Optical Properties of II-VI Compound Low-Dimensional Structures Grown By Molecular Beam Epitaxy

by

Xuecong Zhou

A dissertation submitted to the Graduate Faculty in Physics in partial fulfillment of the requirements for the degree of Doctor of Philosophy, The City University of New York

2005

INFORMATION TO USERS

The quality of this reproduction is dependent upon the quality of the copy submitted. Broken or indistinct print, colored or poor quality illustrations and photographs, print bleed-through, substandard margins, and improper alignment can adversely affect reproduction.

In the unlikely event that the author did not send a complete manuscript and there are missing pages, these will be noted. Also, if unauthorized copyright material had to be removed, a note will indicate the deletion.

ProQuest Information and Learning Company
300 North Zeeb Road
P.O. Box 1346
Ann Arbor, MI 48106-1346

Approval Page

This manuscript has been read and accepted for the Graduate Faculty in Physics in satisfaction of the dissertation requirement for the degree of Doctor of Philosophy.

8/26/04 — Date — Chair of Examining Committee

9/22/04 — Date — Executive Officer

Dr. Maria C. Tamargo

Dr. Ying-Chih Chen

Dr. G. F. Neumark

Dr. Frederick W. Smith

Supervisory Committee

THE CITY UNIVERSITY OF NEW YORK

Abstract

Optical Properties of II-VI Compound Low-Dimensional Structures Grown By Molecular Beam Epitaxy

by
Xuecong Zhou

Advisers: **Professor Maria C. Tamargo**
Professor Ying-Chih Chen

This thesis describes Molecular-Beam Epitaxy (MBE) growth and investigation of the optical properties of a series of materials and structures based on wide-band-gap II-VI materials that have potential applications as light emitting devices, in particular laser diodes. Three types of materials are presented in details: single layers of $Zn_xCd_yMg_{1-x-y}Se$ with different Mg concentrations, optically-pumped blue $Zn_{x'}Cd_{y'}Mg_{1-x'-y'}Se$ /$Zn_xCd_yMg_{1-x-y}Se$ single quantum well (QW) laser structures grown on InP, and CdSe self-assembled quantum dot (SAQD) structures grown on ZnSe, $Zn_{1-x}Be_xSe$ as well as ZnCdMgSe. The goal is to better understand the state of the art QW laser structures based on ZnCdMgSe and propose improvement by using lower-dimensional structures for these devices.

The optical properties of $Zn_xCd_yMg_{1-x-y}Se$ alloys using photoluminescence (PL) and photoluminescence excitation are systematically studied. It is shown that, at low temperatures, PL is dominated by excitons localized by potential fluctuations, which becomes stronger with increasing Mg concentration. Such potential fluctuations are

discussed in terms of a large valence band offset in Zn(Cd)Se/MgSe systems, which serves as a manifestation of the breakdown of "Common-anion Rule".

The lasing operations of the photo-pumped $Zn_{x'}Cd_{y'}Mg_{1-x'-y'}Se$ /$Zn_xCd_yMg_{1-x-y}Se$ separate confinement heterostructure single QW blue and green lasers grown lattice matched to InP are reported. A lower threshold pumping intensity and higher characteristic temperature are obtained for the green laser, which is explained on the basis of the difference in carrier confinement between these two structures.

For the CdSe/ZnSe and CdSe/$Zn_{0.97}Be_{0.03}Se$ SAQDs, the self-assembled growth is reported; the atomic force microscopy measurements on uncapped QDs are given; the steady-state PL and time-resolved PL are performed. Further the QD size and Cd composition are estimated and compared using two different methods for these two QD structures.

The effect of Be concentration on the formation of CdSe SAQDs grown on $Zn_{1-x}Be_xSe$ is investigated. Systematic decrease of the QD size by increasing the Be concentration in the $Zn_{1-x}Be_xSe$ barrier layer is demonstrated. Finally, exploring work for the growth of CdSe/ZnCdMgSe SAQDs is shown, and the initial results are given. By simply changing the deposition time of CdSe, emission through the whole visible range from blue to red has been obtained.

Acknowledgments

This thesis would not be completed without the guidance of my advisers Prof. Maria C. Tamargo and Prof. Ying-Chih Chen, who provide encouragement and inspiration for the past six years. I would like to present my deep appreciation to them.

I owe a debt of gratitude to Dr. Shiping Guo, from whom I have learned many experimental skills and gained a lot of knowledge about the growth and characterization. My thanks also go to other members in the MBE group, Dr. Martin Muñoz, Mr. Mohammad Sohel, Ms. Hong Lu, Ms. Noemi Perez Paz, Dr. Oleg Maksimov, and Dr. F. Fernandez for their significant assistance.

Thanks are due to Dr. C. Chi, Dr. H. Liu, Prof. A. Couzis and Prof. C. Maldarelli in Chemical Engineering in CCNY; Mr. Fleumingue Jean-Mary and Prof. Daniel L. Akins in Chemistry Department in CCNY; Mr. Xiaohui Ni in Physics in CCNY; Dr. Igor L. Kuskovsky, Dr. Yi Gu, Prof. G. F. Neumark, Mr. R. Robinson, and Prof. I. P. Herman in Columbia University; Prof. Y. S. Huang in the National Taiwan University of Science and Technology; Prof. C. Trallero-Giner, and Prof. A. H. Rodríguez in Universidad de La Habana for their great help and cooperation. Thanks are also due to Prof. Frederick W. Smith for his valuable instruction.

Finally I gratefully acknowledge the constant support, encouragement, and patience of my parents and my husband (Mr. Changshi Zhou) without which I cannot concentrate on my research.

CONTENTS

CHAPTER 1 1

INTRODUCTION 1

CHAPTER 2 4

BACKGROUND 4

2-1. Physics background 4
2-1-1. Band structure and dimensionality 4
2-1-2. Design Principles of Semiconductor Lasers 6
2-1-3. II-VI Materials 10
2-1-4. Overall Motivation of This Research 11

2-2. Growth Technique of Molecular Beam Epitaxy 11

2-3. Characterization Techniques 15
2-3-1. Photoluminescence 16
Steady-State Photoluminescence Experimental Setup 18
Time-Resolved Photoluminescence Experimental Setup 19
2-3-2. Photoluminescence Excitation 19
2-3-3. X-ray Diffraction 20
2-3-4. Atomic Force Microscopy Measurement 24
Contact AFM 25
Non-contact AFM 25
2-3-5. Contactless Electroreflectance 26

CHAPTER 3 38

PHOTOLUMINESCENCE PROPERTIES OF $ZN_XCD_YMG_{1-X-Y}SE$ ALLOYS GROWN BY MOLECULAR BEAM EPITAXY 38

3-1. Basics 38
3-1-1. Common-anion Rule 38
3-1-2. Localization Due To Compositional Disorder 39

3-2. Introduction 40

3-3. MBE Growth of $Zn_xCd_yMg_{1-x-y}Se$ alloys 42

3-4. Photoluminescence Properties of $Zn_xCd_yMg_{1-x-y}Se$ Alloys 43

CHAPTER 4 49

CHARACTERISTICS STUDIES OF OPTICALLY-PUMPED BLUE $ZN_X·CD_Y·MG_{1-X'-Y'}·SE/ZN_XCD_YMG_{1-X-Y}SE$ SINGLE QUANTUM WELL LASERS ON INP BY MOLECULAR BEAM EPITAXY 49

4-1. Introduction 49

4-2. MBE Growth of the Laser Structures 52

4-3. Optical Confinement Factor Γ 53

4-4. Photo-Pumping Experiment Setup 56

4-5. Characteristics Studies of the photo-pumped quantum well lasers 57

CHAPTER 5 66

MOLECULAR BEAM EPITAXY GROWTH AND OPTICAL PROPERTIES OF CDSE SELF-ASSEMBLED QUANTUM DOTS 66

5-1. Introduction 66
5-1-1. Historical Developments 66
5-1-2. Fabrication of Self-Assembled Quantum Dots 68

5-2. CdSe/ZnSe and CdSe/$Zn_{0.97}Be_{0.03}Se$ SAQDs 70
5-2-1. Self-Assembled Growth by MBE 71
5-2-2. AFM Measurements of Uncapped QDs 72
5-2-3. Optical Studies of Capped QDs 73

5-3. Effect of Beryllium concentration on the size of self-assembled CdSe quantum dots grown on $Zn_{1-x}Be_xSe$ 79
5-3-1. Introduction 79
5-3-2. Detailed Studies 81

5-4. CdSe/ZnCdMgSe SAQDs 86

CHAPTER 6 104

SUMMARY AND SUGGESTED FUTURE WORKS 104

6-1. Summary 104
6-1-1. $Zn_xCd_yMg_{1-x-y}Se$ alloys 104
6-1-2. Optically-pumped Blue and Green $Zn_x·Cd_y·Mg_{1-x'-y'}Se$ /$Zn_xCd_yMg_{1-x-y}$ Single Quantum Well Lasers Grown on InP 104
6-1-3. CdSe SAQDs on ZnSe and $Zn_{0.97}Be_{0.03}Se$ 105

6-1-4. CdSe SAQDs on $Zn_{1-x}Be_xSe$ 106
6-1-5. CdSe SAQDs on ZnCdMgSe 106

6-2. Future Works 107

PUBLICATIONS **109**

1. Journal Publications (24 publications in total) 109

2. Conference Presentations (16 presentations in total) 111

REFERENCES **114**

Chapter 2 114

Chapter 3 116

Chapter 4 118

Chapter 5 120

LISTS OF ILLUSTRATIONS

Fig. 2.1 Simplified band diagram of a semiconductor 29

Fig. 2.2 Density of states as a function of energy in systems with different numbers of spatial dimensions: 3D, bulk material; 2D, quantum well; 1D, quantum wire; 0D, quantum dot. 29

Fig. 2.3 Schematic structure of (a) conventional semiconductor laser diode and (b) quantum-well laser diode 30

Fig. 2.4 Band alignment of (a) type-I hetero-junction and (b) type-II hetero-junction. ... 30

Fig. 2.5 (a) Bandgap energy and (b) refractive-index profiles of a QW laser structure. The curve shown in (b) is the calculated modal profile of the fundamental transverse mode of the waveguide. 31

Fig. 2.6 Band gap energy vs. lattice constant for some selected semiconductors 31

Fig. 2.7 Conceptual schematics of MBE chamber for ZnCdSe growth..... 32

Fig. 2.8 Riber 2300 MBE System 32

Fig. 2.9 Schematic diagram of the fundamental transitions..... 33

Fig. 2.10 Schematic diagram of the steady state PL setup..... 33

Fig. 2.11 Schematic diagram of the set up for the TRPL measurement 34

Fig. 2.12 X-ray diffraction system..... 34

Fig. 2.13 Principle of X-ray diffraction 35

Fig. 2.14 Possible strain states in the epilayers..... 35

Fig. 2.15 Force sensor in contact AFM..... 36

Fig. 2.16 Non-contact feedback loop..... 36

Fig. 2.17 Schematic representation of the contactless electroreflectance setup in Brooklyn College 37

Fig. 3.1 (a) shows the perturbation of the band edges by potential fluctuation as a function of coordinate in real space. This leads to the formation of tails of states

shown on (b) where the dashed lines show the distribution of states in the unperturbed case. 47

Fig. 3.2 PLE (dotted lines) and PL (solid lines) of $Zn_xCd_yMg_{1-x-y}Se$ alloys with various Mg concentrations at T=10K. The inset: the energy difference (ΔE) between PL and PLE peaks as a function of Mg concentration; the dotted line is the guide for eyes. 47

Fig. 3.3 PL peak energies (solid circles) as a function of temperature for samples with various Mg concentrations. The dotted lines represent the temperature dependence of the CdSe bandgap energy (shifted for easier comparison). 48

Fig. 3.4 PL spectra of $Zn_xCd_yMg_{1-x-y}Se$ alloys with various Mg concentrations as functions of excitation intensity at T=10K (Solid lines represent the highest excitation intensity, and dashed lines represent the excitation intensity about two orders of magnitude lower). The inset: the peak shift as a function of [Mg]; the dotted line is the guide for eyes. 48

Fig. 4.1 Schematic of the separate confinement heterostructure laser structure grown and its band gap profile 61

Fig. 4.2 TE mode for the blue laser. The upper plot is the refractive-index profile. The lower plot is the transverse-electric mode of the electromagnetic wave in the waveguide. 61

Fig. 4.3 (a) Experimental setup for the photopumping experiment; (b) Pumping geometry on the chip 62

Fig. 4.4 Photoluminescence spectra at 77 K of the two SQW laser structures 63

Fig. 4.5 (004) x-ray rocking curve of the SQW blue laser structure. The FWHM of the cladding and guiding layers are 49 arcsec and 70 arcsec respectively. 63

Fig. 4.6 Output intensity vs. pumping intensity at room temperature. The threshold excitation intensity is estimated to be ~ 220 kW/cm^2 for the blue laser and ~ 160 kW/cm^2 for the green laser. 64

Fig. 4.7 Spectra of blue laser emission at different excitation intensities operated at room temperature. (The spectrum at pumping intensity of 177 kW/cm^2 is amplified by 14.5 times in order to see clearly the emission from barrier.) 64

Fig. 4.8 Temperature dependence of the lasing threshold for blue laser structure. Lasing is observed up to 348 K and T_0 is estimated to be 35 K. 65

Fig. 5.1 Schematic diagrams of the three possible growth modes: Frank-van der Merwe (FvdM), Volmer-Weber (VW), and Stranski-Krastanow (SK). 91

Fig 5.2 (004) symmetrical reflection and (115) *a* and *b* asymmetrical reflection DCXRD rocking curves for a ZnBeSe epilayer grown right before the QD samples' growth.91

Fig. 5.3 AFM images of 2.5 MLs of CdSe depositied on $Zn_{0.97}Be_{0.03}Se$ (a) and on ZnSe (b) at 320°C (2 μm x 2 μm)..... 92

Fig. 5.4 Three-dimensional AFM images of 2.5 MLs of CdSe deposited on $Zn_{0.97}Be_{0.03}Se$ at 320°C (2 μm x 2 μm). 92

Fig. 5.5 Steady state PL intensity profiles at 77 K (a) and RT (b) for CdSe QDs grown on ZnSe (solid) and on $Zn_{0.97}Be_{0.03}Se$ (dash)..... 93

Fig. 5.6 Time-resolved PL at 77 K (a) and RT (b) for CdSe QDs grown on ZnSe (open squares) and on $Zn_{0.97}Be_{0.03}Se$ (solid triangles); (c) Temperature dependences of PL decay time for CdSe QDs grown on ZnSe (open squares) and on $Zn_{0.97}Be_{0.03}Se$ (solid triangles). 94

Fig. 5.7 (a) The calculated PL emission energies (dashed lines) for $Cd_xZn_{1-x}Se/Zn_{0.97}Be_{0.03}Se$ QDs as a function of *x* and *d*. The PL spectrum (T=9K) is also shown. The inset shows an example for estimation of *x* and *d*; (b) The PL (solid line) and PLE spectra (open circles, plotted in a semi-log scale) for the $CdSe/Zn_{0.97}Be_{0.03}Se$ QD sample at T=9K. The detection energy and three equally spaced peaks (A, B and C) are indicated by arrows. The inset is the magnification of the marked region in the PLE spectrum: open circles represent the experimental data, and the solid line is the result of the fitting with two Lorentzians (dashed lines). 95

Fig. 5.8 Integrated PL intensity as a function of temperature for CdSe QDs grown on ZnSe (solid circles) and $Zn_{0.97}Be_{0.03}Se$ (open circles). 96

Fig. 5.9 (a) CER spectrum at RT for CdSe/ZnSe QDs structure, where solid line represents the experimental data and the dashed line is the fit. The transitions are indicated by the arrows. (b). Polarized Raman scattering spectroscopy for CdSe/ZnSe QDs structure with the 514 nm line of an Ar^+ laser as excitation source: open circles represent experimental data, solid line is the guide for the eye and dash lines are the results of fitting..... 97

Fig. 5.10 PL emission at 77 K for the CdSe QD structures on $Zn_{1-x}Be_xSe$ with different Be concentration obtained by changing the Be cell temperature while keeping the Zn cell temperature constant. The dashed line is drawn to aid the eye..... 98

Fig. 5.11 PL emission at 77 K for the CdSe QD structures on $Zn_{1-x}Be_xSe$ with different Be concentration obtained by changing the Zn cell temperature while keeping the Be cell temperature constant. The triangles and the squares represent the QD structures grown on "new" and "used" Mo-blocks, respectively. The lines are connect of the QD structures having different Be concentration in the barrier layer grown on the

same day and are a guide for the eye. The two QD structures represented by the open triangles and the two by the open squares were grown on the same day with the two sets of blocks. 98

Fig. 5.12 77 K PL spectrum (a), amplified (10X) RT measured CER spectrum (b), RT measured CER spectrum (c) and the first derivative of the SPV spectrum (d) for the sample with 77 K PL peak energy of 2.553 eV ([Be]~ 5.3%) shown in Fig. 5.11. The dash-dot lines in (b) and (c) are fitting results. 99

Fig. 5.13 First derivative of the RT SPV spectra for the four samples represented by the open symbols in Fig. 5.11 99

Fig. 5.14 PL emission at 77 K for the two CdSe QD structures on $Zn_{1-x}Be_xSe$ with two different Be concentrations (2%: solid line and 24%: dotted line) in the barrier layer obtained by the combination of changing the Zn and Be cell temperatures simultaneously 100

Fig. 5.15 Atomic force microscopy measurements (contact mode) for the two uncapped CdSe QD structures on $Zn_{1-x}Be_xSe$ with significantly different Be concentrations in the barrier layer a) with 2% Be and b) with 24% Be. The large-scale modulation seen in the background of b) is due to the greater roughness on the surface of the $Zn_{0.76}Be_{0.24}Se$ layer. 100

Fig.5.16 PL spectra for samples with different deposition time of CdSe deposited at 320°C 101

Fig. 5.17 PL spectra for the samples with different deposition time of CdSe deposited at 270°C 102

Fig. 5.18 Three dimensional AFM image of CdSe QDs grown on ZnCdMgSe of Eg~2.8 eV nearly lattice-matched to InP 103

Chapter 1

Introduction

Semiconductors are materials whose electrical conductivities are intermediate between those of metals and insulators. Their properties can be controlled in a variety of ways, one of which is by adjusting the size and dimensionality of the semiconductors. Since the invention of the bipolar transistor in 1947, a semiconductor revolution has occurred that is still in progress. Most recently, the dimensionality of the semiconductors has evolved rapidly from three-dimension (bulk material or thick layers) to two-dimension (quantum well), and to 0-dimension (quantum dots). The corresponding device characteristics have been greatly improved due to the low dimensional nature of the active region. The research on semiconductors involves two aspects: the material growth and properties investigations.

Molecular beam epitaxy (MBE) is an advanced and complex technology to grow semiconductor structures. With the ability to grow with atomic layer accuracy, it has proven strength in fabricating heterostructure devices, such as optical detectors, light-emitting diodes (LEDs), double heterostructure lasers, quantum well (QW) lasers, and even quantum dots (QDs) lasers. Today, high quality devices are routinely fabricated in laboratories and factories by MBE.

There are various methods to study the properties of semiconductors, such as electrical methods, optical methods, and methods based on structure studies, etc. Among them, optical methods are widely used due to their high efficiency and non-destructive

characteristics. Furthermore, many of the semiconductors of interest are used as light emitters, thus their optical properties are of interest from the point of view of developing applications.

In this work, I will report the growth by MBE of three-dimensional structures ($Zn_xCd_yMg_{1-x-y}Se$ thick layers with different Mg concentrations), two-dimensional structures (photo-pumped $Zn_{x'}Cd_{y'}Mg_{1-x'-y'}Se/Zn_xCd_yMg_{1-x-y}Se$ single QW blue and green lasers lattice-matched to InP with quaternary $Zn_xCd_yMg_{1-x-y}Se$ QW as active layer), and 0-dimensional structures (CdSe self-assembled QDs). I will also report the optical property investigations of these structures. In the chapters that follow, I will discuss these results in details. The goal of this work is to provide information to optimize the design of wide band gap II-VI-based laser diodes that emit in the blue region of the spectrum by understanding the properties of the ZnCdMgSe material, understanding the limits of the QW laser structures and exploring lower dimensional SAQD structures for device applications.

In chapter 2, I will discuss related physics backgrounds, the basics of MBE growth technique and the various sample characterization methods (including steady-state photoluminescence (PL), time-resolved PL (TRPL), x-ray diffraction, atomic force microscopy (AFM), photoluminescence excitation (PLE), and contactless electroreflectance (CER)).

Chapter 3 focused on the investigation of the optical properties of the $Zn_xCd_yMg_{1-x-y}Se$ alloys with different Mg concentrations where PLE, temperature dependent PL as well as intensity dependent PL studies have been involved. The localized exciton origin of the low temperature PL will be studied and discussed in terms of a large valence band

offset in Zn(Cd)Se/MgSe systems, which serves as a manifestation of the breakdown of "Common-anion Rule". The basic understanding about the common-anion rule as well as the formation of luminescence band of localized excitons is given briefly at first.

Chapter 4 details the MBE growth and lasing characteristics studies of photo-pumped $Zn_{x'}Cd_{y'}Mg_{1-x'-y'}Se/Zn_xCd_yMg_{1-x-y}Se$ single QW blue and green lasers lattice-matched to InP with quaternary $Zn_xCd_yMg_{1-x-y}Se$ QW as active layer. The comparison of the threshold pumping intensity and the characteristic temperature for these two lasers has been given and explained on the basis of the difference in carrier confinement between these two structures. The optical confinement calculation is first given.

In chapter 5, I will first present a general background on the historical developments on QDs, and the fabrication of self-assembled QDs (SAQDs). Then I will report the MBE growth of CdSe SAQDs on ZnSe and $Zn_{0.97}Be_{0.03}Se$. AFM has been used to measure the size of uncapped QDs. For the capped QDs, we have performed steady-state PL and TRPL studies. The PLE as well as Raman scattering spectroscopy studies on the $CdSe/Zn_{0.97}Be_{0.03}Se$ capped QDs structures and the CER studies on the CdSe/ZnSe capped QDs structures have been shown. The comparison of these two types of QDs structures has been given based on AFM and optical studies. Also, systematic studies about the effect of Be concentration on the size of $CdSe/Zn_{1-x}Be_xSe$ SAQDs will be given. At the end, exploring experiments for the growth of CdSe/ZnCdMgSe SAQDs is briefly described and the initial results are shown.

Finally, the summary chapter (chapter 6) and the list of publications highlight the key achievements of this dissertation.

Chapter 2

Background

2-1. Physics background

2-1-1. Band structure and dimensionality

When similar atoms are brought together to form a solid such as a crystal, their valence electrons begin to interact, i.e., the corresponding electronic wave functions start to overlap. The band structure of a crystalline solid, that is, the energy-momentum (E-k) relationship, is usually obtained by solving the Schrödinger equation. To solve this equation for a crystal, the electrons are assumed to be in a periodic potential field created by the nuclei of the atoms, and the dimensions are assumed to be infinite over space. The allowed electronic states separated by an energy gap are obtained. Energy regions or energy bands are permitted above and below this energy gap. The upper unpopulated bands are called the conduction bands; the lower filled bands, the valence bands. The separation between the energy of the lowest conduction band and that of the highest valence band is called the bandgap E_g. It is the magnitude of the energy gap that determines whether a solid is a metal, a semiconductor, or an insulator. In a semiconductor, the bandgap usually extends below 3 eV. Shown in Fig. 2.1 is the simplified band structure diagram.

When the size of the periodic potential field (or the crystal) is reduced in any dimension to a scale comparable to that of the electronic wave function, the electron will posses discrete states instead of bands. Thus, the dimensionality reduction from bulk (3D)

to quantum well (2D), then to quantum wire (1D), finally complete reduction of dimensionality in all three directions to atomic values (0D) leads to carrier localization in all three dimensions and consequently breakdown of the classical band structure model. The reduction of the dimensionality of the system is directly reflected in the dependence of the density of states on energy.

The density of states for a three-dimensional system (bulk semiconductor) has the form

$$\frac{dN}{dE} \propto \frac{d}{dE} E^{3/2} = E^{1/2} \tag{2-1}$$

For a two-dimensional system (quantum well), it is a step function given by

$$\frac{dN}{dE} \propto \frac{d}{dE} \sum_{\varepsilon_i < E} (E - \varepsilon_i) = \sum_{\varepsilon_i < E} 1 \tag{2-2}$$

For a one-dimensional system (quantum wire), it is an inversal square root of the excess energy above the band gap,

$$\frac{dN}{dE} \propto \frac{d}{dE} \sum_{\varepsilon_i < E} (E - \varepsilon_i)^{1/2} = \sum_{\varepsilon_i < E} (E - \varepsilon_i)^{-1/2} \tag{2-3}$$

And for a zero-dimensional system (quantum dot), it consists of discrete states given by

$$\frac{dN}{dE} \propto \frac{d}{dE} \sum_{\varepsilon_i < E} \Theta(E - \varepsilon_i) = \sum_{\varepsilon_i} \delta(E - \varepsilon_i) \tag{2-4}$$

where ε_i are discrete energy levels, Θ is the Heaviside step function, and δ is the Dirac function. Obviously, the reduction in the freedom of motion in low-dimensional structures significantly modifies the density of states, as illustrated schematically in Fig. 2.2. In contrast to higher dimensional structures, such as bulk crystal materials, and even QWs and quantum wires, in which the density-of-states is continuum in energy for at

least some directions, quantum dots have atomic-like discrete energy states, and the physical properties of quantum dots in many, although not all, respects resemble those of an atom. A profound size-dependent change of all macroscopic material properties as compared to the bulk occurs. For QDs, as a consequence of the discrete nature of the energy spectrum, optical transitions between these states are expected to be extremely narrow in energy, with their line width becoming much less sensitive to increasing temperature (although the population of the different states will of course depend on temperature). This feature, together with increased carrier localization due to the confinement in all three dimensions which results in a major enhancement of optical transition matrix elements, holds promise of significant improvements in optical and electronic device applications involving QDs.[1,2] Indeed, device configurations involving SAQDs fabricated from III-V semiconductors[3-5] have already exhibited many superior properties over structures based on quantum wells.

2-1-2. Design Principles of Semiconductor Lasers

In this section, a brief introduction about the design principles of the semiconductor lasers will be given in order to understand what the requirements of the semiconductor materials are and how we choose the structure to grow in order to fabricate optically-pumped lasers as will be described in chapter 4.

As we know, lasing only occurs under two essential conditions.[6,7] the presence of a gain medium that can amplify the light passing through it and a feedback mechanism which forms a resonator. In a semiconductor laser, the gain medium is the semiconductor itself which can emit and amplify the electromagnetic radiation and the feedback

mechanism is usually a Fabry-Perot cavity formed by two natural cleavage planes of the semiconductor. The typical structure of a semiconductor laser is shown in Fig. 2.3.

Light amplification is accomplished by a process called stimulated emission. There are three processes of interaction between the electromagnetic wave and matter: spontaneous emission, stimulated emission and absorption. The Einstein relations show that the absorption and stimulated emission probabilities are equal and are both related to the spontaneous emission probability. These expressions lead to the necessary condition for stimulated emission, which is that the separation in quasi-Fermi levels should exceed the band gap energy, i.e. $F_n - F_p > E_g$. The separation of quasi-Fermi levels can be achieved by the injection of electrons and holes using either electrical or optical pumping to disturb the thermal equilibrium. When the electrons and holes are injected into the active region, they will distribute in the conduction band minimum and valence band maximum associated with their density of state function, respectively. The distribution of both carriers can be described using their quasi-Fermi levels assuming that they are in quasi-thermal equilibrium. When the injected electrons and holes reach certain concentration, the separation of the quasi-Fermi levels will be larger than the bandgap. Then the stimulated emission will occur and dominate.

In order to efficiently collect the injected carriers, heterostructures in which the active region is sandwiched by two larger bandgap materials are used in semiconductor lasers. In general, the band alignment at the hetero-junction can be type-I or type-II, as illustrated in Fig. 2.4. The conduction band offset between the active layer and the two larger bandgap layers should be able to prevent the electrons from flowing out of the active region while the valence band offset between the active layer and the two larger

bandgap layers should be able to prevent the holes from flowing out of the active region. So a type-I interface is required. Also band offset should be much larger than 25 meV (=kT), the thermal energy at room temperature. A band offset of at least 100 meV is required to provide effective carrier confinement.[7]

The laser consists of a thin active layer, which is sandwiched between two cladding layers with higher bandgap energy. In a conventional semiconductor laser diode, the thickness of the active layers is typically in the range of 0.1-0.3 μm. The functions of the higher energy bandgap for the cladding layer are to provide the energy barrier needed for carrier confinement, while also providing waveguiding for optical confinement for the electromagnetic radiation.

When the thickness of the active layer is reduced to the dimension comparable to the de Broglie wavelength of the carriers, the kinetic energy of the carriers associated with the motion in the direction perpendicular to layer is quantized, giving rise to a set of discrete energy levels. The quantum effect becomes pronounced when the thickness is less than 10 nm. The quantization of energy changes the three dimensional bulk properties into two-dimensional. There are two major benefits resulting from the use of the quantum well structure. First, the density of states near the bandgap is increased, which reduces the number of carriers needed to achieve optical transparency in the active layer. Second, due to the higher energy level of the heavy hole with respect to the valence band edge compared with the light hole, most of the holes will populate in the heavy hole bands. Thus, most of the radiative recombination comes from the transition between the electron and the heavy hole bands, which results in the radiation of pure transverse electric (TE) wave in the waveguide configuration.

Although QW lasers seem to have better gain properties, the thin QW reduces the confinement factor Γ.[7] (Confinement factor Γ is a figure of merit measuring the confinement of the light within the active region, defined by the ratio of the power in the active region to the total power of the light.) So the structure needs some modification. In designing the QW laser, a pair of waveguide layers with intermediate bandgap are always inserted between the active layer (QW) and the two cladding layers to form the separate confinement structure. The introduction of the waveguide layers improves both the wave and carrier confinements. Fig. 2.5 shows the schematic of bandgap energy and refractive–index profiles of a QW laser. Fig. 2.5(a) is the desired band lineup for the cladding, waveguiding and QW layers. The QW has the smallest bandgap energy while cladding layers have the largest bandgap energy to confine electrons and holes. Fig. 2.5 (b) is the corresponding refractive-index profile and the curve in it is the calculated modal profile of the fundamental transverse mode of the waveguide. The QW has the largest index of refraction and the cladding layers have the smallest index of refraction. Since the wave confinement factor is proportional to the square of the thickness of active layer, the confinement factor of a QW with 10 nm width is about 0.1%, much less than that of the double heterostructure (DH) lasers (~30%). By using the waveguide layers to focus the intensity distribution to the center, a confinement factor of 3% can be achieved with optimal design. Another function of the two waveguide layers is to help the carriers to be scattered into the well. Because the width of QW is smaller than the mean free path of the carriers, an intermediate stage is necessary to collect the carriers efficiently. From the point view of carrier confinement, a wider waveguide layer is preferred. However, a wider waveguide layer can lead to a higher-order mode that is not desirable. Usually a

single-mode operation can be ensured if the thickness of the waveguide layers is less than 2000Å. Finally the thickness of the cladding layer must be thick enough to prevent the wave from spreading out of the cladding layer. The effectiveness of optical confinement in such a waveguide depends on the difference of the refractive indices between adjacent layers and the thickness of each layer. The details about the optical confinement will be discussed in Chapter 4-4.

2-1-3. II-VI Materials

Shown in Fig. 2.6 is the band gap energy vs. lattice constant for some selected semiconductors involved in this work. Clearly, by adjusting the flux ratio between ZnSe, CdSe, and MgSe, ternary ZnCdSe and quaternary ZnCdMgSe lattice matched to InP could be obtained. Previously, our group in CCNY has performed a series of studies in this system. The (Zn, Cd, Mg) Se quaternary alloys have been grown lattice matched to InP substrates with band gap ranging from 2.2 to 3.5 eV[8]. QW structures entirely lattice matched to InP with a large band gap quaternary $Zn_xCd_yMg_{1-x-y}Se$ alloy as the barrier layers and a ternary $Zn_xCd_{1-x}Se$ as the active layer have been grown with emissions ranging from red to blue[8,9], covering the entire visible range. Emission from yellow to blue is obtained by simply varying the lattice-matched ZnCdSe quantum well thickness while the red emission is achieved by using a strained ZnCdSe active layer with excess Cd. Based on these ZnCdSe/ZnCdMgSe QWs, optically pumped laser structures[10] and LEDs[11]emitting at the spectral range from red to blue have been demonstrated. Also, ZnSe as well as $Zn_{1-x}Be_xSe$ could be easily grown pseudomorphic to GaAs substrate. And CdSe self-assembled QDs (SAQDs) with ZnSe as barrier layer has been well studied.[12,13]

2-1-4. Overall Motivation of This Research

In section 2-1-1 we show that the optical transitions in QDs are expected to be very narrow in energy with their linewidth much less sensitive to increasing temperature. Also, the threhold current density could be greatly reduced for opto-electronic devices involving QDs due to the enhancement of the exciton binding energy and oscillator strength resulting from the three-dimensional confinement. Additional advantages may arise from the spatial separation of carrier localization and defect involving sites in the active region[14] when QDs is involved, resulting in the improvement of the degradation problem. The overall long term motivation of this research is to incorporate QDs in the active layer of the light emitting devices, especially lasers, to improve their operating characteristics. I will first study the optical properties of ZnCdMgSe alloys to gain more knowledge of this system, secondly I will investigate the photo-pumped $Zn_xCd_yMg_{1-x-y}Se$ /$Zn_xCd_yMg_{1-x-y}Se$ single QW laser structure to gain more experiences for the laser in terms of the structure design, fabrication and pumping experiment, and to better understand their limitations. Then, I will perform studies of the growth and optical properties of CdSe QDs, starting with ZnSe and $Zn_{1-x}Be_xSe$ as barrier layer, then switching to those with ZnCdMgSe as barrier layer in order to incorporate CdSe QDs in the active layer of light emitting device in (Zn, Cd, Mg) Se system.

2-2. Growth Technique of Molecular Beam Epitaxy

Molecular beam epitaxy is a versatile technique for growing semiconductor epitaxial thin films.[15] In MBE, thin films crystallize via reactions between thermal-energy molecular or atomic beams of the constituent elements and a substrate surface maintained

at a desired temperature in ultrahigh vacuum (UHV). The composition of the grown epilayer and its doping level depend on the relative arrival rates of the constituent elements and dopants, which in turn depend on the evaporation rates of the appropriate sources. This process is illustrated schematically in Fig. 2.7, which shows the essential components necessary for MBE growth of ZnCdSe. All these components are in a UHV environment. Molecular beams are provided by thermal Knudson effusion cells. Each cell contains a crucible, which in turn contains one of the constituent chemical elements or compounds of the desired epilyer. Individual thermocouples are embedded in each cell oven as well as in the substrate heater. Together with the feedback loop control, desired stable temperature for each cell and the substrate could be obtained. The temperature of each cell is chosen so that the vapor pressures of the materials are sufficiently high for generation of thermal energy molecular beams by free evaporation. The cells are arranged so that the central portion of the beam flux distribution from each cell intersects the substrate. Each cell has a shutter between the cell and the substrate. Operation of these shutters permits abrupt cessation or initiation of any given beam flux to the substrate. By choosing the appropriate cell at a desired temperature through the opening of its shutter and the appropriate substrate temperature, epitaxial films of the desired chemical components can be obtained. The extremely high precision in beam flux control allows the growth of very thin layers, even monolayers. This distinguishing characteristic has enabled MBE to become one of the main growth technologies for heterostructures including quantum wells, superlattices and quantum dots.

All the growth experiments in this dissertation were performed in a Riber 2300P MBE system in Prof. M. C. Tamargo's lab in CCNY. Fig. 2.8 shows the schematic of the

top-view of this system. The system includes 6 chambers: loading chamber, transfer channel, substrate treatment chamber, metallization chamber, and two growth chambers (III-V chamber and II-VI chamber). The III-V chamber is dedicated for the growth of III-V materials and II-VI chamber is dedicated for the growth of II-VI materials. There are several gate valves to separate all the chambers to ensure that unintentional cross contamination between them does not occur. In order to avoid contamination and achieve ultra-high vacuum, each the chamber is pumped by an ion-pump and a Ti sublimation pump except the loading chamber, which is pumped by a turbo-molecular pump with a mechanical pump as the first stage, and the substrate treatment chamber, which is pumped by a cryo-pump. Besides the ion pump, the II-VI chamber and the metallization chamber are each pumped by an additional cryo-pump. The loading chamber is used for introducing the substrates into the UHV system and removing them after growth. There is a gate valve between the loading chamber and the other chambers which allows us to vent the loading chamber by using ultra pure nitrogen gas to load substrates and not affect the vacuum in other chambers. This allows the vacuum in the other chambers to remain in the range of 10^{-10} Torr. The substrates or samples can be transferred within the system through the transfer channel. The substrate treatment chamber is used to out-gas the substrates before transferring them to the growth chamber. Or it could be used to bake the new Moly blocks. The metallization chamber is equipped with an electron-beam evaporator, which can deposit metal layers in situ on the sample to fabricate a device.

The chambers for the growth of III-V and II-VI semiconductor materials are similar. Each is equipped with a substrate manipulator that consists of holder, rotator, heater and temperature sensor of the substrates, Reflection High-Energy Electron

Diffraction (RHEED), quadrupole mass spectrometer, and cryo-shrouds around the manipulator and the cells. These cryo-shrouds will have a flow of liquid nitrogen (LN) through them during growth to prevent the thermal interference between the sources and also trap the residual molecules inside the chamber to obtain UHV vacuum. There are 8 cell ports in the III-V chamber, 6 cells are equipped for Ga, In, Al, As, Si (for n-type doping) and Be (for p-type doping), and 8 cells in the II-VI chamber for Zn, Cd, Mg, Se, Te, Be, $ZnCl_2$ (for Cl flux used for n-type doping) and a radio frequency (RF) nitrogen cell for p-type doping. Very high purity materials from 6N to 8N have been used as the source materials to ensure high purity films are grown.

Being realized in an UHV environment, MBE is compatible with *in situ* surface diagnostic methods such as RHEED[16,17] to monitor the surface during the substrate deoxidation and epilayer growth as shown in Fig. 2.7. In the RHEED, electrons with energies 20-100 keV are generated by an electron gun and incident on the sample surface at a very small (glancing) angle. They are diffracted by the surface layers and are detected by the fluorescence they cause on the phosphor screen. The glancing incidence insures that the electrons penetrate only through a very thin layer of the surface. Therefore RHEED is very sensitive to the surface and is an ideal method to monitor the surface *in situ*. The RHEED pattern depends on the atomic arrangement, flatness of the surface and the direction of the growth surface. Typical RHEED pattern for a disordered surface (for example before the deoxidization) is a diffuse pattern or rings due to the thin amorphous oxide layer on the surface,[18] for a clean surface after deoxidization it is streaky lines or ordered spots.[18] For three dimensional (island) growth it is ordered spots such as a bulk crystal pattern; for two dimensional (layer by layer) growth it is streaky

with a surface reconstruction. The typical surface reconstructions for an As-rich (001) GaAs surface are (2×4) or c(4×4) or c(2×8) depending on how much excess As is on the surface,[16,17] for a Ga-rich (001) GaAs surface they are (4×2) or c(8×2); for a Se-rich (001) ZnSe the typical pattern is (2×1) and for Zn-rich (001) ZnSe the pattern is C(2×2).[17] Thus, from the RHEED pattern we can know whether the deoxidization is finished, whether the growth is two dimensional or 0-dimensinal and which element terminates the surface.

2-3. Characterization Techniques

When the growth was finished, the samples were taken out from the chamber and removed from the Molydenum (Moly) block. The band gap of the material was measured by steady state PL. The crystalline quality and lattice-mismatch were measured by single crystal x-ray diffraction and double crystal x-ray diffraction. The surface topography of QDs samples was measured by AFM. The lifetimes of the QDs samples were measured by TRPL. We have done studies on QDs samples based on CER, PLE and Raman scattering spectroscopy measurements. For the blue laser structures, photo-pumping experiment has been performed. In the study of quaternary thin layers in chapter 3, PL as well as PLE will be employed. In the following I will introduce the PL (including the steady-state PL and TRPL), PLE, X-ray diffraction, AFM and CER measurements. The photo-pumping experiment will be described in details in Chapter 4.

2-3-1. Photoluminescence

To excite luminescence in semiconductors, a high concentration of electron-hole (e-h) pairs must be generated. This can be done by several methods and optical excitation is one of them. In a PL experiment, e-h pairs are photoexcited by absorption of light in an almost monochromatic non-equilibrium state. They diffuse and relax into a quasiequilibrium distributiom while they are depleted by radiative and non-radiative recombination. There are three different processes in PL: (i) e-h pair excitation, (ii) e-h pair thermalization and diffusion, (iii) e-h recombination. There are many radiative transitions involved in the luminescence emission. Here we give a brief summary on the fundamental transitions, those occurring at or near the band edges. Figure 2.9 is the schematic summarizing the fundamental transitions.

1. Excitonic Recombination

   Free Exciton (E)

   Bound Exciton (BE)

2. Conduction Band to Valence Band Transitions (C—V)

3. Transition Between a Band and an Impurity Level

   Shallow Transitions (C—D, A—V)

   Deep Transitions (D—V, C—A)

   Transitions to Deep Levels (DD—V, C—DA)

4. Donor—Acceptor Transitions DAP (D—A)

As to non-radiative transitions, the main processes are: Auger effect where the energy released by a recombining electron is immediately absorbed by another electron which

then dissipates this energy by emitting phonons, surface recombination resulting from a high concentration of deep and shallow levels on the surface, recombination through defects or inclusions and multiple-phonon emission. PL intensity depends on the competition between the radiative recombination and the non-radiative recombination both existing in the recombination process after photoexcitation. The steady-state PL intensity is proportional to the internal quantum efficiency which is defined as $\eta = \tau/ \tau_r$ where $1/\tau=1/ \tau_r+1/ \tau_{nr}$ and τ is the total lifetime which can be evaluated by a time-resolved PL measurement, τ_{nr} is the non-radiative lifetime, and τ_r is the radiative lifetime.

Photoluminescence is a non-destructive spectroscopic technique for analyzing both the intrinsic and the extrinsic properties of semiconductors. It concerns the radiation emitted by a crystal after optical excitation. In particular, it regards the radiative recombination paths of photoexcited electron-hole (e-h) pairs. Through the analysis of the luminescence spectrum as a function of different parameters (temperature, excitation energy, excitation intensity, external fields, etc.), general information on the material quality can be gained. This motivates science and solid state physics. Here we summarize the main advantages of this technique:

(i). It is a non-destructive technique where only small quantities of material are needed.

(ii). It provides information mainly on minority carrier properties and, thus, it is complementary to electrical characterization techniques. The lifetime, the diffusion length, the quantum efficiency could be inferred through the study of the recombination paths;

(iii). It is an easy technique, because it does not require particular sample handling and preparation. The experimental set-up complexity is proportional to the needs: for quick characterization a very simple and low cost apparatus is sufficient[19];

(iv). It is sensitive to the chemical species of impurities that can be detected even at very low densities;

(v). It is an optical spectroscopic technique, i.e., it gives energetically resolved information.

Steady-State Photoluminescence Experimental Setup

The schematic of the steady-state PL system is shown in Fig. 2.10. The samples are mounted on the cold finger of a Janis cryogenic system. The system is pumped to ~ 10^{-5} Torr before cooling it. The cold finger can be cooled down to 5.8 K using liquid helium and 78 K using liquid nitrogen. The temperature of the cold finger can be controlled between 5.8 K to 300 K by using a heater installed on the back of the cold finger. A He-Cd laser with the emission wavelength of 325 nm is used as the excitation source. The laser beam passes through a chopper which changes the laser beam to a periodic signal (ac), then is focused to a small spot on a sample. The luminescence from the sample is collected by a lens and converted to a collimated beam. The collimated beam is focused to a spot on the first slit of the spectrometer. The beams that pass through the SPEX 1680-B spectrometer are detected by a photomultiplier and are converted to an electrical signal. The ac signal is then fed to a lock-in amplifier to be amplified. Finally the amplified signal is inputted to the data-scan connected to the computer to be collected and analyzed. With the neutral density filter, intensity dependent PL could be done. The

PL spectrum can give us the information about the band gap, quality and band structure of the epilayers.[20]

Time-Resolved Photoluminescence Experimental Setup

Time-Resolved photoluminescence (TRPL) spectroscopy is a very powerful technique for the investigation of carrier dynamics in low-dimensional semiconductor structures. In TRPL we excite e-h pairs by a short pulse of light, and then observe the PL intensity as it decays as a function of time. From fitting of the decay curves, value of the lifetime τ can be evaluated.

Fig. 2.11 is a schematic diagram of the set up for the TRPL measurement. TRPL measurements were carried out using the second harmonic (by KDP crystal) of an amplified colliding pulse mode-locking (CPM) output (pulse width=100 fs, repetition rate=5 kHz) at 305 nm wavelength. The 305 nm light was focused on to the sample. The spectrally integrated emission of the sample was obtained by using a streak camera with a time resolution of 10 fs. The data was recorded into the computer which is connected to the Streak Camera. Filter 1 ensures that the light from CPM will not go to the sample and Filter 2 ensures that the excitation light (305 nm) will not go to the Streak Camera. The temperature dependent measurements were performed in a liquid nitrogen continuous flow cryostat with a temperature control unit.

2-3-2. Photoluminescence Excitation

If the laser providing the excitation with fixed-wavelength lines is replaced by a dye laser or other tunable unit, the arrangement shown in Fig. 2.10 also serves for the

alternative technique of photoluminescence excitation (PLE) spectroscopy, where the exciting energy is varied and the monochromator in the spectrometer is set at a fixed wavelength to track the resulting luminescence. This technique offers advantages in some applications, because it allows resonant excitation at important PL features such as exciton peaks. In our PLE setup, a 300 W xenon lamp, coupled with a ¼ m monochromator, was used as a tunable excitation source.

2-3-3. X-ray Diffraction

X-ray diffraction is an important technique[21] used to characterize semiconductor materials. It can give information about the lattice constant, the crystal structure, the quality and the strain in the layer. The schematic of our x-ray diffraction system is shown in fig. 2.12. It consists of an x-ray source, a single crystal x-ray diffraction (SCXRD) system shown on the right manufactured by RIGAKU and a double crystal x-ray diffraction (DCXRD) system shown on the left manufactured by Blake Industries, Inc. In both cases, the rotation of the sample holder will change the incident angle ω while rotation of the goniometer will change 2θ.

In SCXRD, only one crystal (the sample) is used, so the incident x-ray here is not monochromatic and it is difficult to eliminate the Cu $K_{\alpha 2}$ line. Therefore, the incident x-ray beam contains both Cu $K_{\alpha 1}$ and Cu $K_{\alpha 2}$ lines. In the diffraction, each layer has two peaks corresponding to Cu $K_{\alpha 1}$ and Cu $K_{\alpha 2}$. Usually the intensity of the peak corresponding to Cu $K_{\alpha 1}$ is double that of the peak corresponding to Cu $K_{\alpha 2}$. Because the beam has a broad band of wavelengths, the diffraction peaks are usually broad. In SCXRD, we usually use $\theta - 2\theta$ couple mode, which means that the ω and 2θ are moving

simultaneously and ω is always half of 2θ. In the practical measurement, the back of the sample has indium and it is very hard to mount the sample exactly parallel to the sample holder. In order to make sure the ω and 2θ are coupled, we first fix the 2θ and rotate the ω around θ (usually called a rocking curve), find the ω value corresponding to the peak and adjust the ω value to make sure the ω value corresponding to the peak is θ, which means the ω and 2θ are coupled. We then set the scan mode as the θ – 2θ couple mode to measure the diffraction. The SCXRD is good to measure large lattice-mismatch and to find the structure of the materials.

In DCXRD, a first crystal [(100) Ge in our system] is used to separate the various wavelengths of the incident x-ray beam in order to narrow the x-ray band of wavelengths before the x-ray beam reaches the sample. So the incident beam on the sample is highly monochromatic. The measurement sample is the second crystal. In DCXRD, the rocking curve is usually measured, that is, the 2θ is fixed and the ω is varied around θ. DCXRD is a very direct and useful way to evaluate the quality of the epitaxial layer and the lattice mismatch between the epitaxial layers and the substrate.[22] This technique is particularly useful for epitaxial layers grown on a thick substrate. In general, for such cases, two diffraction peaks are observed, one from the substrate and one from the epilayer. From the full width at half maximum (FWHM), we can evaluate the material quality. From the peak separation, we can obtain information about the lattice-mismatch.

The principle of the XRD is based on Bragg's law shown schematically in Fig. 2.13:

$$2d_{hkl} = \lambda/\sin\theta \qquad (2\text{–}5)$$

where $d_{hkl} = a/(h^2 + k^2 + l^2)^{1/2}$ (where a is the lattice constant) is the spacing of lattice planes with Miller indices (hkl), θ is the corresponding Bragg angle, and λ is the wavelength of incident X-ray. Bragg's law was derived to explain the X-ray diffraction pattern. When Bragg's law is satisfied, the scattered X-rays will interfere constructively and the X-ray diffraction peak will appear.

The strain state of the epitaxial layer is an important parameter. With the same thickness and lattice-mismatch, the layer that is pseudomorphic has better quality than a relaxed or partially relaxed layer. In our laser structures, we need to make sure the whole structure is pseudomorphic. In the calculation of composition, we also need to know the strain state in the epilayer. Usually, for a system consisting of an epilayer and a substrate with a different lattice-constant, the epilayer could be either fully strained, partially strained, or fully relaxed. When the thickness of the epilayer is less than a certain thickness (critical thickness), the epilayer will be pseudomorphic or fully strained, and the tetragonal structure will be distorted, as shown in Fig. 2.14. The parallel lattice-mismatch in the plane between the epilayer and the substrate will be zero. The perpendicular lattice mismatch $[\Delta a/a_s|_\perp = (a_\perp - a_s)/a_s]$ in the growth direction can be obtained by (400) reflection. When the thickness of the epilayer is larger than the critical thickness, the epilayer will be partially or fully relaxed. In the case of a fully relaxed layer, the parallel and perpendicular lattice-mismatch will be the same and equal to the real lattice-mismatch between the epilayer and the substrate and could also be obtained by (400) reflection. For the case of a partially relaxed layer, the parallel and perpendicular lattice-mismatch could be obtained by [511]a and [511]b reflections. In the

following, I will show briefly how to evaluate both the parallel and perpendicular lattice-mismatch and further free standing lattice constant from (511)a and (511)b reflections.

Let θ be the Bragg angle for the (400) reflection, φ be the angle spanning the (001) and (511) diffraction planes of the substrate (φ=15.7932°). The subscripts a and b represent (511) reflection geometries with x-ray incident angle of $\theta+\varphi$ and $\theta-\varphi$, respectively. By measuring peak separations ω_a and ω_b, both representing angles separating the epilayer and the substrate in the corresponding $\{511\}_a$ and $\{511\}_b$ x-ray rocking curves, the perpendicular and parallel lattice mismatches can be determined as follows.[23]

$$(\Delta a/a_s)_\perp = (a_\perp - a_s)/a_s$$

$$= \sin\theta \times \cos\varphi / [\sin\{\theta + (\omega_a + \omega_b)/2\} \times \cos\{\varphi + (\omega_b - \omega_a)/2\}] - 1 \quad (2\text{-}6)$$

$$(\Delta a/a_s)_\parallel = (a_\parallel - a_s)/a_s$$

$$= \sin\theta \times \sin\varphi / [\sin\{\theta + (\omega_a + \omega_b)/2\} \times \sin\{\varphi + (\omega_b - \omega_a)/2\}] - 1 \quad (2\text{-}7)$$

To obtain the strain-free lattice constant, we must use the x-ray results from (511) reflections and the elastic theory. According to the solution of Hooke' s law with biaxial stresses, the perpendicular and parallel strains in the epilayer are related by the Poisson effect so that:

$$\varepsilon_\perp / \varepsilon_\parallel = -2\nu/(1-\nu),$$

$$\varepsilon_\perp = (a_\perp - a_f)/a_f$$

$$\varepsilon_\parallel = (a_\parallel - a_f)/a_f$$

$$a_f = [(1-\nu)/(1+\nu)]\, a_\perp + [(2\nu/(1+\nu)]\, a_\parallel \quad (2\text{-}8)$$

where ν is the Poisson ratio of the film and a_f is the free standing lattice constant. According to Bragg's law, θ = 43.0031° for InP substrate and θ = 45.0723° for GaAs

substrate. The Mg concentrations in the $Zn_xCd_yMg_{1-x-y}Se$ compounds studied in Chapter 3 were obtained by the combined analysis of (511) reflections, PL, and Vegard's law. The calculation of Be concentration based on (511) reflections as well as Vegard's law for the $Zn_{0.97}Be_{0.03}Se$ barrier layer of the CdSe/ $Zn_{0.97}Be_{0.03}Se$ QDs structure will be given in Chapter 5.

2-3-4. Atomic Force Microscopy Measurement

Several techniques are available for magnifying the microscopic features of a surface. Methods for magnifying surface features originated with magnifying lenses and optical microscopy in the late 18th century. Optical instruments are limited by the wavelength of visible light and can observe objects down to approximately 0.5 microns.

During the 20th century, methods for magnification based on electron and ion beams were developed. Operating in a vacuum, the scanning electron microscope (SEM) can resolve features to the level of approximately 30 Å if the specimen's atomic number and SEM technique do not readily yield depth information.

Scanning probe microscopy (SPM) is a recent, innovative technology that relies on a mechanical probe for generation of magnified images. An SPM instrument is operable in ambient air, liquid, or vacuum; and resolves features in three dimensions, down to a fraction of an angstrom. There are two basic modes of SPM—scanning tunneling microscopy (STM) and atomic force microscope (AFM) where the original work was done by G. Binning et al..[24]

Unlike the STM, which monitors fluctuations in currents flowing between the probe tip and a conductive sample, the AFM can provide images of a broad spectrum of

both conducting and insulating materials. AFM can be divided into two primary scanning modes, *contact* and *non-contact*, which simply refers to whether or not the scanning probe actually comes into physical contact with the sample surface.

Contact AFM

In the contact AFM method (Fig. 2.15), the probe tip (which is mounted to the end of the cantilever) scans across the sample surface, coming into direct physical contact with the sample. As the probe tip scans, varying topographic features cause deflection of the tip and cantilever. A light beam from a small laser is bounced off of the cantilever and reflected on to a four-section photodetector. The amount of deflection of the cantilever— or the force it applies to the sample— can then be calculated from the difference in light intensity on the sectors.

Hooke's Law gives the relationship between the cantilever's motion, d, and the force required to generate the motion, F: F=-kd. It is possible to fabricate a cantilever with a force constant, k, of 1 N/m or less. Since motion of less than one angstrom can be measured, forces of less than 0.1 nN are detectable.

Non-contact AFM

As the cantilever moves across the sample surface in contact scanning, the lateral motion of the cantilever may cause damage to soft or fragile samples such as biological specimens or polymers. Because of this phenomenon as well as a number of other variables, non-contact scanning is sometimes preferable.

In non-contact operation (Fig. 2.16), the cantilever is oscillated at its resonant frequency. In this mode, what is being detected is changes in force between the tip and

the sample, even though they are not in contact. These force changes are also referred to as the force gradient. As the probe gets closer to the sample surface, the force gradient changes, thus changing both the oscillation *amplitude* and *phase* of the vibrating cantilever. Either the change in amplitude or the change in phase can be detected and used to control the tracking of the probe over the surface (i.e., the feedback-control loop). *Amplitude detection* is the non-contact method usually used for high-amplitude cantilever vibration. *Phase detection* is the method usually used when the cantilever vibration amplitude is relatively small (and/or higher sensitivity is needed for stable feedback). For our CdSe/ZnSe and CdSe/$Zn_{0.97}Be_{0.03}Se$ QDs samples, we used both contact and non-contact (amplitude detection) AFM to measure the surface topography and the results will be shown in Chapter 5.

2-3-5. Contactless Electroreflectance

Since its inception in 1964, modulation spectroscopy has proven to be a powerful and versatile optical technique for obtaining valuable information about a large variety of semiconductor systems,[25-33] including bulk/thin films, micro- and nanostructures (QWs, multiple QWs, superlattices, quantum wires, QDs), surfaces/interfaces (semiconductor/air (vacuum), semiconductor/semiconductor (hetero- and homojunctions), semiconductor/metal, semiconductor/electrolyte), and the effects of growth/processing, as well as the characterization of actual device structures (heterojunction bipolar transistors, pseudomorphic high electron mobility transistor, QW lasers).

The idea underlying modulation spectroscopy is a very general principle of experimental physics. Instead of directly measuring an optical spectrum (reflectance or

transmission), the derivative of this spectrum with respect to some parameter is measured. This can be easily accomplished by applying the parameter as a small perturbation in a periodic fashion and measuring the corresponding change in the optical properties with phase sensitive detection (i.e. with a lock-in amplifier). Structure in the conventional optical spectra is considerably enhanced in the derivative spectra and flat, structureless backgrounds are eliminated. Weak structure superimposed on a large background is sometimes difficult to resolve due to statistical noise of the background. Its resolution becomes easier in a modulation measurement since the structureless background is eliminated.

The modulation techniques can be classified into two categories: internal and external. In the internal modulation techniques, a parameter of the monochromatic optical beam, such as the wavelength or the degree of polarization, is modulated. In the external techniques, an independent modulation parameter (e.g. a stress, an electric field, etc.) is applied to the sample. Of the external modulation techniques, electroreflectance has remained to this date the most popular technique because of its experimental simplicity and the sharpness of the spectra obtained.

Shown in Fig. 2.17 is our experimental setup of contactless electroreflectance (CER). It utilizes a condenser-like system[34] consisting of a front wire grid electrode with a second metal electrode separated from the first electrode by insulating spacers, which are ~ 0.1 mm larger than the sample dimension. The sample was placed between these two capacitor plates and the electromodulation was achieved by applying an ac voltage of 1.2 kV, 200 Hz across the electrodes. Light from an appropriate light source (xenon arc, halogen, or tungsten lamp) pass through a scanning (probe) monochromator. The exit

intensity at wavelength λ, $I_0(\lambda)$, is focused on the sample by means of a lens. The reflected light is collected by a second lens and is focused on an appropriate detector, generally a photodiode. For simplicity the lenses are not shown.

The light striking the detector contains two signals: the d.c. (or average value) is given by $I_0(\lambda)R(\lambda)$, where $R(\lambda)$ is the d.c. reflectance of the material, while the modulated value (at frequency Ω_m) is $I_0(\lambda)\Delta R(\lambda)$, where $\Delta R(\lambda)$ is the change in reflectance produced by the modulation source. The a.c. signal from the detector, proportional to $I_0\Delta R$, is measured by the lock-in amplifier. In order to evaluate the quantity of interest, i.e. the relative change in reflectance $\Delta R/R$, a normalization procedure must be used to eliminate the uninteresting common feature $I_0(\lambda)$. In Fig. 2.11, the normalization is performed by a variable neutral density filter (VNDF) connected to a servo mechanism. The d.c. signal from the detector, which moves the VNDF in such a manner as to keep $I_0(\lambda)R(\lambda)$ as a constant, i.e. $I_0(\lambda)R(\lambda)=C$. Under these conditions the a.c. signal $I_0(\lambda)\Delta R(\lambda)=C\Delta R(\lambda)/R(\lambda)$. Thus, the signal to the lock-in amplifier is proportional to the quantity of interest, i.e. $\Delta R(\lambda)/R(\lambda)$.

The periodic variation of the measurement conditions gives rise to sharp, differential-like spectra in the region of interband (intersubband) transitions. One of the great advantages of modulation spectroscopy is its ability to perform a lineshape fit. Since, it is possible to account for the lineshapes to yield accurate values of important parameters such as the energies and broadening functions of interband (intersubband) transitions. For our CdSe QDs grown on ZnSe, we performed CER measurement and then the lineshape fitting gives us all the transition energies. By doing theoretical modeling, the size of the QDs could be estimated. The details will be given in Chapter 5.

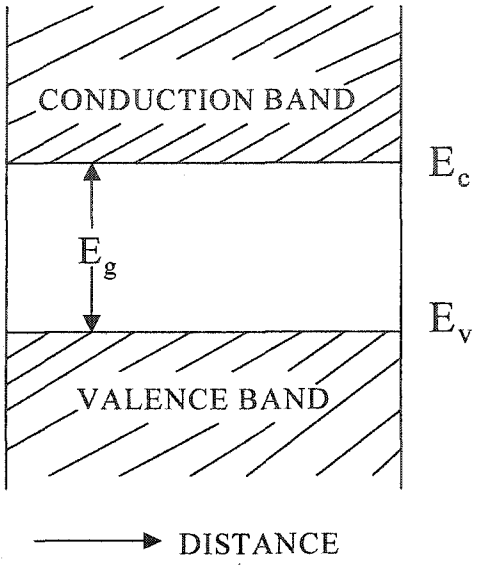

Fig. 2.1 Simplified band diagram of a semiconductor

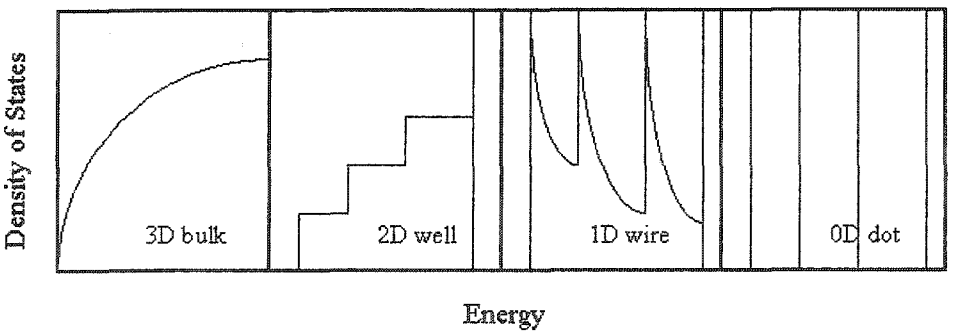

Fig. 2.2 Density of states as a function of energy in systems with different numbers of spatial dimensions: 3D, bulk material; 2D, quantum well; 1D, quantum wire; 0D, quantum dot.

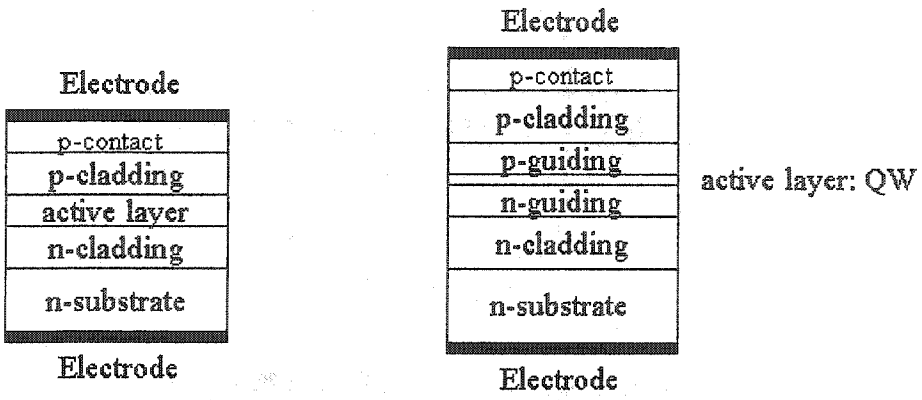

(a) Conventional laser diode (b) Quantum-well laser diode

Fig. 2.3 Schematic structure of (a) conventional semiconductor laser diode and (b) quantum-well laser diode

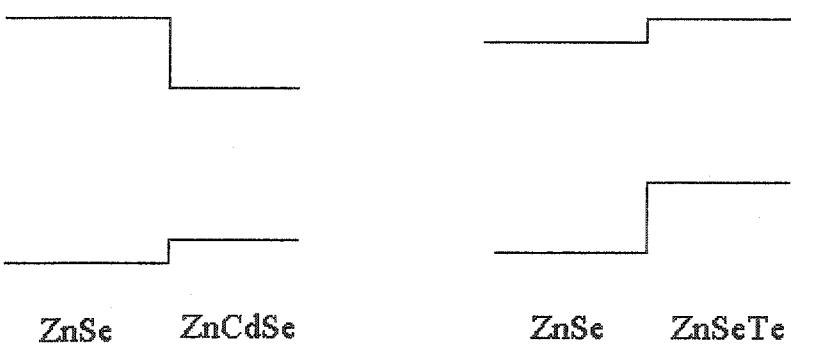

(a) Type-I band lineup (b) Type-II band lineup

Fig. 2.4 Band alignment of (a) type-I hetero-junction and (b) type-II hetero-junction.

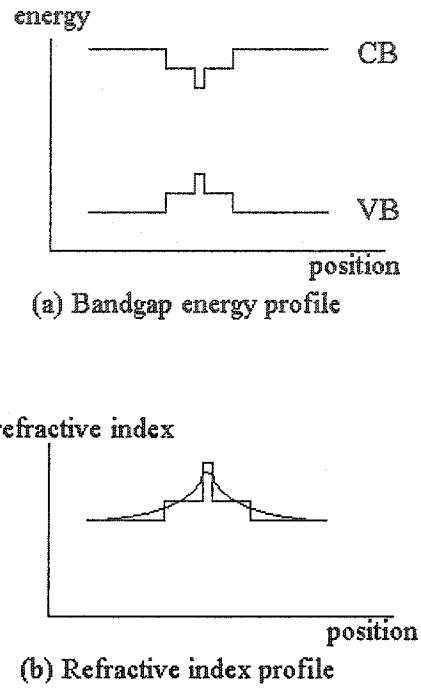

Fig. 2.5 (a) Bandgap energy and (b) refractive-index profiles of a QW laser structure. The curve shown in (b) is the calculated modal profile of the fundamental transverse mode of the waveguide.

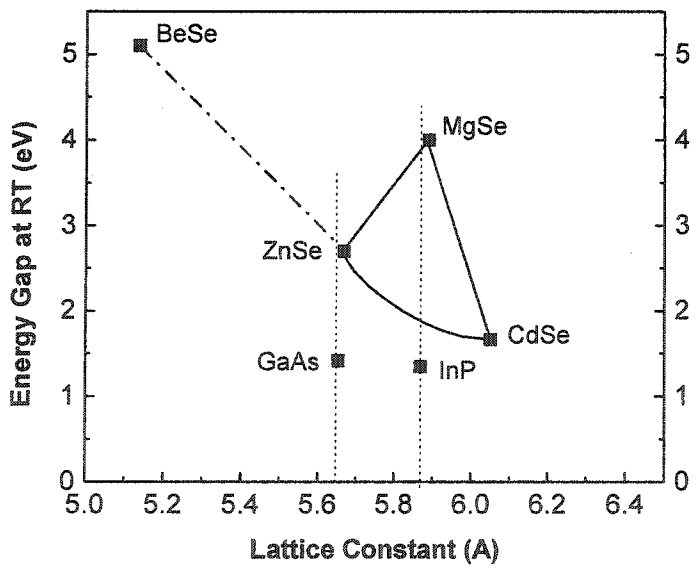

Fig. 2.6 Band gap energy vs. lattice constant for some selected semiconductors

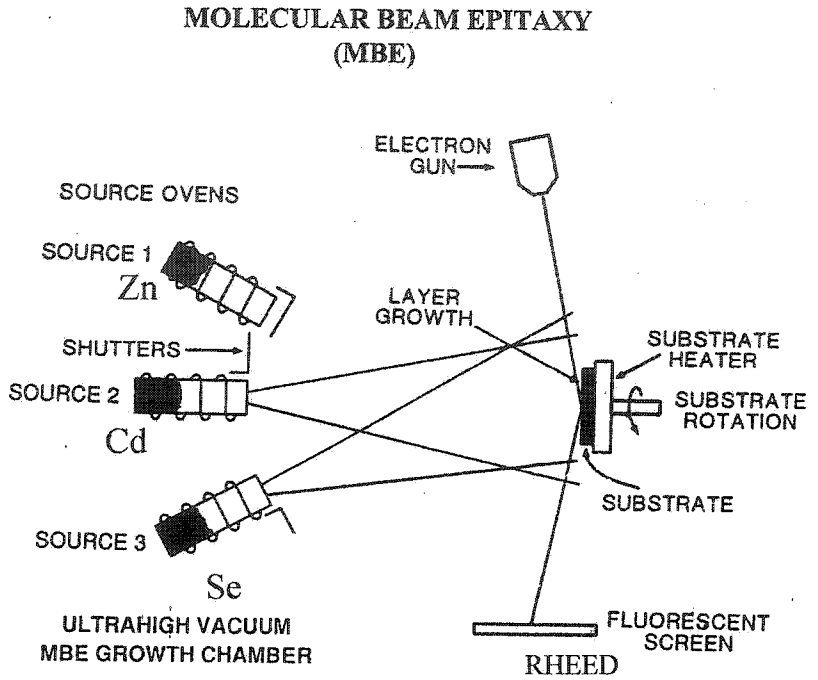

Fig. 2.7 Conceptual schematics of MBE chamber for ZnCdSe growth

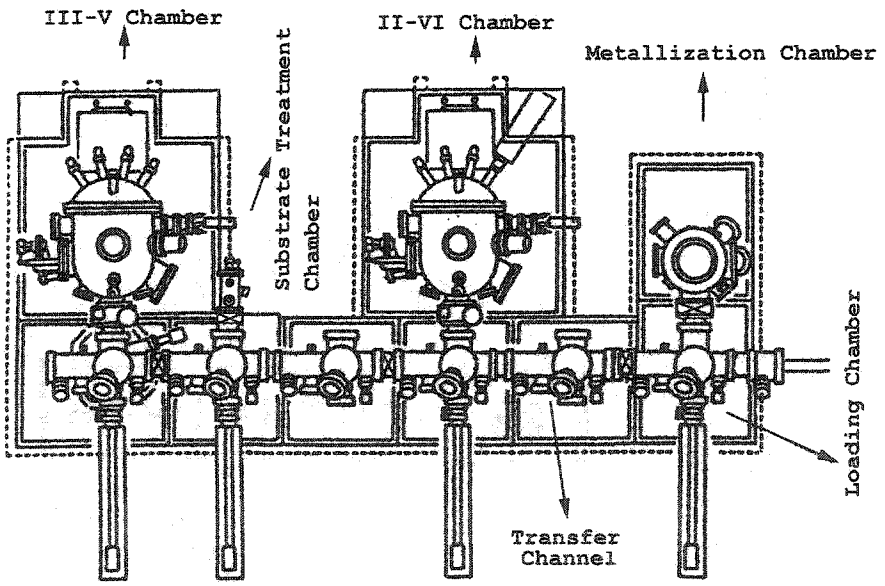

Fig. 2.8 Riber 2300 MBE System

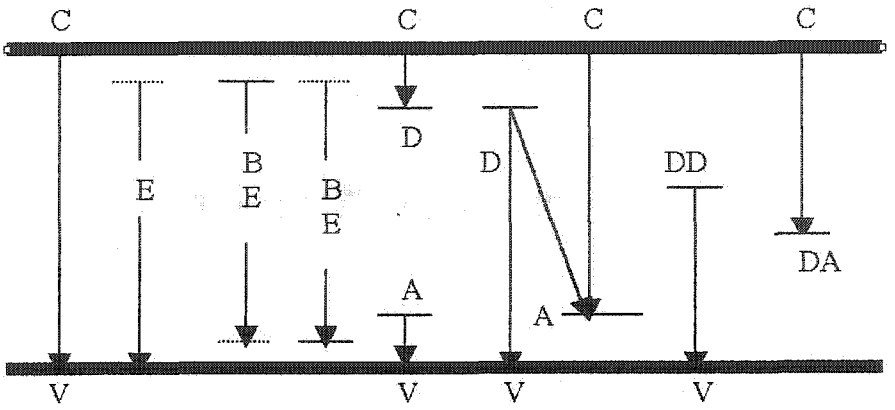

Fig. 2.9 Schematic diagram of the fundamental transitions

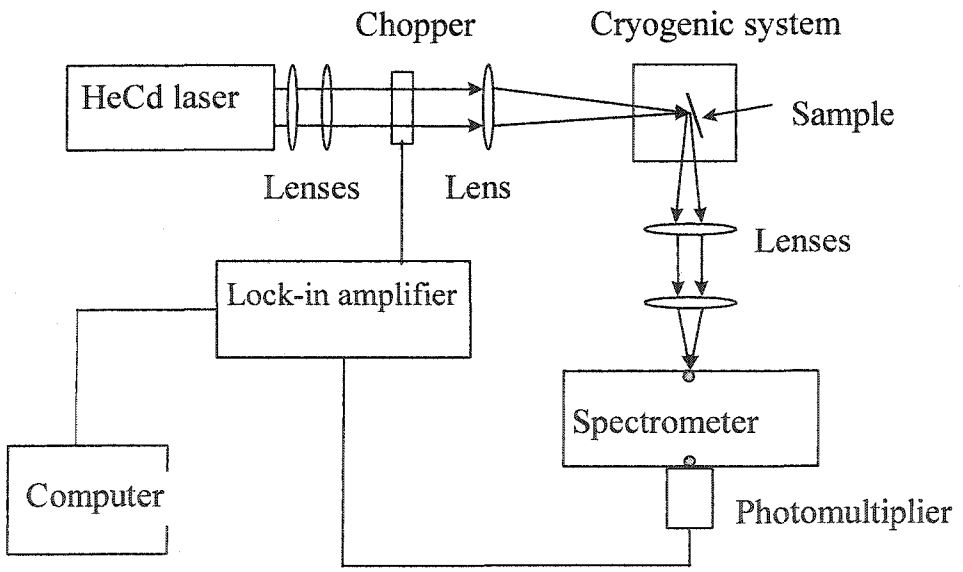

Fig. 2.10 Schematic diagram of the steady state PL setup

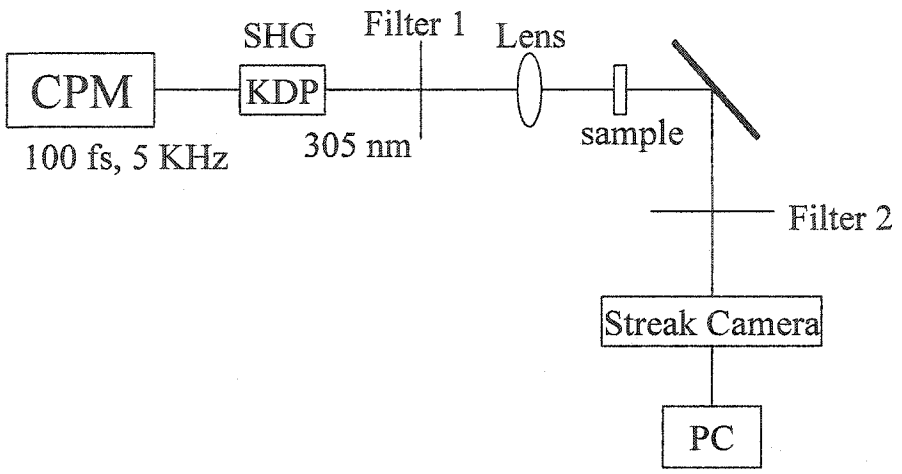

Fig. 2.11 Schematic diagram of the set up for the TRPL measurement

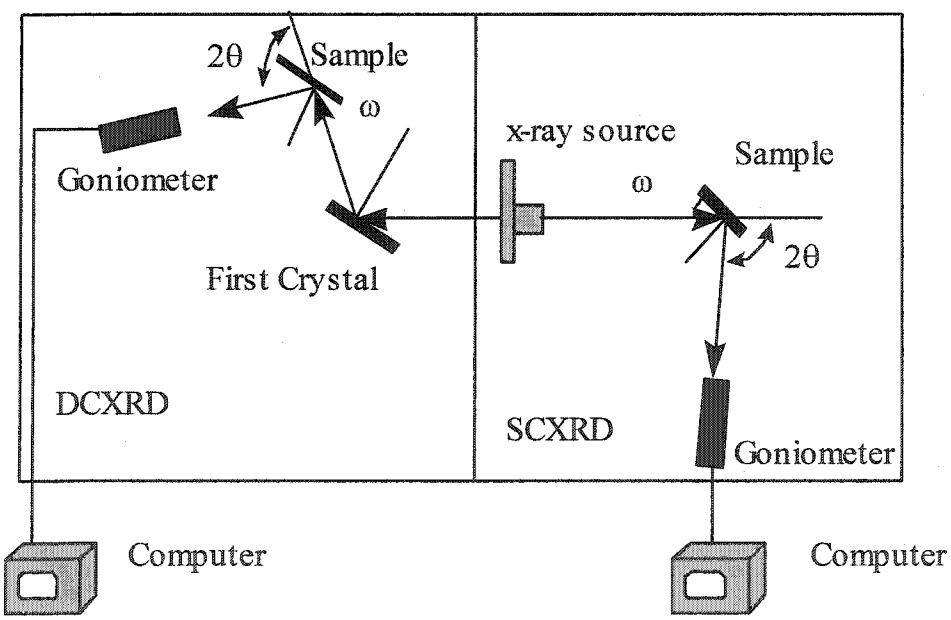

Fig. 2.12 X-ray diffraction system

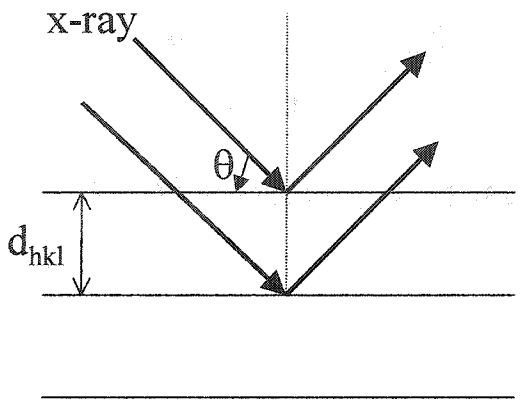

Fig. 2.13 Principle of X-ray diffraction

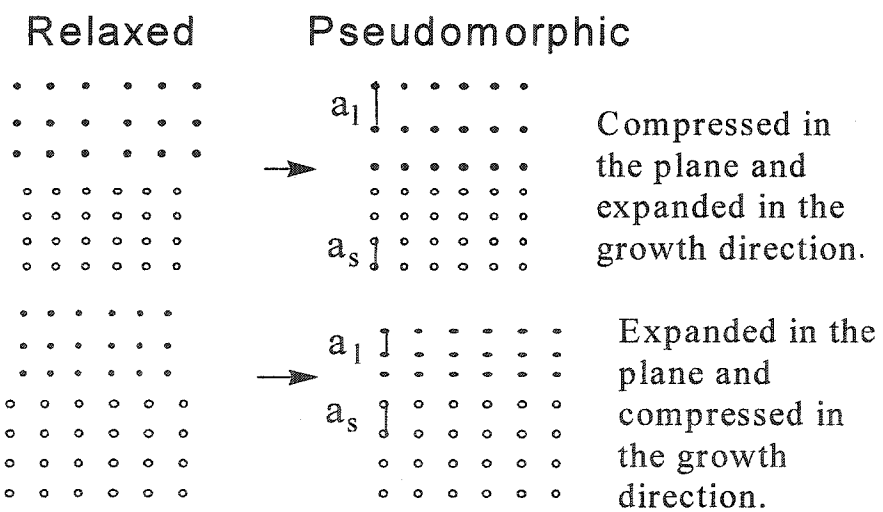

Fig. 2.14 Possible strain states in the epilayers

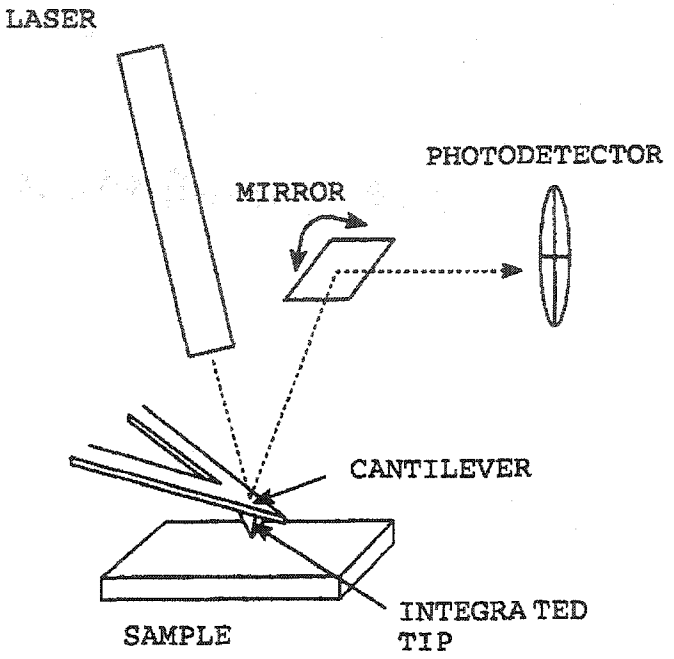

Fig. 2.15 Force sensor in contact AFM

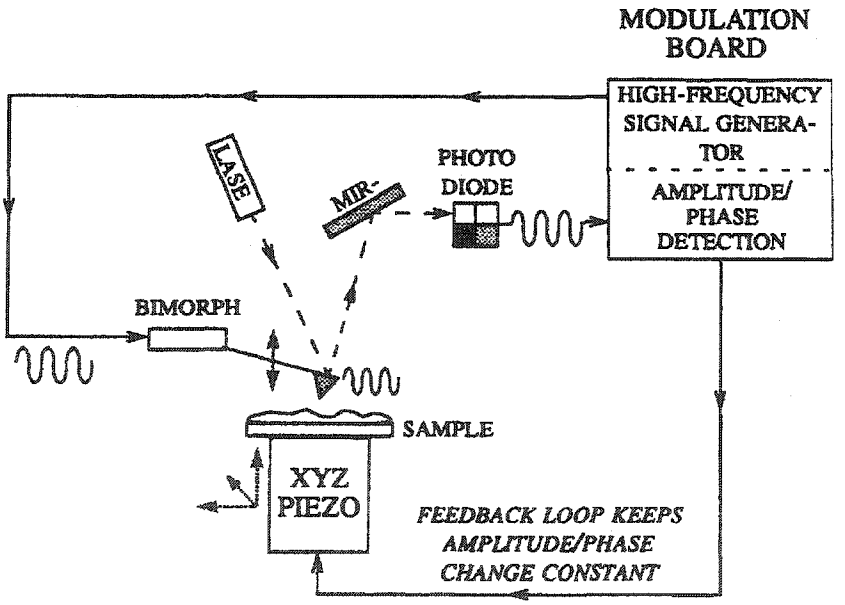

Fig. 2.16 Non-contact feedback loop

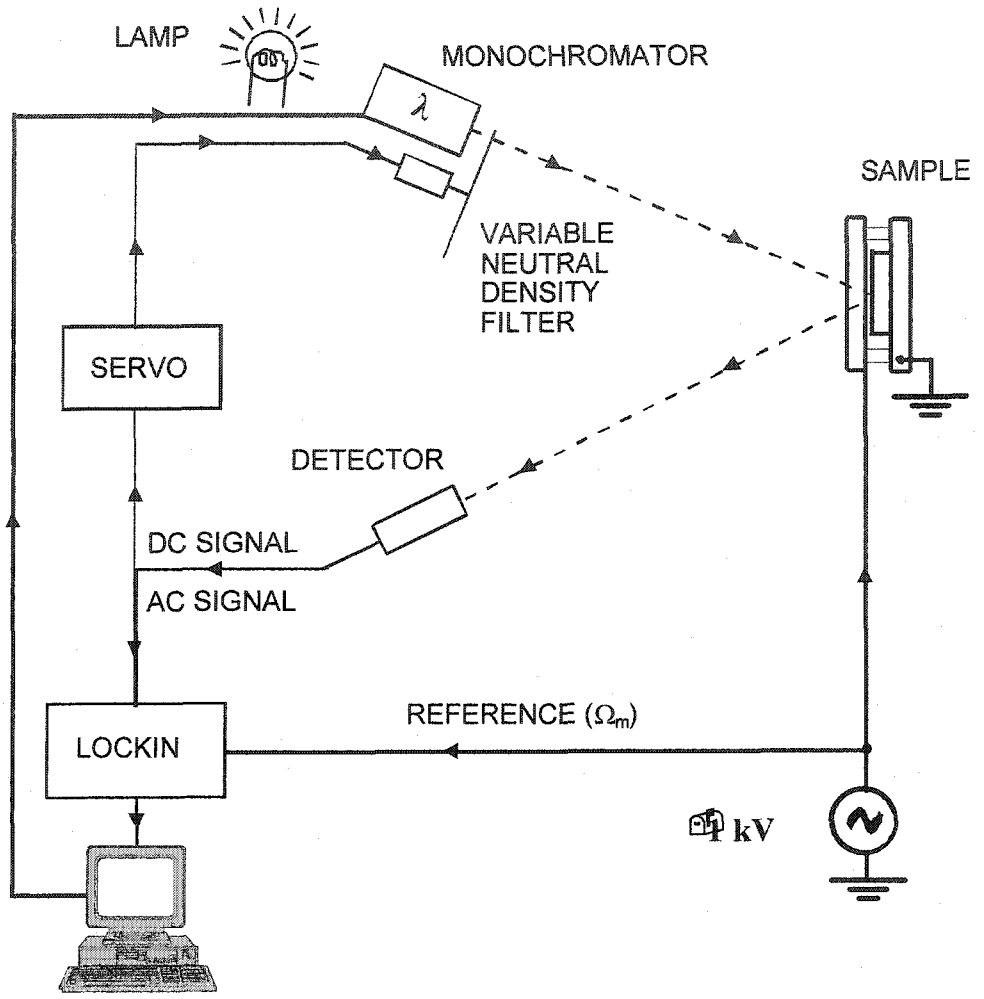

Fig. 2.17 Schematic representation of the contactless electroreflectance setup in Brooklyn College

Chapter 3

Photoluminescence Properties of $Zn_xCd_yMg_{1-x-y}Se$ Alloys Grown by Molecular Beam Epitaxy

3-1. Basics

3-1-1. Common-anion Rule

A solid is formed by atoms brought together. As many atoms approach each other, their valence electrons begin to interact, the electronic wave-functions which are the appropriate solutions of the Schrödinger equation for the interacting atoms are no longer the free-atom atomic orbitals but instead can be thought of as corresponding to overlapping, hybridized orbitals. Bands of allowed states separated by an energy gap are formed due to the overlapping. The degree of overlap and the resulting energy-band structure of the valence electrons determine whether the solid will be a metal, semimetal, semiconductor, or insulator. The energy gap can be filled with a great variety of allowed states. The optical properties of the semiconductors rely on the transitions between these various states.

It is known[1] that the zone-center valence-band maximum (VBM) in a binary zinc-blende semiconductor consists almost exclusively of anion valence *p* orbitals while the conduction-band minimum (CBM) consists almost exclusively of cation valence *s* orbitals. It was therefore initially expected[1-8] that the VBM energies of two common-anion semiconductors which share the same crystal structure and the lattice constant would be nearly equal. Then the "common-anion rule" was formulated based on these

expectations. The "common-anion rule" states that the offset ΔE_{VBM} between the VBM energies of two covalent semiconductors reflects primarily different anion energies, and hence would nearly vanish for semiconductors sharing a common anion. Similarly, the "common-cation rule" states that the offset ΔE_{CBM} between the CBM energies of two covalent semiconductors reflects primarily different cation energies, and hence would nearly vanish for semiconductors sharing a common cation. For examples, ΔE_{VBM} between ZnSe and CdSe is very small since ZnSe and CdSe have common Se anion; while ΔE_{CBM} between ZnSe and ZnTe is very small because ZnSe and ZnTe share common Zn cation.

3-1-2. Localization Due To Compositional Disorder

Disorder is an inherent property of solid solution and can have various forms. Roughly speaking it can be subdivided into compositional and positional types.[9]

In the case of disorder in alloy semiconductors, the disorder is introduced by the statistically distributed occupation of anion (or cation) sites with different atoms. In this compositional disorder case, the composition has fluctuations on a microscopic scale, so that there is in some places a little more one type of atom, in others more the other type of atoms. This will result in fluctuations in the conduction and valence energies as functions of the coordinate in the real space. (see Fig. 3.1(a)). Consequently, the electron (hole) can be trapped in the potential well formed by fluctuations in the conduction (valence) band. Thus, excitons formed with at least one carrier localized by such potentials, would be localized as well. We note that such a localized exciton can be formed also in the case when only one of the carriers is localized.

Qualitatively, the condition for the appearance of localization can be written as:

$$E_W > \eta^2 / m^* a^2, \tag{3-1}$$

where E_w is the potential well depth, m^* is the effective mass of a carrier, and a is the spatial size of the well. Based on the "common-anion rule" and "common-cation rule", we can assume that in semiconductors with common anion, the potential fluctuations will mostly take place in the conduction band and will act predominantly on electrons whereas in semiconductors with common cation the holes will be subjected to potential fluctuations of the valence band. In accordance with Eq. (3-1) it is clear that localization of more heavy carriers (the holes) needs the potential wells of smaller depth and extension. As a result, for a potential relief of given amplitude the appearance of localized states is more probable in semiconductors with common cation.

The potential fluctuations in the energy band will lead to the appearance of tails of localized states, which is shown in Fig. 3.1(b). The effect of disorder (potential fluctuation) on electronic states of solid can be most easily studied at the band edges through the broadening of the optical spectra due to formation of the band tails.

3-2. Introduction

Semiconductor alloys have been widely used for light emitting devices largely due to the flexibility to control changes in the band gap energy and lattice constant. Specifically, ZnCdMgSe-based light emitting diodes (LEDs)[10,11] and optically pumped laser structures[12,13] operating in the visible range of the spectrum have been reported by several research groups. Such structures are usually grown on InP substrates. Thus, by choosing appropriate composition of Zn, Cd, and Mg, emissions at different wavelengths

can be achieved while lattice-matching to InP is maintained. $Zn_xCd_yMg_{1-x-y}Se$ alloys with high crystal quality are crucial for the fabrication of long-lived devices. Furthermore, the knowledge about the optical properties of such alloys is very important for proper device fabrication.

It has been reported[14,15] that band edge PL from $Zn_xCd_yMg_{1-x-y}Se$ alloys is relatively broad comparing to that from ZnCdSe. We note that other Mg containing alloys also exhibit broad low temperature PL[16]. This differs from most II-VI common-anion alloys, where the band-edge PL is quite narrow, while in the alloys with common cation the PL is usually broad and relatively deep (for good discussion see Refs. 9,17). Indeed, in the case of common anions the fluctuations are associated with the conduction band and thus exciton localization occurs via electron trapping, which requires strong fluctuations. For instance, it has been shown that the PL from ZnCdSe is dominated by free excitons, and that the potential fluctuations only limit the free exciton diffusion length and do not affect the PL emission significantly[17]. On the other hand, when the potential fluctuations arise from the valence band, the localization is quite probable because of large hole mass, and localized excitons have been readily observed (see e.g., Ref. 18 and references therein).

Thus, the origin of broad low temperature PL from $Zn_xCd_yMg_{1-x-y}Se$ requires a careful investigation. Previously[14], this has been explained by the sum of free and localized exciton recombinations, with the former dominating the PL. The presence of both free and localized exciton transitions was postulated based on the assumptions that the asymmetric PL can be fitted by two Gaussians and that the observed non-exponential PL decay can be fitted by two exponentials[14]. However, it is also well known that such

asymmetric line shapes with tail on the low energy side as well as a non-exponential PL decay are the hallmarks of systems with potential fluctuations.[19,20]

Therefore, we systematically investigate optical properties of high quality $Zn_xCd_yMg_{1-x-y}Se$ alloys grown nearly lattice-matched on InP[21] to clarify the origin of this PL. We shall definitely show by PLE as well as by temperature and excitation dependent PL that the excitons localized by potential fluctuations, which arise from incorporation of Mg, play a dominant role in the low temperature PL emission. We shall discuss this phenomenon in terms of a large valence band offset (VBO) in Zn(Cd)Se/MgSe systems, which is anomalous for common anion alloys.

3-3. MBE Growth of $Zn_xCd_yMg_{1-x-y}Se$ alloys

The samples were grown on epi-ready (001) InP substrates by MBE in a Riber 2300 system described in section 2-2. Oxide desorption of the InP substrate was performed in the III-V chamber by heating to ~ 490°C with an As flux impingent on the InP surface, after which a 120 nm lattice matched InGaAs buffer layer was grown. Then the substrate with the buffer layer was transferred in UHV to the II-VI chamber for the $Zn_xCd_yMg_{(1-x-y)}Se$ alloy growth. Prior to the growth of quaternary $Zn_xCd_yMg_{(1-x-y)}Se$, a Zn irradiation of the InGaAs buffer layer surface was performed and a 10 nm thick low temperature ZnCdSe interfacial layer was grown at 170°C in order to improve the crystalline quality.[22]The growth was initiated at a low temperature of 170°C for 1 minute. Then the substrate temperature was raised to the typical II-VI growth temperature of 270°C and a 1 μm high-band gap $Zn_xCd_yMg_{(1-x-y)}Se$ epilayer was grown, followed by a 10 nm ZnCdSe cap layer to protect the $Zn_xCd_yMg_{(1-x-y)}Se$ from oxidation by atmospheric

oxygen. All the $Zn_xCd_yMg_{(1-x-y)}Se$ epilayers were nearly lattice matched to InP substrate ($\Delta a/a<0.2\%$) as confirmed by x-ray studies. The concentrations of all the samples are obtained based on the x-ray studies.

3-4. Photoluminescence Properties of $Zn_xCd_yMg_{1-x-y}Se$ Alloys

We show in Fig. 3.2 the low temperature (T=10K) PLE spectra detected at the PL peak energy as well as corresponding PL spectra for samples with various Mg concentrations ([Mg]). All the samples exhibit a single asymmetric PL peak, whose width increases with increasing Mg concentration. The PLE spectra for the alloys with low [Mg] exhibit a relatively flat initial baseline, as expected for above bandgap excitation, which is followed by the peak with a relatively sharp low energy side. For samples with high [Mg] this peak merges with the band-edge and becomes less distinguishable; also the lower energy tail becomes longer.

It has to be noted that if free excitons (FX) are to dominate the PL as suggested in Ref. 14, no such peak should be observed in PLE. However, if the PL is dominated by localized excitons, one would expect to see a FX line in PLE spectra. Thus we attribute the observed PLE peak to a free excitonic transition and the low temperature PL to exciton localized by potential fluctuations. Consequently, the energy difference (ΔE) between PLE and PL peaks would correspond to the average localization energy and thus ΔE should increase with increasing magnitude of the potential fluctuations. Indeed, as seen from the inset in Fig. 3.2, ΔE increases from 24 meV in the sample with [Mg]=11% to 120 meV in the sample with [Mg]=53%. Therefore, we conclude that the potential

fluctuations become stronger with larger [Mg], resulting from increased compositional disorder. This also explains the broadening of the PL with increasing [Mg].

Studies on the temperature-dependent PL further confirm our conclusions. In Fig. 3.3, we plot the PL peak position as a function of temperature for samples with various [Mg]. It is interesting that for samples with lower [Mg] (the lower two curves), the PL peak first follows the temperature dependence of the bandgap (the CdSe bandgap[23] in this case) up to T= 40 K, then it shifts to higher energies up to T= 80 K, and afterwards it starts following the bandgap again. For the samples with higher [Mg] (the upper two curves), it first shows a red-shift relative to the bandgap, then it shifts to higher energies, exhibiting a so-called "inverted-S" shape that has been routinely observed in disordered systems.[24,25] We note that such a behavior cannot be explained within the model proposed in Ref. 14, since if FXs dominate, the PL would closely follow the bandgap as a function of temperature. On the other hand, such a behavior is easily explained within the model of localized excitons as follows. The PL blue-shift of samples with lower [Mg] is due to ionization of excitons localized by rather shallow potentials, after which the PL is dominated by free excitons, which then follow the temperature dependence of the bandgap. For samples with higher [Mg] (stronger potential fluctuations), the ionization of excitons localized by shallow potentials also occurs as the temperature increases; however, excitons localized by deep potentials start to dominate at intermediate temperatures, which contributes to the red-shift of the PL. As the temperature increases further, almost all the localized excitons are ionized and become free excitons, which results in the blue shift of the PL.

Studies of PL as a function of excitation intensity also corroborate our model. In Fig. 3.4 we plot PL of various $Zn_xCd_yMg_{1-x-y}Se$ alloys under two different excitation intensities; all the samples[26] exhibit a blue shift with increasing excitation intensity and the magnitude of the shift is larger in samples with higher [Mg] (see the inset in Fig. 3.4). Such a behavior is attributed to the effect of filling of shallower localized states as the quasi-Fermi levels move closer to the corresponding band-edges.[19,27]

Therefore, based on the above, we conclude that the low temperature PL of $Zn_xCd_yMg_{(1-x-y)}Se$ alloys is primarily due to excitons localized at the potential fluctuations arising from compositional disorder. Having established the PL emission mechanism, we then proceed to explain the origin of the exciton localization in this common anion alloy. As mentioned above, it has been argued that in alloys with cation substitution the potential fluctuations are associated mostly with the conduction band, and thus exciton localization occurs via electron trapping, which requires very large fluctuations. On the other hand, when the potential fluctuations are associated with the valence band, the localization is quite probable because of large hole mass. Thus the appearance of the localized excitons in $Zn_xCd_yMg_{(1-x-y)}Se$ suggests that the presence of Mg breaks down the "common-anion rule". Indeed, this alloy differs from many other II-VI common-anion systems by the fact that the VBO between MgSe and Zn(Cd)Se is rather large (0.8-1 eV).[28,29] This has also been observed in some other common-anion systems (e.g. AlAs/GaAs[30], CdTe/HgTe[31], and AlN/GaN[32]), which contain cations with and without d-orbitals. It has been shown[33] that the cation d-orbitals can interact with anion p-orbitals, and such an interaction modifies valence band maximum. As a result,

the VBOs between materials containing cations with (Zn(Cd)Se) and without d-orbitals (MgSe) are enhanced.

The VBO values between MgSe and Zn(Cd)Se are comparable to those of common-cation systems. Thus, even relatively small quantities of Mg added to ZnCdSe will lead to significant modifications in the PL properties due to appearance of rather strong potential fluctuations associated with the valence band, which we indeed have observed.

In summary, we have shown that at low temperatures (T=10 K) PL from $Zn_xCd_yMg_{1-x-y}Se$ is dominated by excitons localized by potential fluctuations due to compositional disorder and that the magnitude of the fluctuations increases with increasing Mg concentration. Such potential fluctuations serve as a manifestation of breakdown of the "Common-anion Rule" in some Mg-containing alloys.

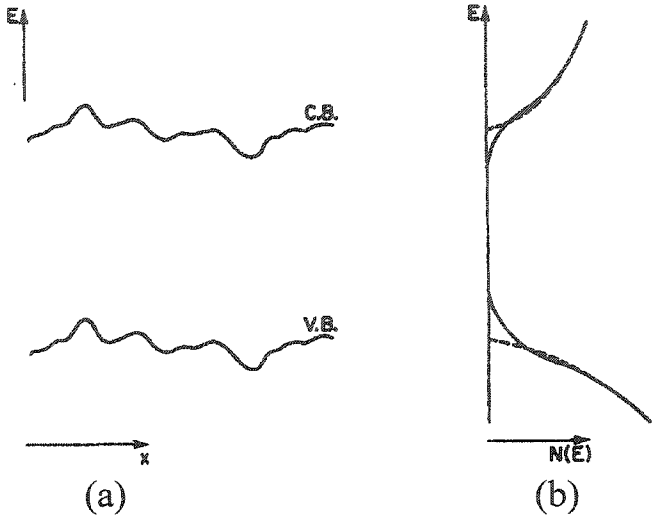

Fig. 3.1 (a) shows the perturbation of the band edges by potential fluctuation as a function of coordinate in real space. This leads to the formation of tails of states shown on (b) where the dashed lines show the distribution of states in the unperturbed case.

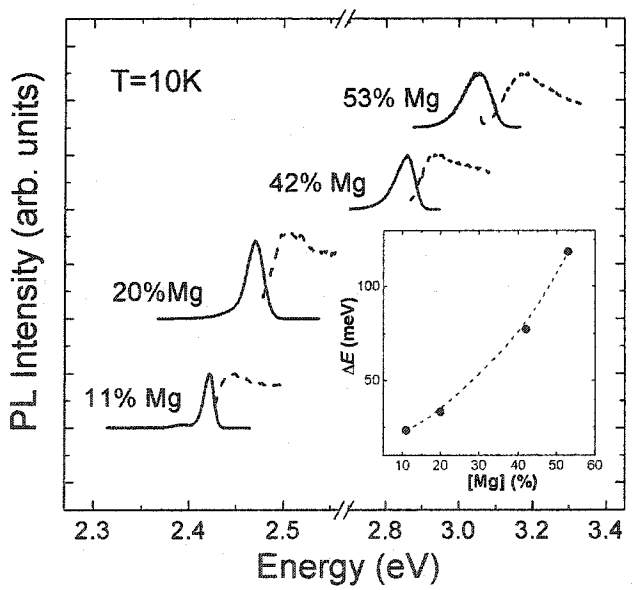

Fig. 3.2 PLE (dotted lines) and PL (solid lines) of $Zn_xCd_yMg_{1-x-y}Se$ alloys with various Mg concentrations at T=10K. The inset: the energy difference (ΔE) between PL and PLE peaks as a function of Mg concentration; the dotted line is the guide for eyes.

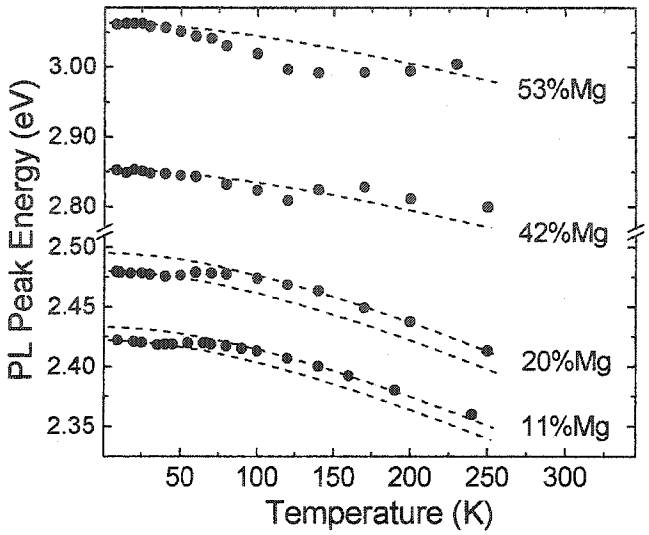

Fig. 3.3 PL peak energies (solid circles) as a function of temperature for samples with various Mg concentrations. The dotted lines represent the temperature dependence of the CdSe bandgap energy (shifted for easier comparison).

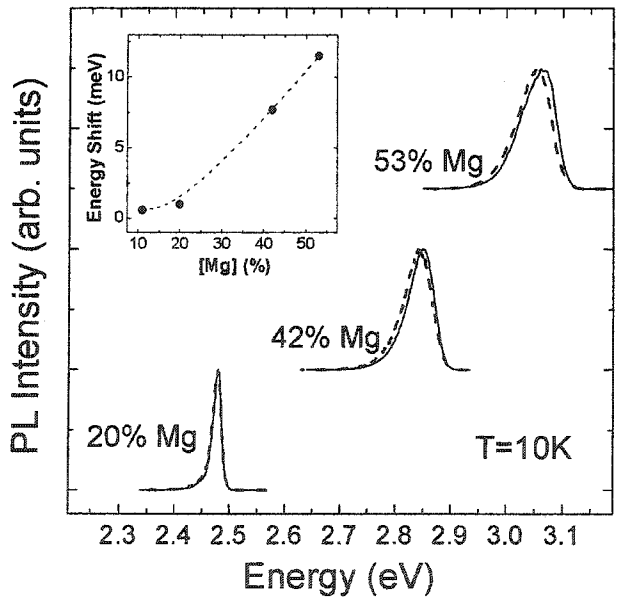

Fig. 3.4 PL spectra of $Zn_xCd_yMg_{1-x-y}Se$ alloys with various Mg concentrations as functions of excitation intensity at T=10K (Solid lines represent the highest excitation intensity, and dashed lines represent the excitation intensity about two orders of magnitude lower). The inset: the peak shift as a function of [Mg]; the dotted line is the guide for eyes.

Chapter 4

Characteristics Studies of Optically-Pumped Blue $Zn_x Cd_y Mg_{1-x-y} Se/Zn_x Cd_y Mg_{1-x-y} Se$ Single Quantum Well Lasers on InP By Molecular Beam Epitaxy

4-1. Introduction

The first demonstration of a blue-green ZnSe-based laser diode (LD) in 1991[1] marked, in fact, an era in the development of semiconductor lasers, expanding the area of their potential applications to the whole visible and UV spectral range. Considerable progress has been achieved in the following years, resulting in the realization of CW room temperature (RT) green LDs with lifetimes as long as 400 h in 1997.[2] It turned out that the degradation problems were intractable with the underlying reasons being unclear at the time.

Stimulating the development of other wide gap semiconductors for visible and UV applications, the II-VI studies were severely affected by the breakthrough in III-Nitrides (III-N) resulting in commercially applicable LD lifetimes of ~ 10000 h under CW RT operation at an emission wavelength of ~ 405 nm in 1998.[3] Nevertheless, the great expectations of easily expanding the III-N-based LDs to the blue-green spectral range have faced basic material problems in InGaN/AlGaN heterostructures with high In content, such as phase separation,[4] causing a much faster device degradation than in the case of II-VI LDs.

Other possible competitors of the II-VIs in the green range coming from the "yellow" side - the group III phosphides - are used for the commercial fabrication of red lasers in the 630-670 nm wavelength range[5] and bright LEDs with emission through greenish-yellow to orange.[6] In the beginning of the nineties significant efforts were made to reach the green range with LDs based on AlGaInP-based heterostructures. A shortest LD wavelength of 555 nm was demonstrated under cw conditions at 77 K.[7] Whereas for the RT devices a decrease in the lasing wavelength from 615 nm[8] through 607 nm[9] to 586 nm[10] was accompanied by a consequent variation of the lasing conditions from cw through pulsed to optically pumped conditions. The fundamental reason for this is that the lattice-matched layer of AlInP has a band gap very close to the AlGaInP QW, strongly limiting the carrier confinement in the AlInP/AlGaInP QW.

Summarizing, the blue-green spectral range (470-550 nm), which is extremely important for many applications such as a projection TV, pointers and alignment devices, plastic fibers etc., and which moreover corresponds to the maximal sensitivity of the human eye, is naturally covered by ZnSe-based wide gap II-VI LDs grown on GaAs.[1] One of the major obstacles limiting the lifetime of ZnSe-based devices grown on GaAs is the pre-existing defects and the formation of dislocation networks in the active region due to recombination-enhanced defect migration. It is reported that the degradation of ZnSe-based II-VI LDs grown on GaAs substrates originates at pre-existing defects (mainly stacking faults) and propagates by the formation of <100> dark line defects (DLDs) in or near the active layer. [11,12] The formation of DLDs is observed in both electrical and optical injection devices. In the initial state of degradation, DLDs develop along the pathways of dark mobile defects, which originate from pre-existing defects. With time,

the DLDs grow, branch, and broaden forming large areas of nonradiative recombination centers. Spatially resolved cathodoluminescence study shows that nonradiative recombination processes associated with DLDs are thermally activated.[13]

The blue-green spectral range (470-550 nm) could also be naturally covered by ZnCdSe/ZnCdMgSe QW structure grown lattice-matched on InP, with only varying the thickness of ZnCdSe QW.[14,15] Recently, a material degradation study on the ZnCdSe/ZnCdMgSe QW structures grown on InP shows no sign of the formation of DLDs in the active layer.[16] One may expect long lifetime devices made from this material system. Therefore, the ZnCdSe/ZnCdMgSe material system grown on InP is still of interest in the blue-green spectral region. Since there still exists challenges on the high p-type doping for ZnCdMgSe with high band gap as barrier layers, I choose here to study the photo-pumped blue and green laser structures in order to investigate the characteristics including the structure design of the semiconductor lasers.

Based on ZnCdSe/ZnCdMgSe QWs, optically-pumped laser structures[17] emitting at the spectral range from red to blue has been demonstrated. However, a very thin ZnCdSe well (≤20 Å) must be used in order to achieve blue emission. This results in a broad luminescence emission peak with a FWHM of ~ 70 meV at 10 K due to well thickness fluctuations. The wavelength of the QW emission is also sensitive to the well thickness. Therefore, it is difficult to obtain reproducible blue emission energies by controlling the well thickness in MBE growth. A $Zn_{x'}Cd_{y'}Mg_{1-x'-y'}Se/Zn_xCd_yMg_{1-x-y}Se$ QW structure using a quaternary $Zn_xCd_yMg_{1-x-y}Se$ layer with a band gap of ~ 2.5 eV instead of a ternary $Zn_xCd_{1-x}Se$ layer as the QW layer has been grown[18] to achieve emission in the blue range with a thicker well, resulting in a narrower emission linewidth,

increased reproducibility and excellent optical characteristics. In this thesis, we report the operation of photo-pumped blue lasers made from $Zn_{x'}Cd_{y'}Mg_{1-x'-y'}Se/Zn_xCd_yMg_{1-x-y}Se$ single QW (SQW) laser structures grown on InP with quaternary $Zn_xCd_yMg_{1-x-y}Se$ as the QW material. By varying the QW composition we obtained lasing emission in the green region as well. The properties of these lasers are compared and explained on the basis of the differences in their confinement. The temperature dependency of the threshold pumping intensity can be fitted by a simple Arrhenius behavior $I_{th}(T)=C*exp(-E_a/kT)$ with an activation energy E_a very close to the band gap energy difference between the cladding layer and the quantum well. This points to a carrier loss process through thermalization into the cladding layer and subsequent diffusion away from the quantum well.

4-2. MBE Growth of the Laser Structures

The schematic of the separate confinement heterostructure $Zn_{x'}Cd_{y'}Mg_{1-x'-y'}Se$ /$Zn_xCd_yMg_{1-x-y}Se$ SQW laser structure and its band gap profile are shown in Fig. 4.1. The samples were grown on (001) epi-ready InP substrates by MBE in a Riber 2300 system described in section 2-2. Oxide desorption of the epi-ready substrate was performed in the III-V chamber by heating to ~ 490 °C with an As flux impingent on the surface, after which a 160 nm lattice matched InGaAs buffer layer was grown. Then the substrate with the buffer layer was transferred to the II-VI chamber under UHV. Growth of the II-VI material was performed under Se-rich conditions with the growth rate less than 1 μm/hr and a VI/II beam equivalent pressure ratio of ~ 4. Prior to the growth of the laser structure, a Zn irradiation of the InGaAs surface was performed and a 10 nm low

temperature $Zn_xCd_{1-x}Se$ interfacial layer was grown at 170 °C in order to improve the crystalline quality[19]. The substrate temperature was then raised to the typical II-VI growth temperature of 270 °C and the laser structure was grown. The SQW blue and green laser structures are nearly the same. They consist of a $Zn_{x''}Cd_{y''}Mg_{1-x''-y''}Se$ cladding layer (0.5μm, E_g ~ 3.03 eV), a $Zn_{x'}Cd_{y'}Mg_{1-x'-y'}Se$ waveguide layer (0.1μm, E_g ~ 2.78 eV), a single $Zn_xCd_yMg_{1-x-y}Se$ QW (50 Å), a top $Zn_{x'}Cd_{y'}Mg_{1-x'-y'}Se$ waveguide layer (0.1μm, E_g ~ 2.78 eV), a top $Zn_{x''}Cd_{y''}Mg_{1-x''-y''}Se$ cladding layer (0.1μm, E_g ~ 3.03 eV) and a ZnSe capping layer (50 Å). This cap layer was used to protect the top cladding layer from oxidation. All the layers except for the ZnSe cap layer were closely lattice matched to the InP substrate. The only difference between the two structures is the QW composition.

4-3. Optical Confinement Factor Γ

The radiation emitted by the gain medium must be confined in the active region by a waveguide. In a heterostructure semiconductor laser, the electric field confinement in the direction perpendicular to the junction plane occurred through dielectric waveguiding. This mechanism is often referred to as index guiding since the refractive index step (shown in Fig. 2.5 (b)) between the active and cladding layers is responsible for the mode confinement through total internal reflection at the interfaces.

The electric field of an electromagnetic wave propagating in the z-direction along a waveguide is determined by the following equation:

$$\left(\frac{\partial^2}{\partial x^2}+\frac{\partial^2}{\partial y^2}+\frac{\partial^2}{\partial z^2}\right)\vec{E}(x,y,z)+\varepsilon(x,y)k_0^2\vec{E}(x,y,z)=0 \qquad (4\text{-}1)$$

Where $\vec{E}(x,y,z)$ is the electric field, $\varepsilon(x, y)$ is the distribution of the dielectric constant in the (x, y) plane and k_0 is the wave vector in vacuum. Here, we assume that the dielectric constant is independent of z.

One approach to solve the above equation is based on the effective-index approximation. This approach can be applied to the case in which the dielectric constant varies very slowly in the lateral x direction along the junction plane compared to its variation in the transverse y direction (perpendicular to the junction plane). Thus, the electric field can be assumed to be

$$\vec{E}(x,y,z) = \vec{e}\Phi(y)\Psi(x)\exp(i\beta z) \tag{4-2}$$

Where z is the direction of propagation, β is the propagation constant of the mode and $\vec{e}$ is a unit vector in the direction of the polarization.

By substituting into Equation (4-1), we have

$$\frac{1}{\Psi}\frac{\partial^2\Psi(x)}{\partial x^2} + \frac{1}{\Phi}\frac{\partial^2\Phi}{\partial y^2} + [\varepsilon(x,y)k_0^2 - \beta^2] = 0 \tag{4-3}$$

To obtain the solution for the above equations, one must know the distribution of the dielectric constant $\varepsilon(x, y)$ or the refractive index for each layer in the structure.

The loss or gain effect is generally treated as a small perturbation to the eigenvalue problem. This is appropriate for heterostructure semiconductor lasers since the mode confinement in the y direction is mainly caused by the index step at the heterostructure interfaces. The dielectric constant ε is of the form

$$\varepsilon(x, y) = \mu_b^2(y) + \Delta\varepsilon(x) \tag{4-4}$$

Where $\mu_b(y)$ is the structural refractive index distribution whose variation is on the order of 0.1. The small perturbation, $\Delta\varepsilon(x)$, caused by the loss and the contribution of external pumping is on the order of 10^{-3}.

By separating the variables in Equation 4-3, the y-component satisfies the following eigenvalue equation

$$\frac{d^2\Phi}{dy^2} + [k_0^2\mu_b^2(y) - \beta_{eff}^2]\Phi = 0 \tag{4-5}$$

Where β_{eff} is the effective propagation constant and can be determined by solving Equation (4-5). The solution to Equation (4-5) gives the transverse eigenmodes for the structure. In a slab waveguide, it is found that two sets of modes can exist, the TE modes and TM modes, characterized according to their polarization. For the TE modes, the elctric field *E* is polarized along the heterojunction plane, i. e., the polarization vector in Equation (4-2) is along the *x-axis*. For the TM modes, the magnetic field H is polarized along the *x*-axis.

For a heterojunction laser, the modal gain for a specific optical mode is given by

$$\gamma_{mode}(\omega)=\gamma(\omega)\Gamma \tag{4-6}$$

Where $\gamma(\omega)$ is the gain of the bulk material, which is the gain when the entire optical mode is confined in the active layer and Γ is the overlapping factor of the eigenmode with the active layer, defined as

$$\Gamma = \frac{\int_{thickness}\Phi^2(y)dy}{\int_{-\infty}^{\infty}\Phi^2(y)dy} \tag{4-7}$$

Typically, the overlapping factor is on the order of a few percent for QW lasers.

For the blue laser, the eigenmode of the electromagnetic wave in the waveguide was calculated by a computer program, which is based on the theory described above. The refractive-index profile of the waveguide structure was constructed by assuming a refractive index vs bandgap energy relation obtained at 632.8 nm established in Ref. 20. We used the refractive indexes of 2.55, 2.45, and 2.36 for QW, waveguide and cladding, respectively. Fig. 4.2 shows the step-index profile of the waveguide and the calculated intensity distribution of the eigenmode. The optical confinement factor Γ for the fundamental transverse wave is about 1.2%.

4-4. Photo-Pumping Experiment Setup

The experimental setup for photo-pumping is shown in Fig. 4.3 (in the optics lab of Prof. Y. C. Chen in Hunter College). A frequency tripled Nd:YAG laser operating at 355 nm wavelength was used as the pump source. The pulse width and repetition rate of the laser output were 3 ns and 20 Hz, respectively. The samples were thinned to about 100μm thickness and cleaved into 2-mm-wide bar for photo-pumping. The pump beam went through a slit of 100 μm before going onto the surface of the wafer to create a stripe geometry excitation region along the (110) direction. A variable attenuator was used to control the pumping intensity. The edge emission of the laser bar was collected by a microscope objective and focused into an optical multichannel analyzer to determine the spectral characteristics. A boxcar integrator was used to average the pumping power and output power.

4-5. Characteristics Studies of the photo-pumped quantum well lasers

Fig. 4.4 shows the PL spectra at 77 K for our laser structures. Emissions from the cladding layer, waveguide layer and QW were observed. For the blue laser, the emission peak energies are at 3.03 eV, 2.78 eV, 2.66 eV respectively and FWHM are 96 meV, 57 meV and 49 meV respectively; while for the green laser, the emission peak energies are at 3.03 eV, 2.77 eV, and 2.53 eV, respectively and FWHM are 99 meV, 85 meV and 57 meV, respectively. No deep level emission was observed. These results (narrow FWHM as well as absence of deep level emission) indicate very good optical quality of the samples[21]. The (004) DCXRD for the blue laser structure is shown in Fig. 4.5. The FWHM of DCXRD for the cladding and waveguide layers are 49 arcsec and 70 arcsec respectively, indicating high crystalline quality of the structure. Similar X-ray results were obtained for the green laser structure.

Fig. 4.6 shows the output intensity from the SQW laser as a function of pumping intensity at room temperature. The pumping-emission plot exhibited a typical superlinear relation below the lasing threshold and a linear relation above the threshold. The threshold occurs at a pumping power density of 220 kW/cm^2 for the blue laser while it is 160 kW/cm^2 for the green laser. The threshold pumping intensity is influenced by many factors including the laser structure, excitation mode, optical confinement factor, material properties and crystal quality. Our two lasers have the same layer structure. Both have similar high crystalline and optical quality and the threshold intensity measurements were done under identical conditions. Thus, the higher threshold pumping intensity in the blue laser is attributed to its smaller carrier confinement.

Shown in Fig. 4.7 are the spectra of the blue laser emission at 492 nm as a function of optical excitation intensity at room temperature. A clear linewidth narrowing was observed above the threshold. The lasing linewidth is about 5 nm at 420 kW/cm^2 which is two times the threshold, and ultimately became as narrow as 1.9 nm at several times the threshold. The spectral narrowing near the threshold was not as dramatic as normally expected of lasing spectra when the threshold is crossed. The lack of a dramatic narrowing may be attributed to two factors. Firstly, the linewidth of the spontaneous emission of the quaternary materials sample are already considerable narrower than the ternary quantum wells by a factor of two. Secondly, the quantum well levels of the samples are close to the band gap energy of the barrier layers. The coalescence of the quantum well and barrier emissions is evident in the spectrum of the amplified spontaneous emission at 177 kW/cm^2 shown in Figure 4.7. Under high levels of excitation, band filling can result in a widening of the gain profile and less dramatic narrowing of the lasing spectra near the threshold. Similar lack of narrowing in the lasing spectra at threshold is also found in photo-pumped Be-chalcogenide-based single quantum-well lasers[22] in which high levels of excitation and band filling are expected due to lack of waveguide structure for optical confinement. The green lasing emission occurs at 514 nm with a similar behavior as a function of excitation intensity as that shown in Fig. 4.7.

The temperature dependent threshold pumping intensity measurements for this laser structure are shown in Fig. 4.8. The inset of Fig. 4.8 shows the emission intensity as a function of excitation intensity at elevated temperature varying from 288 K to 348 K. A clear threshold behavior was observed up to 348 K. T_0 is estimated to be 35 K from an

exponential relationship between threshold and temperature by an empirical formula shown in Fig. 4.8, where I_0 is the threshold at an arbitrary reference temperature T_1, T is the absolute temperature and T_0 is the characteristic temperature, an impirical number often used to express the temperature sensitivity of threshold. The temperature dependent threshold pumping intensity measurements have also been done for the green laser and in that case T_0 has been estimated to be 60 K. Previous studies of III-V AlGaAs lasers and InGaAsP lasers show that the value of T_0 is affected by the carrier recombination mechanisms[23,24] such as Auger recombination and carrier confinement[25,26]. Since higher bandgap results in smaller Auger coefficient, weak carrier confinement is believed to be the reason for the low T_0 in our $Zn_x{\cdot}Cd_y{\cdot}Mg_{1-x'-y}{\cdot}Se/Zn_xCd_yMg_{1-x-y}Se$ SQW blue laser structure compared to the green laser structure. The temperature dependency of the threshold pumping intensity can be fitted by a simple Arrhenius behavior $I_{th}(T)=C*exp(-E_a/kT)$ with an activation energy E_a = 250±4 meV where C is a parameter depending on electron diffusion coefficient and electron effective mass etc.. This activation energy is very close to the band gap difference of 259 meV between the cladding and the QW in the conduction band assuming $\Delta E_c/\Delta E_v$ = 70/30 where ΔE_c and ΔE_v are the barrier heights in the conduction and valence bands, respectively. This points to a carrier loss process involving thermalization of electrons into the cladding layer and subsequent diffusion away from the quantum well. Similar carrier loss was found in AlGaInP-based laser diodes emitting at 633 nm.[27] The T_0 value may be increased by using multiple-quantum-well active region and by improving carrier confinement between the cladding layer and the QW through changing the cladding layer composition or using an artificial "multi quantum barriers" [28,29].

In summary, laser structures containing a quaternary $Zn_xCd_yMg_{1-x-y}Se$ SQW embedded in a waveguide consisting of two 0.1-μm-thick $Zn_{x'}Cd_{y'}Mg_{1-x'-y'}Se$ layers and $Zn_{x''}Cd_{y''}Mg_{1-x''-y''}Se$ as cladding layers have been grown. The structure is closely lattice matched to the InP substrate and has a good quality indicated by narrow (004) DCXRD curves and narrow PL linewidths at 77 K. We have achieved optically pumped blue lasing at 492 nm and green lasing at 514 nm at room temperature from two SQW laser structures with relatively thick quaternary QWs. The lasing linewidth was ~ 5 nm. The lasing threshold pumping intensity has been measured to be ~ 220 kW/cm^2 for the blue laser and ~ 160 kW/cm^2 for the green laser at room temperature. The T_0 was estimated based on the temperature dependency of threshold pumping intensity. Values of T_0 of ~ 35 K and ~ 60 K were obtained for the blue and green laser, respectively. The higher threshold pumping intensity and lower T_0 value for the blue laser can be ascribed to its shallower carrier confinement. The temperature dependency of the threshold pumping intensity can be fitted by a simple Arrhenius behavior $I_{th}(T)=C*exp(-E_a/kT)$ with an activation energy E_a very close to the band gap energy difference between the cladding layer and the QW. This points to a carrier loss process through thermalization into the cladding layer and subsequent diffusion away from the QW. One way to improve the operating characteristics of the laser is to incorporate QDs in the active region due to the lower dimensionality of QDs as shown in section 2-1-1. The spectrum could be very narrow in energy resulting from the discrete nature of energy for QDs. The threshold pumping intensity could be greatly reduced and the characteristic temperature T_0 could be greatly increased due to the enhancement of the exciton binding energy for QDs.

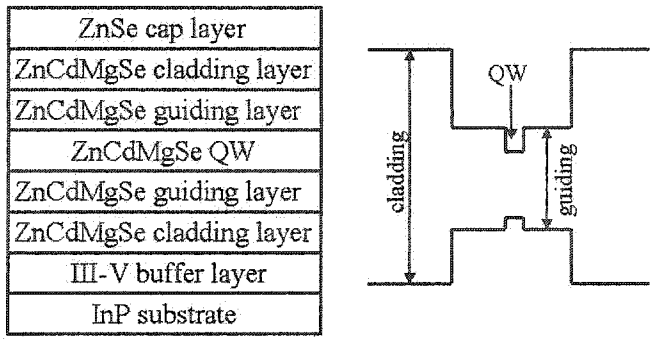

Fig. 4.1 Schematic of the separate confinement heterostructure laser structure grown and its band gap profile

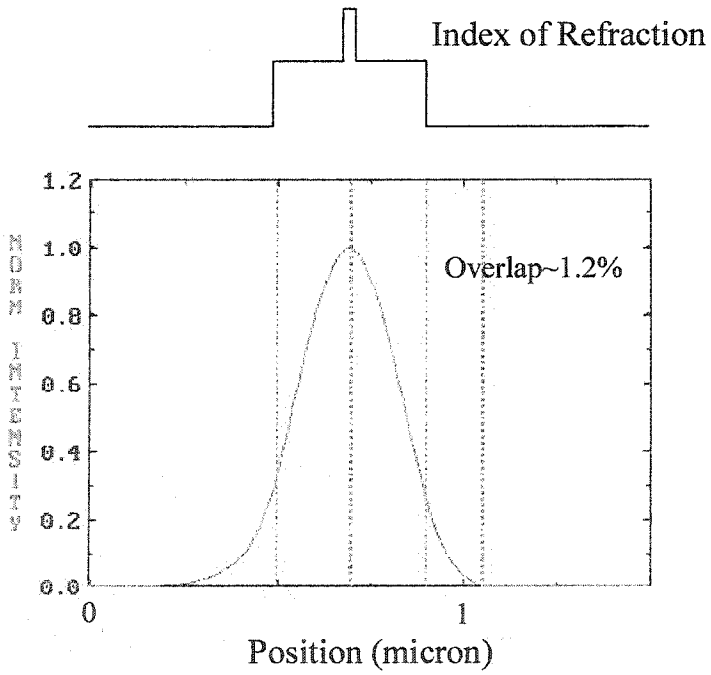

Fig. 4.2 TE mode for the blue laser. The upper plot is the refractive-index profile. The lower plot is the transverse-electric mode of the electromagnetic wave in the waveguide.

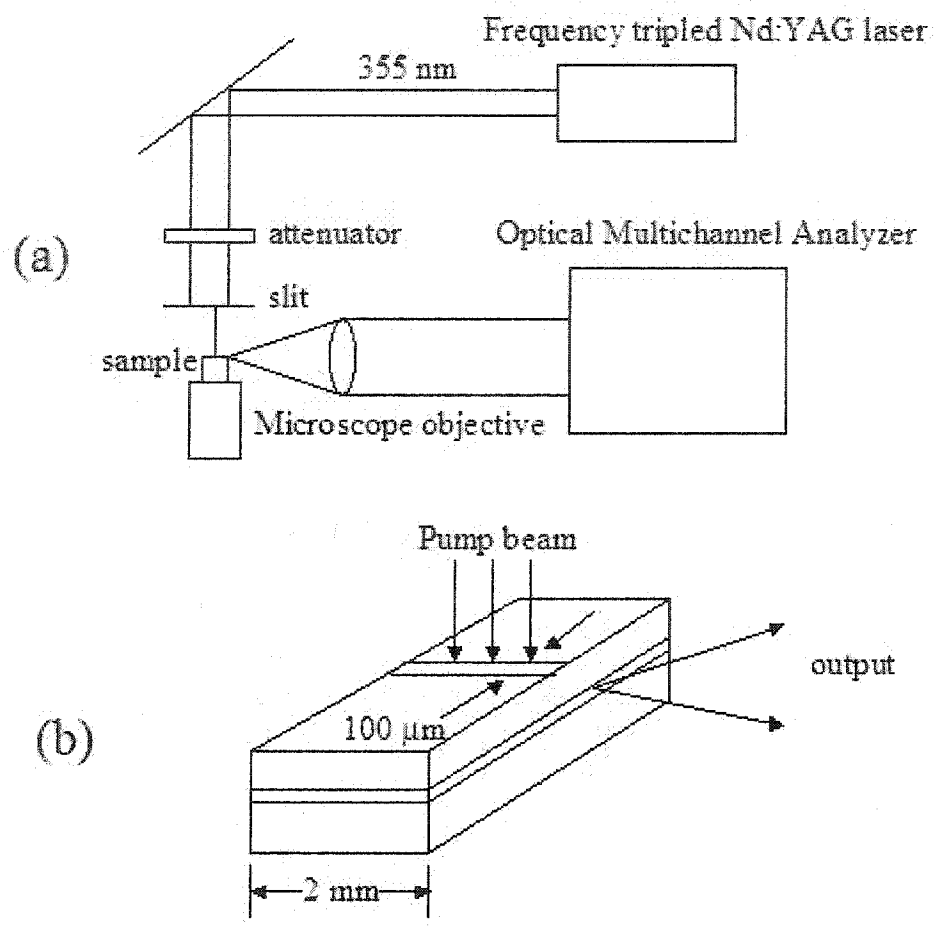

Fig. 4.3 (a) Experimental setup for the photopumping experiment; (b) Pumping geometry on the chip

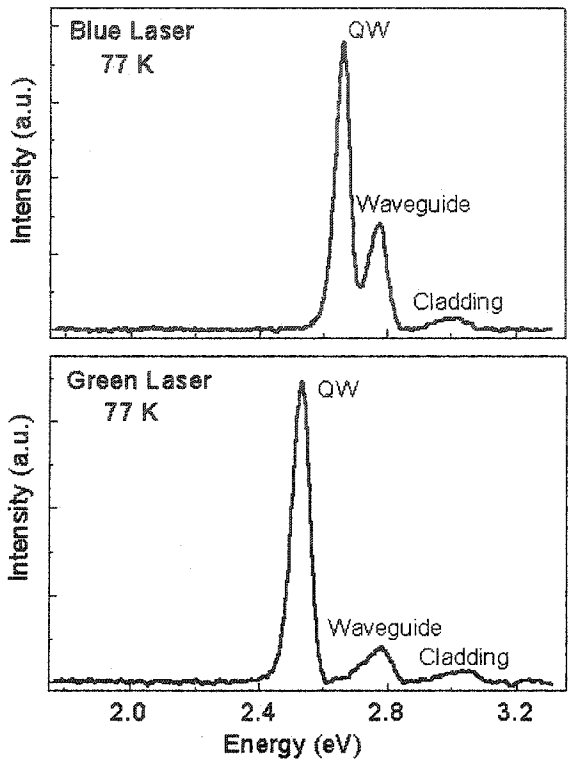

Fig. 4.4 Photoluminescence spectra at 77 K of the two SQW laser structures

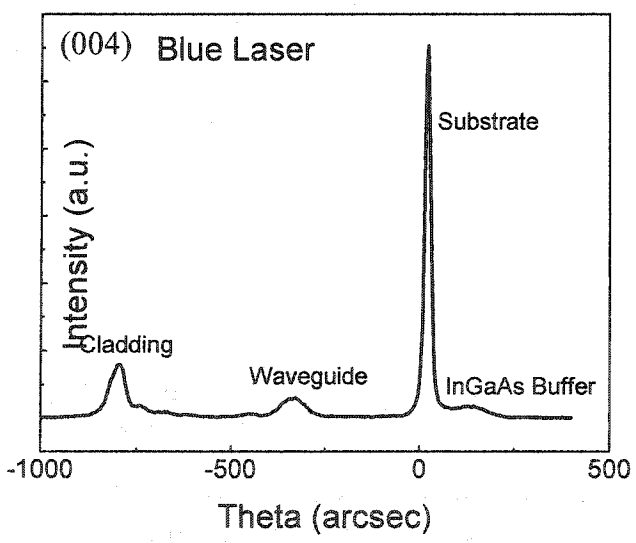

Fig. 4.5 (004) x-ray rocking curve of the SQW blue laser structure. The FWHM of the cladding and guiding layers are 49 arcsec and 70 arcsec respectively.

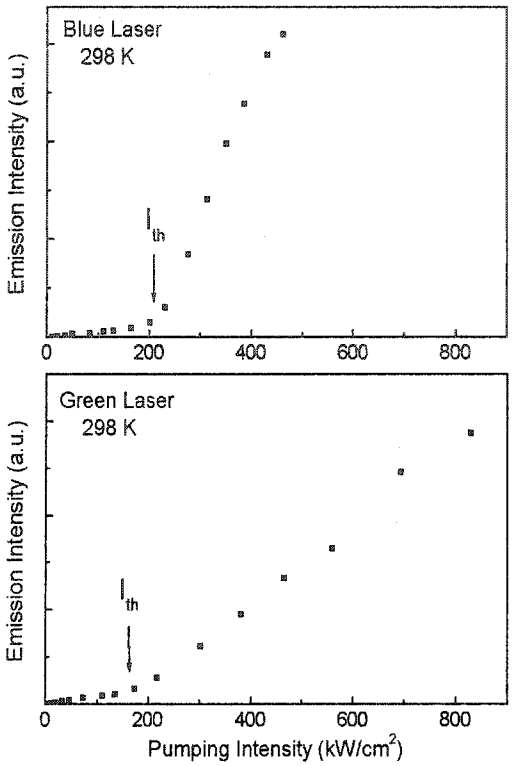

Fig. 4.6 Output intensity vs. pumping intensity at room temperature. The threshold excitation intensity is estimated to be ~ 220 kW/cm^2 for the blue laser and ~ 160 kW/cm^2 for the green laser.

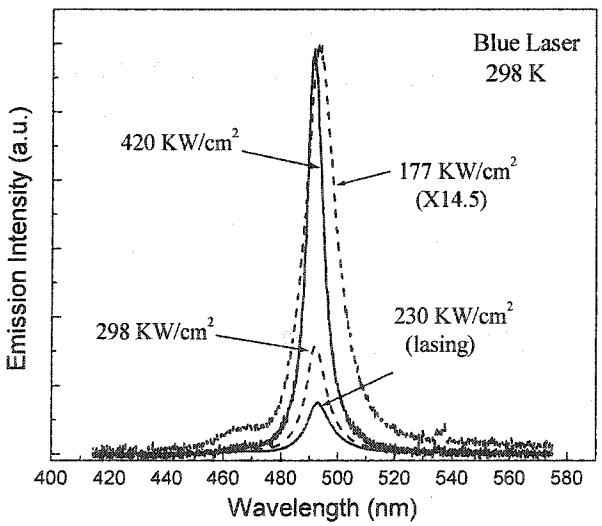

Fig. 4.7 Spectra of blue laser emission at different excitation intensities operated at room temperature. (The spectrum at pumping intensity of 177 kW/cm^2 is amplified by 14.5 times in order to see clearly the emission from barrier.)

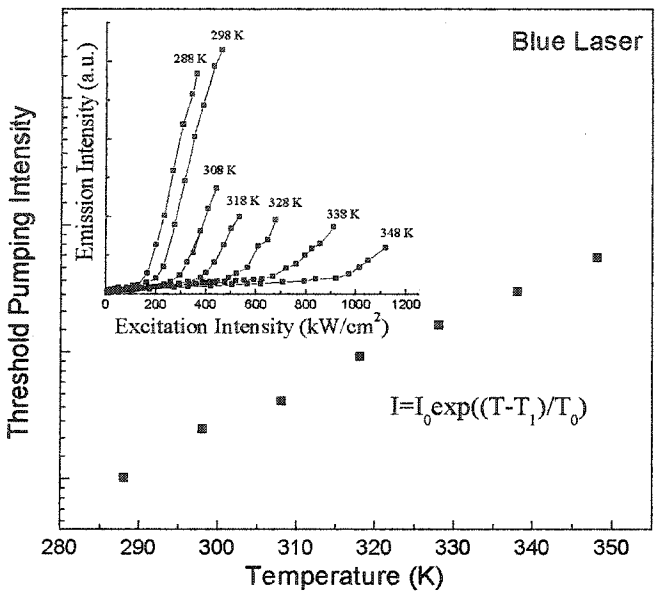

Fig. 4.8 Temperature dependence of the lasing threshold for blue laser structure. Lasing is observed up to 348 K and T_0 is estimated to be 35 K.

Chapter 5

Molecular Beam Epitaxy Growth and Optical Properties of CdSe Self-Assembled Quantum Dots

5-1. Introduction

5-1-1. Historical Developments

By introducing the concept of an electronic "bandstructure" for an ideal crystalline solid, Bloch[1] presented in the late 1920s a revolution in the world of physics dominated by research on atoms. In atoms the energies of bound electrons are discrete and precisely defined within the limit of Heisenberg's uncertainty relation. In solids the electron energy is a multivalued function of momentum resulting in energy bands, continuous densities of states, and gaps. The wavefunctions became completely delocalized in real space. Central in Bloch's theory is an infinite extension of the regular array of lattice points in all three dimensions of space. The restriction of the theory to infinite bodies was regarded as being meaningless from any practical point of view, except next to surfaces. Still small crystallites of a few micrometers in size are very large compared to next-neighbor distances. No observable deviations from the predictions for an infinitely extended crystal were expected, even for small objects.

If the carrier motion in a solid is limited in a layer of a thickness of the order of the carrier de Broglie wavelength, one will observe effects of size quantization. The idea of using ultra-thin layers for studies of size quantization effects was already popular by the late 1950s and early 1960s.[2] With the advent of novel epitaxy deposition techniques like molecular beam epitaxy and somewhat later metal organic chemical vapor deposition

in the late 1960s, a clear demonstration of size quantization effects became possible. By the end of 1980s, the main properties of quantum wells and superlattices were rather well understood and the interest of researchers shifted toward structures with further reduced dimensionality-to quantum wires and quantum dots.

Further advances in nanotechnology now permit the fabrication of quantum dots in which the carriers and/or excitons are confined in all three directions. Such QD structures are formed conventionally by various lithographic methods. The lithographic approach, however, generally requires complicated procedures and, more importantly, suffers from the occurrence of inevitable process-induced defects that generally deteriorate the crystal quality of the resulting QD structures, thus offsetting the advantages of their otherwise extremely attractive optical properties, and limiting the feasibility of their practical usefulness.

There are three well-known modes of heteroepitaxial growth (Fig. 5.1): Frank-van der Merwe (1949), Volmer-Weber (1926), and Stranski-Kranstanow (1938).[3] They represent layer-by-layer growth (FvdM, 2D), island growth (VW, 3D), and layer-by-layer plus islands (SK). For the past decade, QDs have been successfully realized with considerably fewer defects by the self-assembling growth mode (SK mode). This mode of growth requires the deposition of several atomic layers of one material on top of another of a different lattice constant under precisely controlled conditions. Due to the stringent requirements of such controlled thin layer deposition, the SK growth mode eluded the crystal growth community for a long time. Recent developments in epitaxial techniques, however, such as metal-organic chemical vapor deposition (MOCVD) and MBE, have finally made it possible to control layer deposition to the degree required by

the SK process. By making the self-assembling processes possible, these advances have in effect opened a new era in nanostructure fabrication, making zero-dimensional geometries a very practical reality.

5-1-2. Fabrication of Self-Assembled Quantum Dots

The self-assembling effects are a general phenomenon of strained heterosystems. It occurs during growth of strained heterostructures. When the lattice constants of the substrate and the crystallized material differ considerably, only the first deposited monolayers crystallize in the form of epitaxial, strained layers with the lattice constant equal to that of the substrate. When a certain thickness (the "critical thickness") is exceeded, a significant strain occurring in the layer leads to the break-down of such an ordered structure and to the spontaneous creation of randomly distributed islands of regular shape and similar sizes. The shape and average size of islands depend mainly on factors such as the amount of strain in the layer as related to the misfit of lattice constants, the temperature at which the growth occurs, and the growth rate.

In order to fabricate QD structures with three-dimensional (3D) confinements by the SK growth mode, the materials involved in the growth must satisfy two requirements. First, there must be lattice mismatch (strain) between the QD material and the substrate. This forces the growth mode to transform, when the critical thickness is reached, from pseudomorphic 2D layer growth into 3D island formation, without forming defects or dislocations. Second, the QD material must have a smaller band gap than the surrounding "matrix" material, so that the dots constitute in effect zero-dimensional potential wells, energetically favorable for quantum confinement of the carriers. Fortunately, the above

two requirements usually go hand-in-hand in most IV-IV, III-V and II-VI families of semiconductors.

About the self-assembled QD formation, there are equilibrium and dynamical theories. A review paper on this could be found in Ref. 4.

The self-assembling growth process has already been shown to produce QDs in the form of coherent nanoscale islands in various combinations of lattice-mismatched IV-IV, III-V, and II-VI materials. However, in contrast to the work already done on the IV-IV[5,6] and the III-V QDs,[7-13] considerably less is known both about the self-assembling formation of II-VI QDs and about their optical properties.[14,15] One of the reasons is because this material system is particularly challenging since due to the small dielectric constant the bulk exciton size is only a few nanometers. Therefore quantum dots exhibiting significant confinement effects must be very small. But at the same time, the interest in II-VI QDs is intense because of their device potential in the short-wavelength visible range of the electromagnetic spectrum. Much of the efforts in II-VI QDs have been concentrated on the CdSe/ZnSe system partly by the fact that the CdSe/ZnSe combination is, in terms of strain relationships, identical to the now well-established InAs/GaAs QD system. Since bond configurations are identical in both systems, while their chemical properties are obviously different, comparison of InAs/GaAs and CdSe/ZnSe systems should thus provide valuable insights into the roles played by strain and by chemistry in the process of QD formation. So here I choose to study CdSe/ZnSe SAQDs as a starting point.

In section 5-2, I will report the self-assembled growth of CdSe/ZnSe and CdSe/$Zn_{0.97}Be_{0.03}Se$ QDs, the topological measurements on uncapped QDs and detailed

studies of the optical properties of these two types of capped material structures. The AFM measurements and PL measurements show that introduction of Be in the layer on which the CdSe QDs are formed results in smaller size, higher density and better uniformity of the QDs. We observe that the PL intensities at RT for these two structures are very different while they are comparable at low temperature. A TRPL study reveals that non-radiative processes dominate at RT in the CdSe/$Zn_{0.97}Be_{0.03}Se$ QDs structure while these non-radiative processes do not dominate in the CdSe/ZnSe QDs structure up to RT. We developed a method to estimate the capped CdSe/$Zn_{0.97}Be_{0.03}Se$ QDs size and composition, based on PL and photoluminescence excitation (PLE) as well as Raman scattering spectroscopy measurements. Assuming spherical QDs shape, QDs size and composition were obtained. We also performed CER measurements on the CdSe/ZnSe QDs, and observed transitions due to the QDs and the wetting layer. In this case, assuming lens shaped QDs, QDs size was extracted. Raman spectroscopy measurement for this structure suggests that Cd composition is about 44%. The temperature dependence of PL lifetime is consistent with the results of the QDs size and composition estimated by these two methods.

In section 5-3, I will present the studies of the effect of Be concentration on the size of self-assembled CdSe quantum dots grown on $Zn_{1-x}Be_xSe$. And in section 5-4, I will describe the exploratory work on the growth of CdSe/ZnCdMgSe SAQDs and give some initial results.

5-2. CdSe/ZnSe and CdSe/$Zn_{0.97}Be_{0.03}Se$ SAQDs

5-2-1. Self-Assembled Growth by MBE

The samples were grown by MBE on GaAs (001) substrates in a dual chamber Riber 2300 system described in section 2-2. A 200 nm GaAs buffer layer, 30 periods of (2 nm GaAs/2 nm AlAs) short-period superlattice and a 30 nm GaAs layer were first grown at 580°C in the III-V chamber after the deoxidation of GaAs substrate under an As flux in order to achieve a flat growth front. Then the substrate with a III-V buffer layer was transferred into the II-VI chamber in UHV. Prior to the growth of the II-VI epilayers, a Zn irradiation of the GaAs surface was performed at 170°C to avoid the formation of Ga_2As_3, which is believed to be related to the formation of stacking faults.[16] Then the substrate temperature was increased to 250°C and a 6 nm ZnSe buffer layer was grown. After this, 94 nm $Zn_{0.97}Be_{0.03}Se$ (or ZnSe) epilayers, which are nearly lattice matched to GaAs, were grown at 270°C. CdSe QDs were formed by depositing 2.5 MLs of CdSe on ZnBeSe (or ZnSe) surface at a substrate temperature of 320°C and with a growth interruption of 30 s. To ensure that the surface conditions (i. e., surface temperature) in the two experiments are the same, except for the presence of Be in the ZnBeSe layers, the Be cell was kept on (~900°C) during both growth sequences.

To determine the Be concentration in ZnBeSe layer, one calibration sample of ZnBeSe thick layer (~1.4 μm) was grown right before the QD samples' growth. Fig. 5.2 shows the (004) symmetrical reflection and the (115) *a* and *b* asymmetrical reflection DCXRD rocking curves for the ZnBeSe thick layer. A very narrow peak related to the ZnBeSe epilayer, with a FWHM of 23 arcsec, was observed, indicating a very high crystalline quality. From the (115) *a* and *b* asymmetrical reflection DCXRD we can

obtain the perpendicular and parallel lattice constant: a_1 and a_2. The bulk lattice constant then is calculated from the equation

$$a = a_1\{1-[2\nu/(1+\nu)][(a_1-a_2)/a_1]\} \quad (5\text{-}1)$$

Where ν is the Poisson's ratio. Here we use ν=0.28 (ν for ZnSe) for ZnBeSe due to small Be concentration. Assuming that Vegard's law is valid for ZnBeSe and the bulk lattice constant for ZnSe and BeSe is a_{ZnSe}=5.6676 Å and a_{BeSe}=5.139 Å, the Be concentration of 3.1% could be attained from the lattice constant.

5-2-2. AFM Measurements of Uncapped QDs

AFM measurements of CdSe QDs grown on $Zn_{0.97}Be_{0.03}Se$ and ZnSe were performed at room temperature right after the growth. A smooth surface for the $Zn_{0.97}Be_{0.03}Se$ surface without CdSe was observed with a surface roughness of about 4 nm. Fig. 5.3(a) shows a (2 μm x 2 μm) AFM image of 2.5 MLs of CdSe deposited on $Zn_{0.97}Be_{0.03}Se$ at 320°C. The average QD density is $1.5x10^9$ cm^{-2} with an average diameter of ~ 70 nm and an average height of ~ 12 nm. The three-dimensional AFM image of this sample is shown in Fig. 5.4. For comparison, an AFM image of 2.5 MLs of CdSe deposited on ZnSe at 320 °C is shown in Fig. 5.3(b). Much lower QD density and larger QD size than those grown on $Zn_{0.97}Be_{0.03}Se$ under the same growth conditions were observed on ZnSe. The average QD density is $5x10^8$ cm^{-2} with an average diameter of 105 nm and an average height of ~ 18 nm. Clearly, presence of Be in the barrier layer makes the QD size smaller and density higher. Recently, this behavior has also been observed by Keim *et al.*,[17] who demonstrated that coverage of the ZnSe starting surface with a fractional ML of BeSe (0.01-0.05 ML) leads to enhanced CdSe island formation in CdSe/ZnSe heterostructures well below the CdSe thickness of 0.6-0.7 ML.

5-2-3. Optical Studies of Capped QDs

The steady-state PL intensity profiles at 77 K and RT for the two samples investigated are shown in Fig. 5.5(a) and (b), respectively. At each temperature the measurements were made under identical instrumental conditions so the relative intensities could be compared. The slightly higher peak position and narrower linewidth of the $Zn_{0.97}Be_{0.03}Se$ -based sample are attributed to the smaller and more uniformly sized islands in this structure. Interestingly the figures show that the steady state PL intensity from the CdSe QDs on ZnSe measured at RT is much higher than that from CdSe QDs on $Zn_{0.97}Be_{0.03}Se$ while the two have similar intensities at 77 K.

To better understand the PL intensity relationship at these two temperatures, we have performed TRPL measurements on both samples as a function of temperature, in the range of 77 K to RT. The PL decay profiles at 77 K and RT for the two samples are shown in Fig. 5.6(a) and (b). (A small kink observed in the time range of about 869 ps ~ 951 ps is due to the streak camera error in this time region and the slight downward bend at the end is due to background subtraction.) While at 77 K the two decay traces nearly overlap and have comparable rate of decay, at RT the $Zn_{0.97}Be_{0.03}Se$ -based QDs sample exhibits a much faster PL decay rate than the ZnSe-based sample. In these measurements, QDs of all sizes contribute to the time decay. It has been previously shown[18] that PL lifetime data for different QD depends on the QD size, thus measurements of an ensemble of QDs lead to a distribution of lifetimes. It is also known that decay at a single wavelength for these structures is a single exponential at most of the wavelengths.[19] Thus, our observed decay (based on spectrally integrated measurements of many QDs) is expected to be a sum of such exponentials weighed by a distribution function. It has been

stated[20] that such a sum can be replaced by a stretched exponential function $I(t)=I(0)\exp(-((t-t_0)/\tau)^{\beta})$ where τ is the PL lifetime and β represents the broadening of the distribution function (or QDs size distribution in our case). Based on these considerations we used the stretched exponential decay to fit the PL lifetimes. Thus, the PL lifetimes obtained here should be treated as average or representative PL lifetimes. Shown in Fig. 5.6(c) are the temperature dependences of the PL lifetimes obtained by this analysis. The temperature dependences of the PL lifetime for the two samples are strikingly different. The PL lifetime for CdSe QDs grown on ZnSe is about 255 ps at 77 K and increases steadily all the way to about 453 ps at RT. For CdSe QDs grown on $Zn_{0.97}Be_{0.03}Se$, the PL lifetime is about 232 ps at 77 K and goes down to about 83 ps at RT. A faster PL decay rate with increased temperatures, as observed for the $Zn_{0.97}Be_{0.03}Se$ -based samples, has also been observed and reported for other low dimensional systems.[21,22] This behavior was attributed to unspecified non-radiative phenomena that become dominant at high temperatures. However we do not observe such dominant non- radiative processes even at RT in the sample of the CdSe QDs grown on ZnSe. The absence of dominant non-radiative processes at RT has important implications for light emitting devices in which RT operation is desired.

To further understand this behavior, we developed two different methods for these two QD structures to estimate the size and Cd composition of the QDs.

The PL (T=9K) from $CdSe/Zn_{0.97}Be_{0.03}Se$ (solid line) QDs is shown in Fig. 5.7(a). Such a PL is usually observed in CdSe/ZnSe QDs structures (It is actually $Cd_xZn_{1-x}Se$/ZnSe QDs due to Cd/Zn interdiffusion) and attributed to excitons localized in QDs with different x and/or size (diameter d, assuming a spherical QD).[4] To estimate the x and

d of the QDs that are responsible for such a PL, as an initial step, we calculate the PL transition energy as a function of these two parameters by solving the Schrödinger equation based on finite spherical potential well. The results (dash lines) are plotted in Fig. 5.7(a). Details of the calculation of the PL energy as a function of *x* and *d* could be found in Ref. 23. It is based on the following assumptions: (1) The QDs are considered spherical and the Coulomb energy of the excitons has been ignored. Because our TRPL results show that the PL decay time stays constant up to T=150 K, also the radiative process dominates up to this temperature range (see Fig. 5.8), indicating zero-dimensional character; (2) only the ground state of QDs is considered, since only a single PL peak is observed even at the highest excitation intensity (~28 W/cm^2) and the integrated PL intensity as a function of excitation intensity shows a single slope (not shown here); (3) the QDs are considered free of Be, since there is only 3% of Be in the barrier layer; (4) for barrier material ($Zn_{0.97}Be_{0.03}Se$) properties, we use ZnSe values except for the band gap energy (E_g), which is calculated using the relation given in Ref. 24; (5) the material parameters for $Cd_xZn_{1-x}Se$ are obtained by linear interpolation between those of pure CdSe and ZnSe except for E_g, where the quadratic dependence on *x* is used with the bowing parameter B=0.35;[25] (6) the shifts of the band edges due to the hydrostatic component of strain are calculated independently[26] assuming there is no shear component of the strain due to the spherical QDs. To determine both the *x* and the *d* of the QDs that contribute to the PL at a given wavelength, two independent measurements are necessary. The second measurement that we can use is the LO phonon energy obtained at a given wavelength using PLE. The PLE spectrum on CdSe/$Zn_{0.97}Be_{0.03}Se$ (T=9K) with detection energy ($\hbar\nu_{det}$) at 2.45 eV (indicated by the arrow) is plotted in Fig.

5.7(b) along with the PL. The PLE spectrum consists of a sharp strong peak at about 2.866 eV, which corresponds to the free exciton energy in $Zn_{0.97}Be_{0.03}Se$,[24] a rather broad band feature below this peak, which is presumably due to excitation via the CdZnSe wetting layer, and three equally-spaced peaks (indicated by A, B and C) adjacent to the detection energy, which are consistently observed at various $\hbar\nu_{det} > 2.43$ eV (not shown here). The energy separation between these peaks as well as between the detection energy and peak A is around 28 meV, which is in the range of the $Cd_xZn_{1-x}Se$ alloy LO phonon energy ($\hbar\omega_{LO}$). A more careful investigation (see the inset of Fig. 5.7(b)) of peak A reveals that it can be fitted well with two Lorentzians, whose energy separations from $\hbar\nu_{det}$ is ~ 28.7 meV (peak 1) and 24.7 meV (peak 2). Peak 1 and peak 2 are attributed to LO phonon from $Cd_xZn_{1-x}Se$ QDs with a given x and surface phonon, respectively. We then proceed to quantitatively estimate $\hbar\omega_{LO}\ (x, d)$ for $Cd_xZn_{1-x}Se$ QDs as a function of x (strain included) and QDs' d using the method developed in Refs. 27,28, assuming the linear interpolation between CdSe and ZnSe values. Combining the calculation of $Cd_xZn_{1-x}Se$ QDs PL transition energies and LO phonon energies as well as the LO phonon energy data obtained from PLE, we are now able to estimate the Cd composition and size of QDs emitting at a given wavelength (shown in the inset of Fig. 5.7(a) is an example at $\hbar\nu_{det} = 2.45$ eV) and obtain that the QDs diameter ranges from 5.1 nm to 8.0 nm with Cd composition between 47% and 54%.[29] It is interesting that the radii of QDs (2.5 nm-4.0 nm) are smaller than the exciton Bohr radius in CdSe (~ 5.4 nm[30]), suggesting a nearly 0-dimensional character.

This analysis has a limitation in that the assumed geometry of the QD (spherical) is not realistic. A more realistic picture might be to consider the dots to be spherical "cap"

(lens shape). The above analysis also requires that we observe LO-phonon lines in the PLE spectrum, which was not observed in the CdSe/ZnSe QDs structure. The absence of this line suggests[31] that the "QDs" in this structure are larger than in CdSe/ $Zn_{0.97}Be_{0.03}Se$ structure (the Cd compositions are similar for both structures, as will be shown below). Thus a different analysis was needed for the CdSe/ZnSe QDs structure.

Shown in Fig. 5.9(a) is the measured RT CER spectrum (solid line) and the fitting (dash line) for CdSe/ZnSe QDs structure. The energies corresponding to the observed transitions were obtained using a fit and indicated by arrows. The transitions originating in the SL/buffer region (< 2.2 eV) present a series of Franz-Keldysh oscillations, and were fit using Lorentzian broadened electro-optical functions.[32] The transitions originating from the QDs, wetting layer (WL) and barrier (> 2.2 eV) were fit using the first derivative of a Gaussian lineshape[32] due to their bound origin. In order to identify the transitions originating from the QDs, the shape of the quantum lens in real space has been modeled by a spherical cap of height h and circular cross section with radius r. For simplicity and in the limit of strong spatial confinement regime, we have used in our calculation the uncoupled electron-hole particle Hamiltonian model confined in the QD domain with isotropic bands and effective masses m_e and m_h for the electron and holes, respectively. There is no explicit solution for the corresponding Schrödinger equation for a quantum dot with lens-shape geometry. Taking full advantage of the results pointed in Ref. 33, the energy levels of the lens can be expressed as a function of the geometric parameters h and r. It is possible to show that the electron-hole pair energy is given by[33]

$$E_{N_e M_e; N_h M_h} = \frac{\eta^2}{2r^2}\left[\frac{\lambda_{N_e M_e}\left(h/r\right)}{m_e} + \frac{\lambda_{N_h M_h}\left(h/r\right)}{m_h}\right] \qquad (5\text{-}2)$$

where M=0, ±1,.. is the z-component of the orbital angular momentum and N enumerates the levels by increasing energy. In the above equation $\lambda_{N,M}$ are the eigenvalues of the problem which depend on the ratio h/r[33]. According to the allowed optical selection rules, $N_e=N_h$, and $M_e=M_h$, the features observed in the CdSe QD spectral region correspond to the transitions $|N,M>_e \rightarrow |N,M>_h$. Assuming that this ratio minimizes the energy surface in this system and, therefore, is the most favorable ratio for QDs formation, and using the effective masses taken from Ref. 34, we determined the that dimensions of the capped CdSe-QDs corresponding to these QD_0 and QD_1 transitions are h=3.24 nm and r=9.52 nm.[35] According to this calculation the features QD_0 and QD_1 correspond to the electron $\rightarrow$ heavy hole transitions $|1,0>_e \rightarrow |1,0>_{hh}$ and $|1,1>_e \rightarrow |1,1>_{hh}$, respectively. We should note that, the above calculation is based on the assumption that the QD is pure CdSe. Taking into considerations that there exists intermixing between Cd and Zn, the QD is actually $Cd_xZn_{1-x}Se$, the calculation should give larger QD size. This result shows that the radius of the QDs in this structure is larger than the exciton Bohr radius, suggesting a quasi-two dimensional character, consistent with the absence of the LO phonon lines in PLE as well as the temperature dependencies of PL lifetime.

The above analysis estimates the QD size only at a given Cd concentration. In order to obtain information about the Cd concentration of the CdSe/ZnSe QDs, another measurement is necessary. By the preliminary studies using polarized Raman scattering spectroscopy with the excitation of 514.5 nm which is shown in Fig 5.9(b), we obtained the LO phonon energy of the CdSe/ZnSe QDs. Following a similar procedure to that used above for the $CdSe/Zn_{0.97}Be_{0.03}Se$ QDs, calculations based on the quantum disk model suggest that the Cd concentration is about 44%..[36]

Based on the results shown above, we propose that the presence of Be in the barrier makes the QDs size smaller but doesn't affect the intermixing in the QDs. The CdSe/$Zn_{0.97}Be_{0.03}Se$ QDs are very small, exhibit nearly 0-dimensional quantum confinement, consistent with the temperature dependent TRPL results where the PL lifetime for the CdSe/$Zn_{0.97}Be_{0.03}Se$ QDs is about 232 ps at 77 K and remains nearly constant up to 150 K. Due to the small size of the QDs (low ionization energy), the PL lifetime goes down to about 83 ps at RT where the non-radiative processes dominate. In the case of CdSe/ZnSe QDs, the QDs size is large, showing a quasi-two-dimensional behavior. In this case, the temperature dependent TRPL results show the PL lifetime for CdSe QDs grown on ZnSe is about 255 ps at 77 K and increases with increasing temperature, consistent with 2-dimensional confinement. Due to the large size of the QDs (very high ionization energy), the PL lifetime increases steadily all the way to about 453 ps at RT without the effect of the non-radiative processes.

In summary, we report detailed studies of the optical properties of CdSe QDs grown on ZnSe and $Zn_{0.97}Be_{0.03}Se$ by MBE. We performed TRPL measurement and obtained PL lifetime for these two structures. We also estimated the QDs size and Cd composition using different methods. The results of PL lifetime are consistent with the results of estimation of the QDs size and composition.

5-3. Effect of Beryllium concentration on the size of self-assembled CdSe quantum dots grown on $Zn_{1-x}Be_xSe$

5-3-1. Introduction

Above, I have reported the growth and optical studies of CdSe SAQDs on ZnSe and $Zn_{0.97}Be_{0.03}Se$ by MBE. AFM measurements on uncapped QD structures of these materials as well as optical studies on capped QD structures show that the size of CdSe QDs on $Zn_{0.97}Be_{0.03}Se$ is significantly smaller than that on ZnSe.

Could we change the QD size by varying the Be concentration in the $Zn_{1-x}Be_xSe$ barrier layer? In this section I will report a study of the effect of Be concentration on the size of self-assembled CdSe QDs grown on $Zn_{1-x}Be_xSe$. Varying the Be concentration in the $Zn_{1-x}Be_xSe$ barrier layer was accomplished by changing either the Zn cell temperature or the Be cell temperature, or both. We show that higher Be concentration in the $Zn_{1-x}Be_xSe$ layer results in higher QD photoluminescence (PL) emission energy produced by a reduction on the QD size. The smaller size was also observed on uncapped QDs by AFM measurements. We also used contactless electroreflectance (CER) and surface photovoltage spectroscopy (SPS) to characterize the capped QDs. Our experiments indicate a strong dependence of the QD size on other unintentionally varying growth parameters that must be carefully controlled in order to use the Be effect to control QD size for practical applications.

CER measures the changes in the optical reflectance of the material with respect to a modulating electric field, giving rise to sharp, derivative-like spectra in the region of the transitions. CER utilizes a condenser-like system consisting of a front wire grid electrode with a second metal electrode separated from the first electrode by insulating spacers, which are ~0.1 mm larger than the sample dimension. We placed the sample between these two capacitor plates. Thus, there is nothing in direct contact with the front surface of the sample. The probe beam is incident through the front wire grid.

Electromodulation is achieved by applying an ac voltage of 1.2kV, 200 Hz across the electrodes. In the SPS technique, the contact potential difference between the sample and a reference grid electrode is measured in a capacitive manner as a function of the photon energy of the probe beam. This was accomplished by holding the grid fixed and chopping the probe beam. We used the same grid-back metal plate configuration as CER except that the incident probe radiation is chopped; and there was no applied high voltage between the grid-back plate but rather the surface photovoltage (SPV) is introduced directly into the lock-in amplifier.

5-3-2. Detailed Studies

The samples were grown by MBE on GaAs (001) substrates in a dual chamber Riber 2300 system described in section 2-2. A 200 nm GaAs buffer layer was first grown at 580°C in the III-V chamber after the deoxidation of GaAs substrate under an As flux. Then the substrate with a III-V buffer layer was transferred into the II-VI chamber in UHV. Prior to the growth of the II-VI epilayers, a Be-Zn coirradiation of the GaAs surface was performed at 170°C to get $Zn_{1-x}Be_xSe$ with better quality[37] and to avoid the formation of Ga_2As_3, which is believed to be related to the formation of stacking faults[16]. Then the substrate temperature was increased to 250°C and a ZnSe buffer layer was grown for 5 minutes. After this, $Zn_{1-x}Be_xSe$ epilayers grown by 10 minutes, which are nearly pseudomorphic to GaAs, were grown at 270°C. CdSe QDs were formed by depositing 2.5 MLs of CdSe on $Zn_{1-x}Be_xSe$ surface at a substrate temperature of 320°C and with a growth interruption of 30 s. For PL measurement, a $Zn_{1-x}Be_xSe$ top barrier was

grown by 10 minutes to confine the carriers in the QDs. All the samples were grown with the same Se and Cd cell temperatures.

Shown in Fig. 5.10 is the PL peak energy at 77 K for QD structures with different Be concentration in the $Zn_{1-x}Be_xSe$ barrier layer obtained by varying the Be cell temperature while keeping the Zn cell temperature constant at 190°C. The PL peak energy was blue shifted by about 80 meV when the Be cell temperature increased from 950°C to 1010°C, indicating smaller QD size with increasing Be concentration in the barrier layer. The estimated Be concentration based on X-ray diffraction measurements on reference samples for these two Be cell temperatures are 2.0% and 5.0%, respectively. The presence of some scatter in the data are believed to be partly due to the fact that these samples were grown using manual control of the shutters. Figure 5.11 shows the PL peak energy at 77 K for QD structures with different Be concentration in the $Zn_{1-x}Be_xSe$ barrier layer obtained by changing the Zn cell temperature while keeping the Be cell temperature constant at 950°C. In these, the growth of the QD structures is computer controlled to avoid unintentional variations of the deposition time of the QDs. The X-ray diffraction measurements on reference samples give Be concentration obtained with these two Zn cell temperatures to be 2.0% and 5.3%, respectively. Two sets of Mo-blocks were used in these experiments. One set had been used for a prolonged period of time and had been subjected to repeated etching and cleaning steps. The other set was newer and had been subjected to the etching and cleaning process only a few times. The triangles and the squares represent the QD structures grown with the "new" and "used" Mo-blocks, respectively. Full lines are used to connect the results of QD structures grown on the same day, and are a guide for the eye. Clearly all the sets of samples in which only one

type of Mo-blocks was used exhibit a similar trend, with similar slope, although there is a large variation in the absolute value of the emission between samples grown on different days. A blue shift of the PL peak energy of about 90 meV was observed in all the sets of samples when the Zn cell temperature decreased from 190°C to 160°C, indicating smaller QD size with increasing Be concentration in the $Zn_{1-x}Be_xSe$ barrier layer. One set of samples was grown using the two types of Mo-blocks. The results of the two QD structures represented by open squares and the two represented by open triangles were all grown on the same day but with the two sets of Mo-blocks. This set is connected with a dashed line. A large discontinuity between the samples grown with the "used" blocks and those grown with the "new" blocks is seen, suggesting an unintentional change of the growth conditions as a result of the different blocks. We suggest that the substrate temperature may change when different Mo-blocks are used, which is causing a change in the QD size that results in variation of the PL peak energy. Variations in substrate temperature depending on the Mo-block are a common problem in MBE growth. We also attribute the apparently random variation of the emission energy between samples grown on different days to unintentional variations in growth conditions from one day to another that also affect the QD size.

In order to better characterize this phenomenon we have performed room temperature (RT) CER and SPS measurements on some samples. The solid lines in Fig. 5.12 are the 77 K PL spectrum (a), amplified (10X) RT measured CER spectrum (b), RT measured CER spectrum (c) and the first derivative of the SPV (DSPV) spectrum (d) for the sample with 77 K PL peak energy of 2.553 eV ([Be]~ 5.3%) shown in Fig. 5.11. For spectra b and c, the dash-dot lines are the fitting obtained by using the first derivative of a

Gaussian lineshape[32] due to their bound origin. Four peaks at 2.529 eV, 2.7098 eV, 2.8157 eV, and 2.9479 eV were obtained and attributed to the emission from QDs, ZnSe, $Zn_{0.952}Be_{0.048}Se$, and the excitonic transition E_1-R_1 of GaAs, respectively. The identification of these peaks was done by comparison with the PL emission (2.553 eV at 77 K), and considering the reported values for E_0(ZnSe)=2.700 eV[38] , E_0(BeSe)=5.1 eV[39] and E_1-R_1 (GaAs)=2.97eV.[40] Comparing the two peaks (2.50 eV and 2.816 eV) in the DSPV spectrum (d) with those in the CER spectrum, it is clear that they correspond to the signals from the QDs and the $Zn_{1-x}Be_xSe$, respectively. In fact, a strong, well-defined signal from the QD could be seen. Thus, the peaks in DSPV spectrum are very useful to identify the emissions from the QDs and the corresponding $Zn_{1-x}Be_xSe$ barrier layer simultaneously. Shown in Fig. 5.13 is the measured RT DSPV spectra for the four samples represented by the open symbols in Fig. 5.11. The spectra (from top to bottom) correspond to the open symbols (from left to right). The top two spectra correspond to those grown with the "new" blocks, meanwhile the bottom two ones to the "used" blocks. Fig. 5.13 indicates that the change in the band gap of the barriers of the structures grown on the "new" blocks (top two spectra) due to the increased Be content is 8 meV, while the quantum dot transition is blue-shifted by 52 meV. Numerical calculations[41] indicate that an increase in the band gap barrier by 8 meV will shift the QD energy transition only by 5 meV. Similarly, for the samples grown on the "used" blocks (bottom ones) an increase in the band gap energy of the barrier by 44meV corresponds to a blue-shift of 12 meV in the QD transition if the same size is assumed, however the observed shift is 30 meV. This indicates that the main contribution to this shift is the QD size reduction. It follows that effect of the Be incorporation is not only the increase of the barrier energy but also the

formation of smaller QDs. The data on Figure 5.13 also show that the discontinuity in the emission energy of the four samples shown in open symbols in Figure 5.11 is not due to lack of control of the Be content in the samples, which is seen to vary monotonically as expected, but rather is due to another unintentional variation in the growth parameters that affects the size of the QDs. As previously stated, we suggest that substrate temperature may be the unintentional variable introduced by changing the blocks.

To enhance the effect of Be concentration, we designed an experiment with a much larger change in Be concentration of the barrier layer. This was done by growing two samples using the two "new" blocks, on the same day, with two sets of cell temperatures: 1) T(Zn)=190°C, T(Be)=950°C and 2) T(Zn)=160°C, T(Be)=1010°C. The Be concentration measured by X-ray rocking curves on reference samples is about 2.0% and 24%, respectively. Given in Fig. 5.14 is the PL emission at 77 K for these two structures. The PL peak energy for the sample with $Zn_{0.76}Be_{0.24}Se$ barrier layer is about 233 meV higher than the one with $Zn_{0.98}Be_{0.02}Se$ barrier layer. The PL linewidth for the QD structure with higher Be concentration is slightly broader. Also a weak deep level emission at ~ 2.30 eV is observed in this sample. Two other structures with uncapped QDs were also grown under the same conditions. The AFM measurements on these two uncapped structures are shown in Fig. 5.15. The AFM scans clearly indicate that the QDs are much smaller in the case of the higher Be concentration sample. Profile measurements of the AFM scan show that the height of the QD for the structures with $Zn_{0.98}Be_{0.02}Se$ and $Zn_{0.76}Be_{0.24}Se$ barrier layers, are about 20.0 nm and 3.9 nm, respectively. The AFM images also clearly indicate a large reduction in the QD diameter. The smaller dot size is consistent with the PL blue shift observed in the capped samples.

A rougher surface for the $Zn_{0.76}Be_{0.24}Se$ sample compared to the $Zn_{0.98}Be_{0.02}Se$ sample is clearly evident in the AFM scans. We attribute the broader PL linewidth for the capped sample with higher Be concentration in the barrier to the enhanced wave function overlap between the QD and the barrier layer for smaller QDs, combined with the increased surface roughness in the $Zn_{0.76}Be_{0.24}Se$ barrier layer. The reduced crystalline quality of the barrier layer is also evident from the weak deep level emission observed in the PL.

Our results demonstrate that the increased Be concentrations in the barrier layer result in smaller QDs. In this study, the size reduction of the QDs is not expected to be due to an increase in lattice mismatch, since the $Zn_{1-x}Be_xSe$ layers are very thin and nearly pseudomorphic so that the in plane lattice constant is the same as that of GaAs substrate. We believe that the observed size reduction by the presence of Be is due to differences in the surface energy and/or the chemical properties of the $Zn_{1-x}Be_xSe$ surface due to the presence of Be. Chemical effects on the QD size have been involved in other systems such as CdSe/ZnCdMgSe[42] and CdSe/ZnMnSe.[43]

In summary, the effect of Be on the formation of the CdSe QDs grown on $Zn_{1-x}Be_xSe$ has been studied. The reduction of the QD size by increasing the Be concentration in the $Zn_{1-x}Be_xSe$ barrier layer has been demonstrated under controlled growth conditions. The results also indicate a very high sensitivity of the QD size to other growth parameters, sometimes difficult to control, such as possibly variation in the substrate temperature. Very careful control of the conditions during growth is essential in order to take advantage of the Be concentration effect on SAQD size in practical applications.

5-4. CdSe/ZnCdMgSe SAQDs

During the past several years, our group has performed research in the ZnCdMgSe system and have gained much knowledge about this system, including the growth of ZnCdMgSe epilayers with good quality[44], the photoluminescence properties of ZnCdMgSe epilayers[45], device structures such as LEDs[46] and photo-pumped lasers[47,48] based on the quantum well structures with ZnCdMgSe as barrier layer and ZnCdSe or ZnCdMgSe as the quantum well layer. In order to take advantage of this well-established system, and to apply the knowledge gained on the above studies about CdSe/Zn(Be)Se QDs, we have begun to explore the growth of CdSe QDs on ZnCdMgSe layers lattice matched to InP. This quaternary material can be grown with a bandgap similar to that of Zn(Be)Se and has approximately half of the lattice-mismatch of the CdSe/Zn(Be)Se system.

For the comparison, and to use the knowledge we have gained about the CdSe/Zn(Be)Se QDs, we started with ZnCdMgSe of Eg~ 2.8 eV (similar to that of Zn(Be)Se) nearly lattice-matched to the InP substrate.) For the QDs, we used the same growth conditions as for CdSe/Zn(Be)Se in terms of substrate temperature (320°C) at which CdSe was deposited as well as interruption time (30"). Since the lattice-mismatch between CdSe and ZnCdMgSe is nearly half of that between CdSe and Zn(Be)Se, we assumed that the critical thickness now should be about double of that of CdSe/Zn(Be)Se, so we chose the deposition time of QDs at 26". Considering the variation of the deposition time of CdSe due to the possible variations of the flux, we also tried the deposition time of CdSe at 22" and 30". For completeness, we also tried the deposition time of 13", which is the same time we used for the formation of CdSe/Zn(Be)Se QDs.

Initially we grew four samples with CdSe deposition times of 13" (A1992), 26"(A1993), 22"(A1994) and 30"(A1995). The sample structure and growth details are as the follows: InGaAs buffer layer was first grown, then 1 minute of interfacial layer of ZnCdSe was grown at 170°C in order to improve the interface to get ZnCdMgSe with better quality[49], followed by ZnCdMgSe of Eg~2.8 eV grown initially at 250°C for 1 minute then increased to 270°C by 9 minutes without stopping the growth, then CdSe deposited for different time at 320°C, ZnCdMgSe of Eg~2.8 eV grown at 270°C by 10 minutes, and finally 1 minutes of ZnCdSe cap layer to protect the top ZnCdMgSe layer from oxidation. Shown in Fig. 5.16(a-d) is the PL emission for sample A1992, A1993, A1994, and A1995 respectively. There were two points to note. One is that there was always a strong peak around 2.0 eV for all the samples. The other is that in some samples there was one peak with lower energy beside the peak at about 2.8 eV that we believed to be from the ZnCdMgSe barrier layer. We attributed this second-high energy peak to composition fluctuations of the ZnCdMgSe. At first we assumed the peak at 2.0 eV to be the one originating from the QDs (which we expected to be relatively large) and attempted to increase the substrate temperature for the CdSe deposition. The reason for this was that in our previous CdSe/Zn(Be)Se QDs experiences, high quality QDs structures did not exhibit any emission from the barrier, and our structures were dominated by the barrier emission. Thus, we thought higher substrate temperature may enhance the QD formation and would produce higher quality QD structures. However, the result was that, although the peak intensity at 2.0 eV increased, the quality of the material degraded. This was especially evident in AFM scans of uncapped QD structures grown with these conditions.

Several observations made us doubt our original assignment. The main one was that the 2.0 eV peak was invariable in energy regardless of the deposition time, or growth temperature, leading us to suspect that this maybe was a defect level. We then performed an experiment in which we grew only the quaternary layers without the QDs, but subjecting it to the same growth interruption, and temperature cycles that the QD structures underwent. The PL emission from this sample showed also a strong peak at 2.0 eV, clearly showing that the 2.0 eV peak was actually a defect deep level and not the QD emission.

We then shifted our attention to the lower energy peak near the 2.8 eV peak and explored the possibility that it was the QD emission. We grew three samples with different deposition times of 6" (A2005), 10" (A2006), and 13" (A2007) with the CdSe deposited at 270°C, the same temperature used to grow the quaternary layer. The structures were the same as described above except that we grew thicker bottom ZnCdMgSe layer (30 minutes) to improve the sample quality. The PL emission from these three samples is shown in Fig. 5.17(a-c). There was only one narrow peak for each sample and the peak position was below that of ZnCdMgSe barrier (2.8 eV) and was shifting in energy for the different deposition times. No barrier or deep level emission was observed. We now could confidently attribute this peak to the QDs emission. AFM measurement on uncapped samples grown under these new conditions also exhibited QDs. The three-dimensional AFM image ofthe uncapped sample with deposition time of 10 secs is shown in Fig. 5.18. One interesting observation is that the PL emission changes from blue to green by simply changing the deposition time of CdSe from 6 secs (A2005)

to 13 secs (A2007). By increasing the deposition time to 36 secs, a further red shift was observed in the QD emission at 1.963 eV to the red range of the visible spectrum.

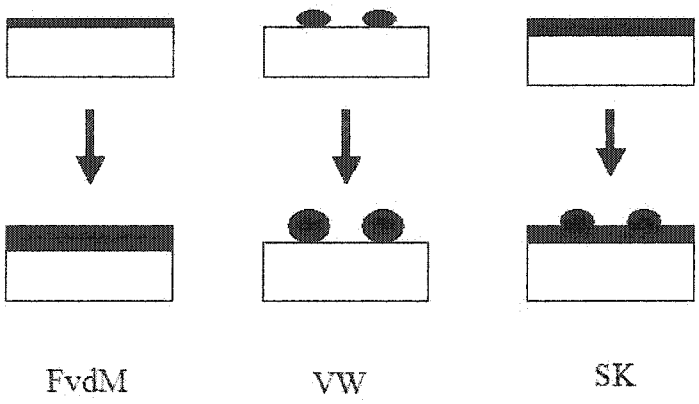

Fig. 5.1 Schematic diagrams of the three possible growth modes: Frank-van der Merwe (FvdM), Volmer-Weber (VW), and Stranski-Krastanow (SK).

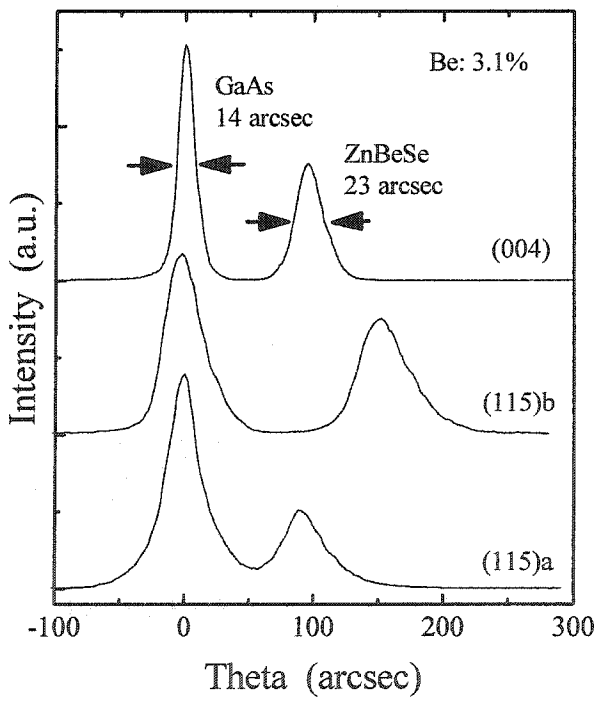

Fig 5.2 (004) symmetrical reflection and (115) *a* and *b* asymmetrical reflection DCXRD rocking curves for a ZnBeSe epilayer grown right before the QD samples' growth.

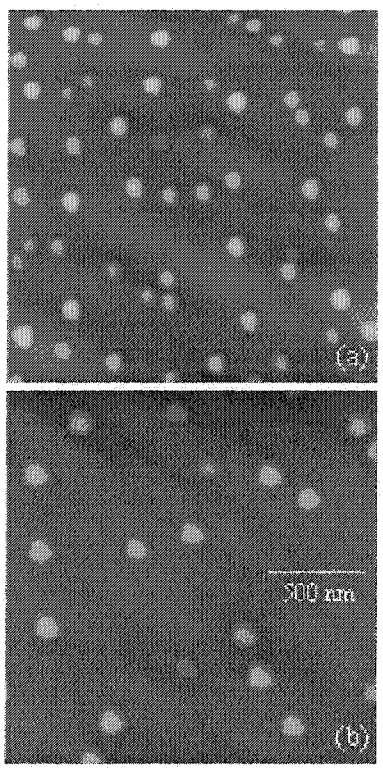

Fig. 5.3 AFM images of 2.5 MLs of CdSe depositied on $Zn_{0.97}Be_{0.03}Se$ (a) and on ZnSe (b) at 320°C (2 μm x 2 μm).

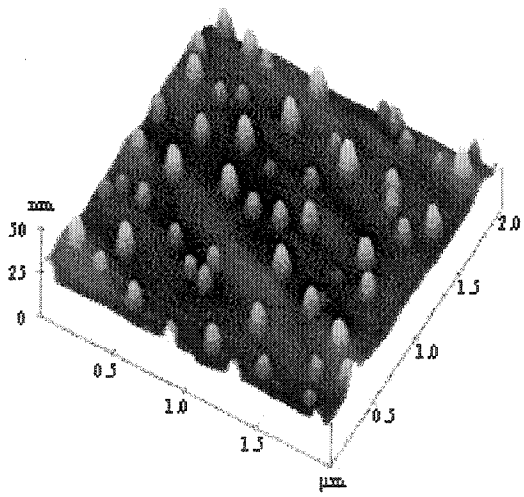

Fig. 5.4 Three-dimensional AFM images of 2.5 MLs of CdSe deposited on $Zn_{0.97}Be_{0.03}Se$ at 320°C (2 μm x 2 μm).

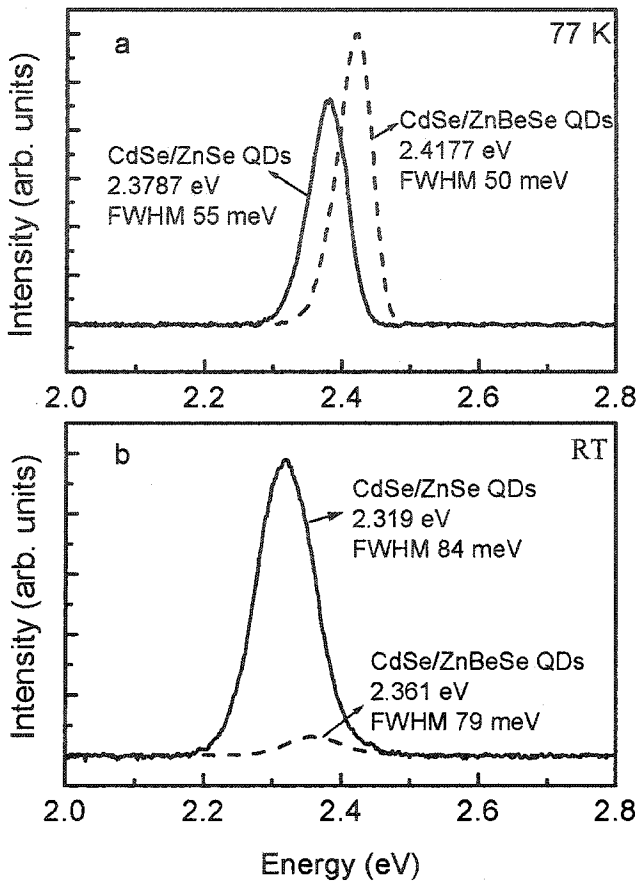

Fig. 5.5 Steady state PL intensity profiles at 77 K (a) and RT (b) for CdSe QDs grown on ZnSe (solid) and on $Zn_{0.97}Be_{0.03}Se$ (dash).

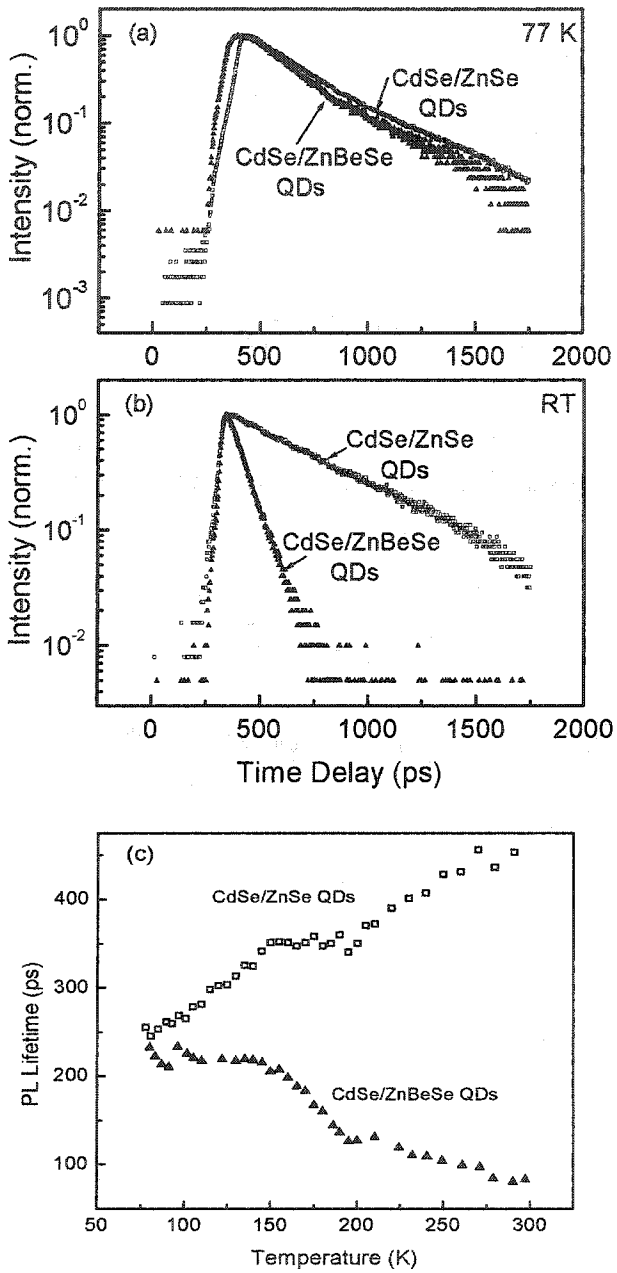

Fig. 5.6 Time-resolved PL at 77 K (a) and RT (b) for CdSe QDs grown on ZnSe (open squares) and on $Zn_{0.97}Be_{0.03}Se$ (solid triangles); (c) Temperature dependences of PL decay time for CdSe QDs grown on ZnSe (open squares) and on $Zn_{0.97}Be_{0.03}Se$ (solid triangles).

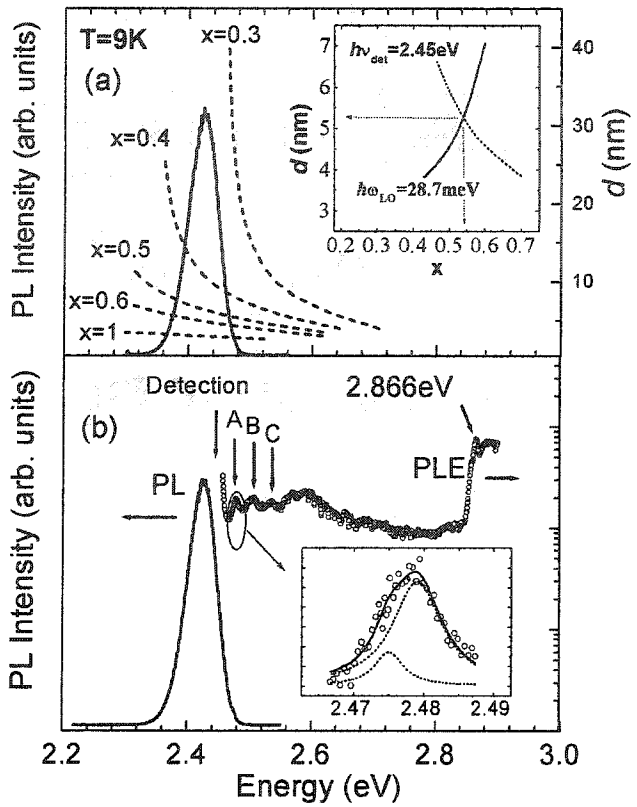

Fig. 5.7 (a) The calculated PL emission energies (dashed lines) for $Cd_xZn_{1-x}Se/Zn_{0.97}Be_{0.03}Se$ QDs as a function of x and d. The PL spectrum (T=9K) is also shown. The inset shows an example for estimation of x and d; (b) The PL (solid line) and PLE spectra (open circles, plotted in a semi-log scale) for the $CdSe/Zn_{0.97}Be_{0.03}Se$ QD sample at T=9K. The detection energy and three equally spaced peaks (A, B and C) are indicated by arrows. The inset is the magnification of the marked region in the PLE spectrum: open circles represent the experimental data, and the solid line is the result of the fitting with two Lorentzians (dashed lines).

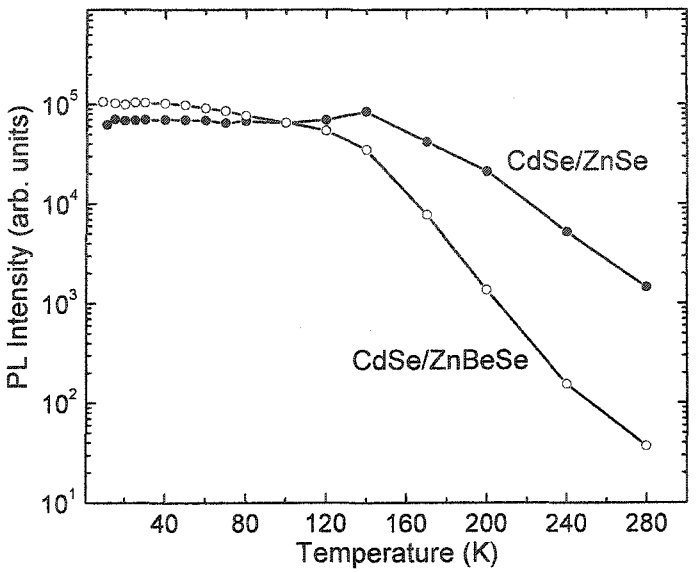

Fig. 5.8 Integrated PL intensity as a function of temperature for CdSe QDs grown on ZnSe (solid circles) and $Zn_{0.97}Be_{0.03}Se$ (open circles).

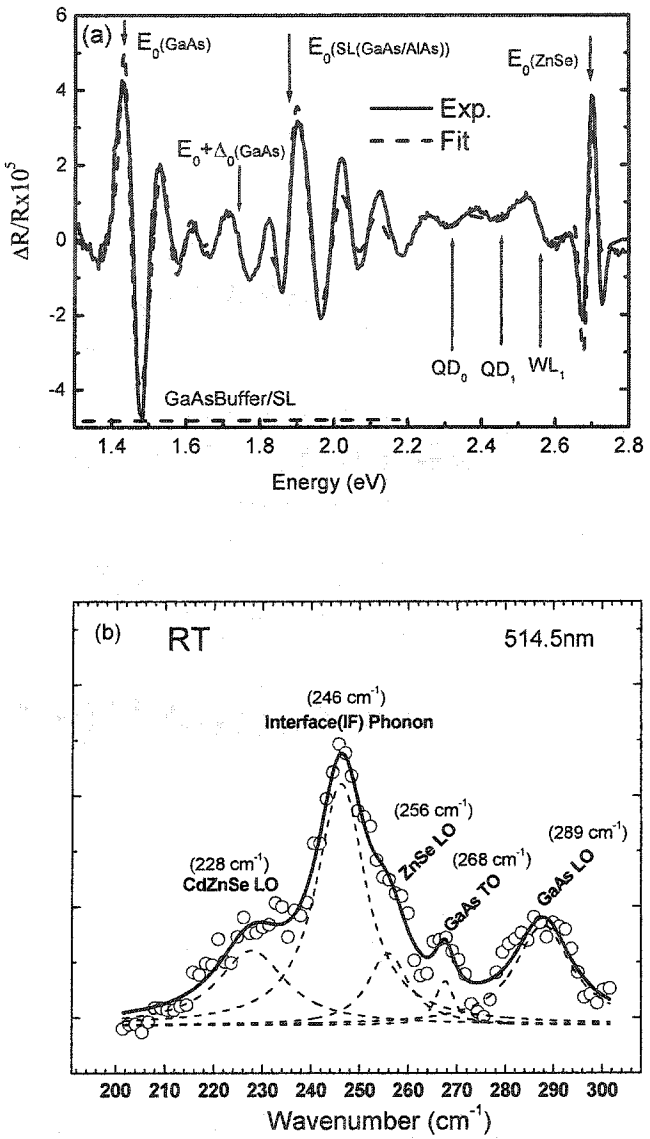

Fig. 5.9 (a) CER spectrum at RT for CdSe/ZnSe QDs structure, where solid line represents the experimental data and the dashed line is the fit. The transitions are indicated by the arrows. (b). Polarized Raman scattering spectroscopy for CdSe/ZnSe QDs structure with the 514 nm line of an Ar^+ laser as excitation source: open circles represent experimental data, solid line is the guide for the eye and dash lines are the results of fitting.

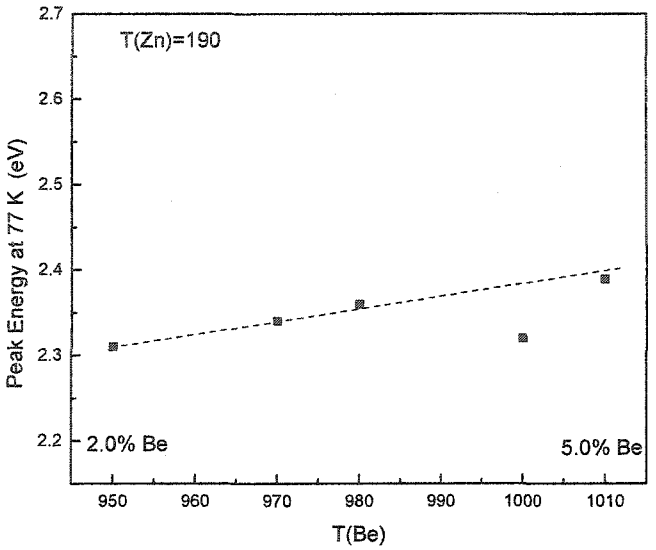

Fig. 5.10 PL emission at 77 K for the CdSe QD structures on $Zn_{1-x}Be_xSe$ with different Be concentration obtained by changing the Be cell temperature while keeping the Zn cell temperature constant. The dashed line is drawn to aid the eye.

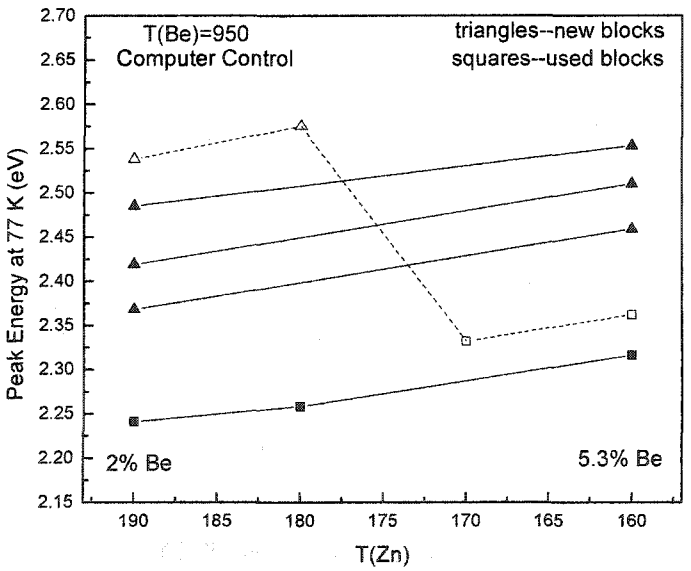

Fig. 5.11 PL emission at 77 K for the CdSe QD structures on $Zn_{1-x}Be_xSe$ with different Be concentration obtained by changing the Zn cell temperature while keeping the Be cell temperature constant. The triangles and the squares represent the QD structures grown on "new" and "used" Mo-blocks, respectively. The lines are connect of the QD structures having different Be concentration in the barrier layer grown on the same day and are a guide for the eye. The two QD structures represented by the open triangles and the two by the open squares were grown on the same day with the two sets of blocks.

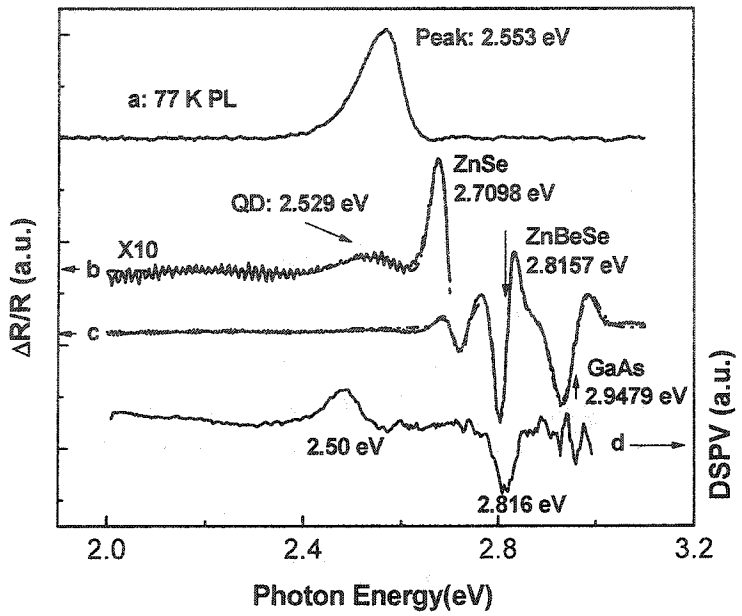

Fig. 5.12 77 K PL spectrum (a), amplified (10X) RT measured CER spectrum (b), RT measured CER spectrum (c) and the first derivative of the SPV spectrum (d) for the sample with 77 K PL peak energy of 2.553 eV ([Be]~ 5.3%) shown in Fig. 5.11. The dash-dot lines in (b) and (c) are fitting results.

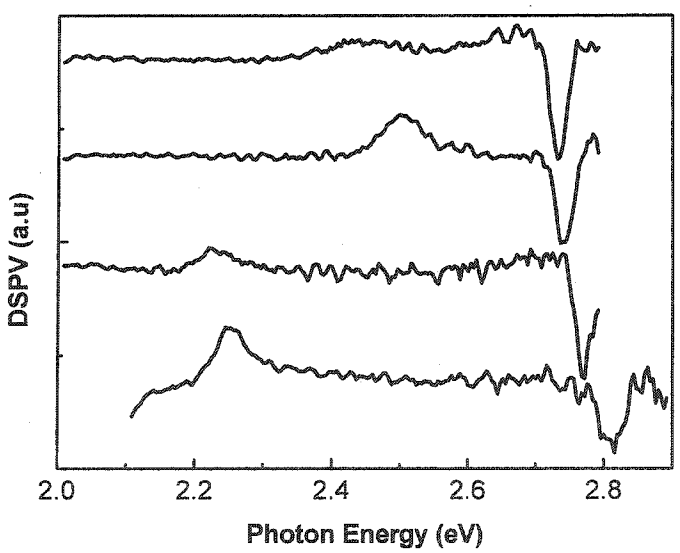

Fig. 5.13 First derivative of the RT SPV spectra for the four samples represented by the open symbols in Fig. 5.11.

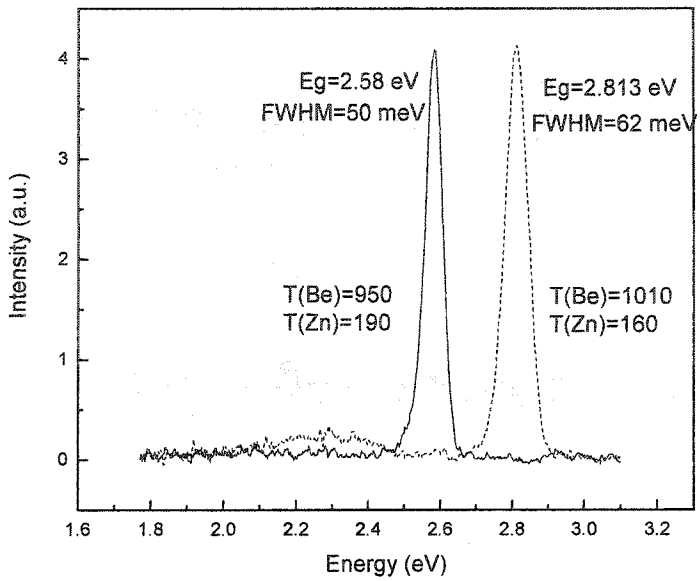

Fig. 5.14 PL emission at 77 K for the two CdSe QD structures on $Zn_{1-x}Be_xSe$ with two different Be concentrations (2%: solid line and 24%: dotted line) in the barrier layer obtained by the combination of changing the Zn and Be cell temperatures simultaneously.

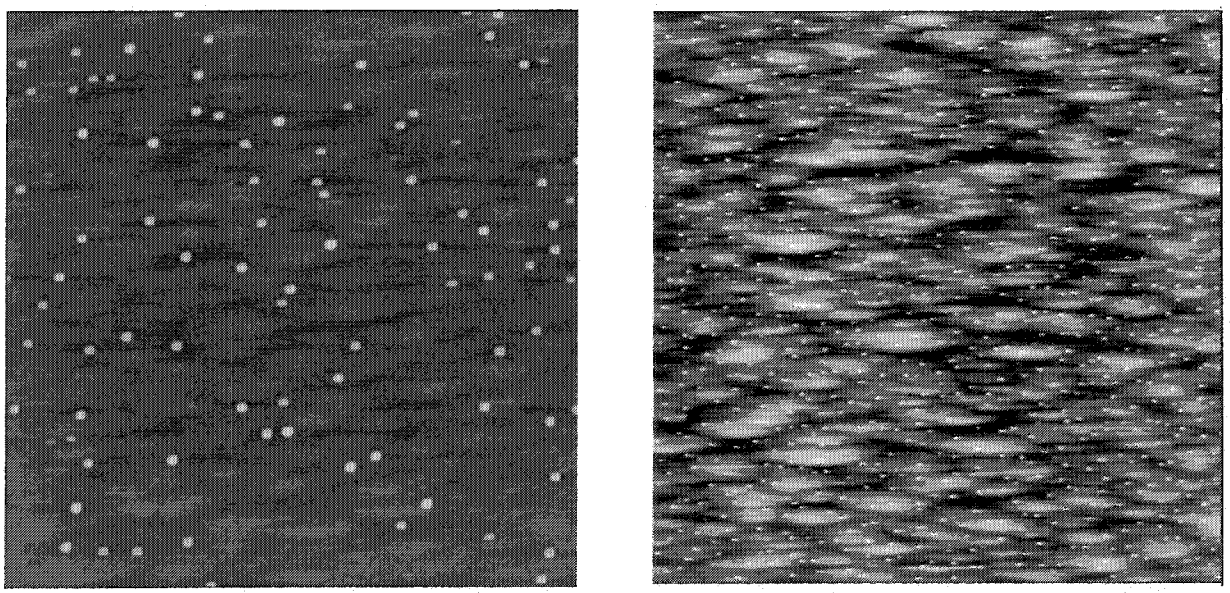

(10μm x 10μm)
(a)

(10μm x 10μm)
(b)

Fig. 5.15 Atomic force microscopy measurements (contact mode) for the two uncapped CdSe QD structures on $Zn_{1-x}Be_xSe$ with significantly different Be concentrations in the barrier layer a) with 2% Be and b) with 24% Be. The large-scale modulation seen in the background of b) is due to the greater roughness on the surface of the $Zn_{0.76}Be_{0.24}Se$ layer.

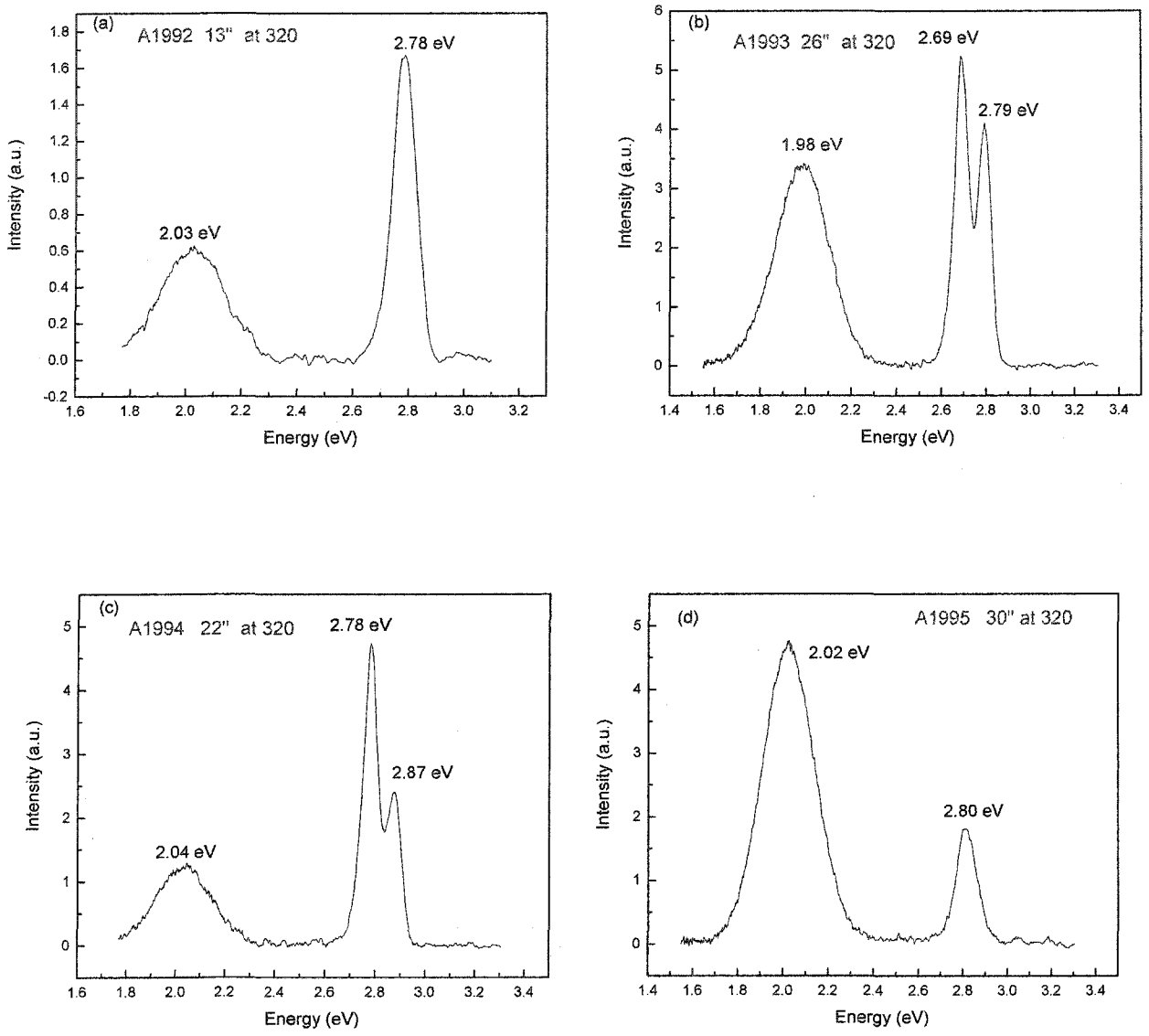

Fig.5.16 PL spectra for samples with different deposition time of CdSe deposited at 320°C

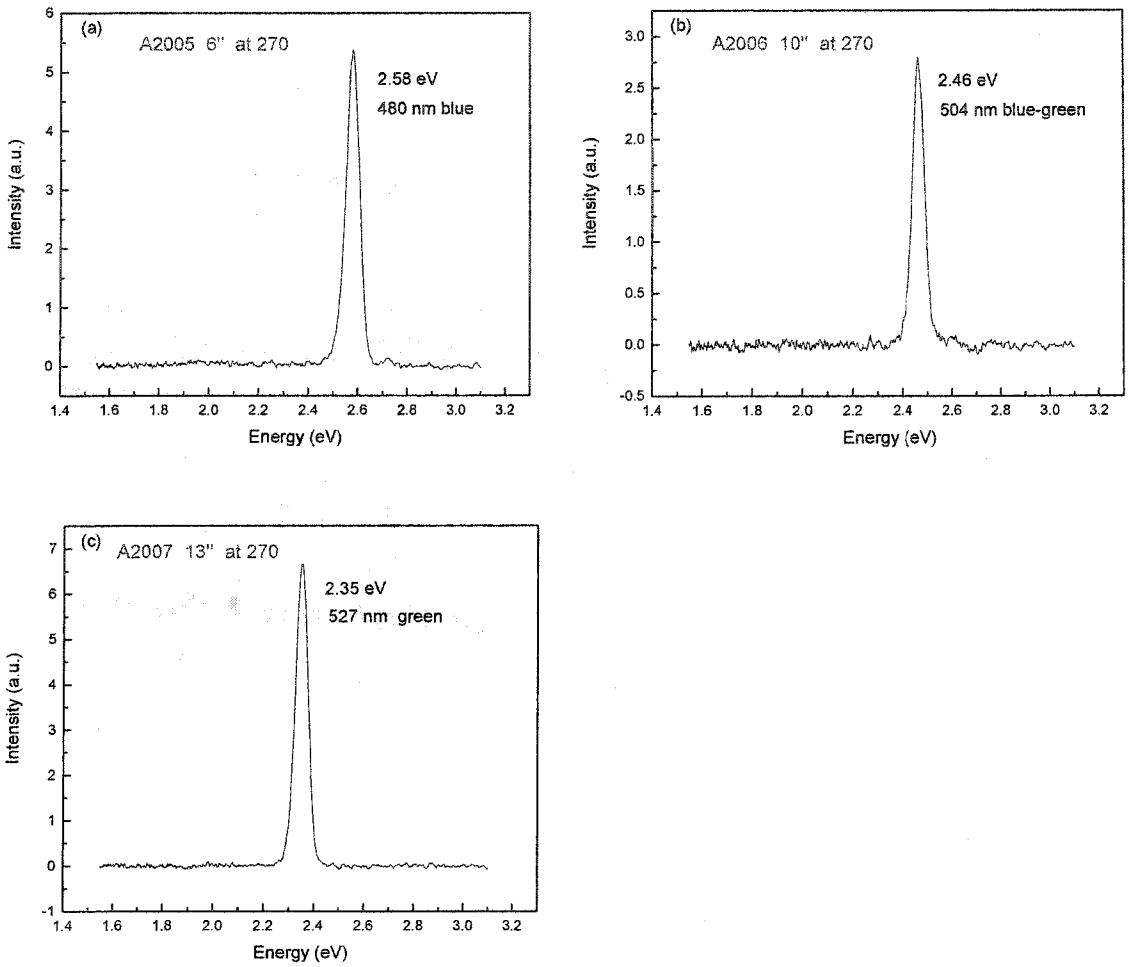

Fig. 5.17 PL spectra for the samples with different deposition time of CdSe deposited at 270°C

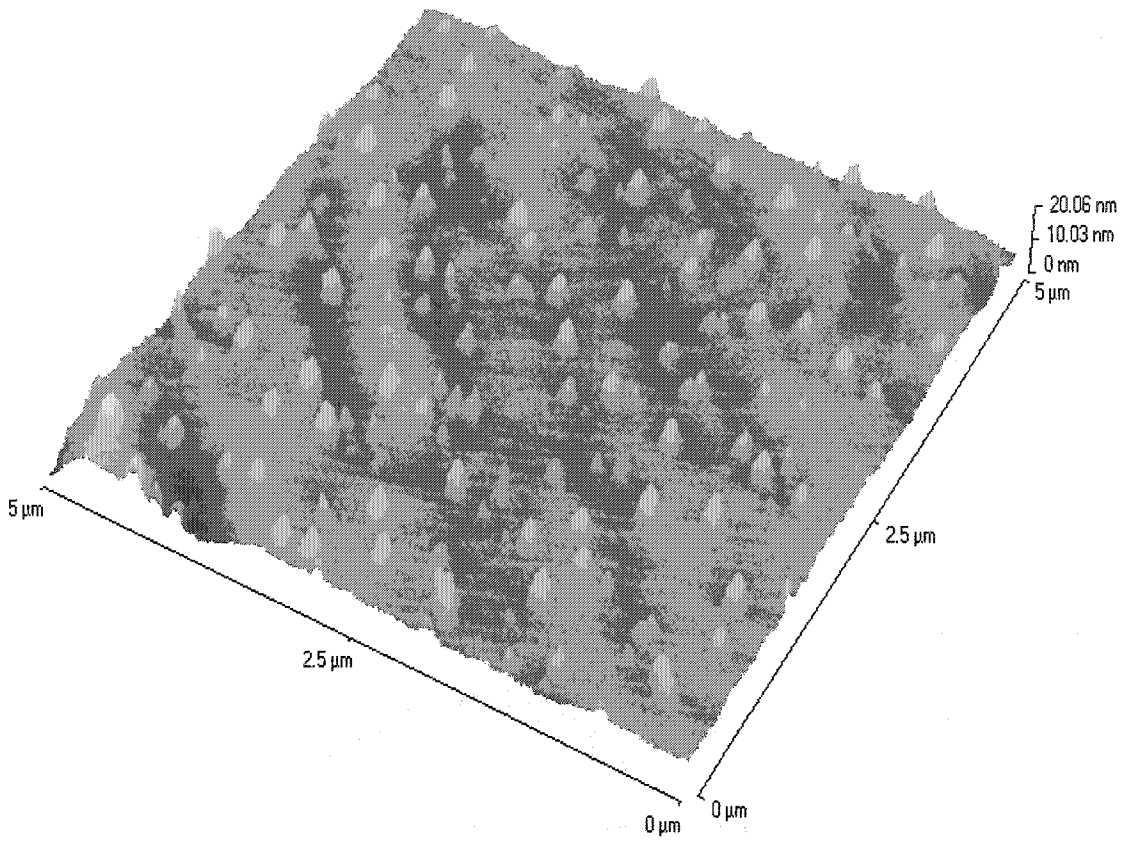

Fig. 5.18 Three dimensional AFM image of CdSe QDs grown on ZnCdMgSe of Eg~2.8 eV nearly lattice-matched to InP

Chapter 6

Summary and Suggested Future Works

6-1. Summary

The main purpose of my research is to grow low-dimensional structures and study their optical properties in order to understand the behavior of the current state of the art blue and green QW lasers based on II-VI materials, and to explore ways to improve them. Following is the summary of my work and the important outcomes.

6-1-1. $Zn_xCd_yMg_{1-x-y}Se$ alloys

(1). We have grown $Zn_xCd_yMg_{1-x-y}Se$ alloys with different Mg concentration nearly lattice-matched to InP substrate.

(2). The optical properties of $Zn_xCd_yMg_{1-x-y}Se$ alloys using PL and PLE are systematically studied. It is shown that, at low temperatures, PL is dominated by excitons localized by potential fluctuations, which becomes stronger with increasing Mg composition. Such potential fluctuations are discussed in terms of a large valence band offset in Zn(Cd)Se/MgSe systems, which serves as a manifestation of the breakdown of "Common-anion Rule".

6-1-2. Optically-pumped Blue and Green $Zn_{x'}Cd_{y'}Mg_{1-x'-y'}Se$ /$Zn_xCd_yMg_{1-x-y}$ Single Quantum Well Lasers Grown on InP

(1). We have grown $Zn_{x'}Cd_{y'}Mg_{1-x'-y'}Se/Zn_xCd_yMg_{1-x-y}$ single QW blue and green lasers lattice matched to InP with relatively thick quaternary $Zn_xCd_yMg_{1-x-y}Se$ QWs (~50

Å). The only difference for these two laser structures is the QW composition. High qualities are confirmed by the PL and DCXRD measurements.

(2). Optical confinement factors are calculated for both laser structures.

(3). We have achieved optically-pumped blue lasing at 492 nm and green lasing at 514 nm at room temperature from these two laser structures.

(4). Comparison of the threshold pumping intensity and characteristic temperature (T_0) for the blue and green lasers shows a lower threshold pumping intensity and higher T_0 for the green laser. These results are explained on the basis of the difference in carrier confinement between these two structures. For the blue laser, the temperature dependency of the threshold pumping intensity can be fitted by a simple Arrhenius behavior $I_{th}(T)=C*exp(-E_a/kT)$ with an activation energy E_a very close to the band gap energy difference between the cladding layer and the QW which points to a carrier loss process through thermalization into the cladding layer and subsequent diffusion away from the QW.

6-1-3. CdSe SAQDs on ZnSe and $Zn_{0.97}Be_{0.03}Se$

(1). We have grown CdSe/ZnSe and CdSe/$Zn_{0.97}Be_{0.03}Se$ QDs on GaAs (001) substrate by MBE.

(2). We have performed AFM on the uncapped QDs and it shows that the presence of Be in the barrier layer makes the QD size smaller and density higher.

(3). Steady-state PL measurements show that the PL intensity at RT from the CdSe QDs on ZnSe is much higher than that from CdSe QDs on $Zn_{0.97}Be_{0.03}Se$ while the two have similar intensities at 77 K.

(4). A TRPL study reveals that non-radiative processes dominate at RT in the CdSe/$Zn_{0.97}Be_{0.03}Se$ QDs structure while these non-radiative processes do not dominate in the CdSe/ZnSe QDs structure up to RT.

(5). We developed a method to estimate the capped CdSe/$Zn_{0.97}Be_{0.03}Se$ QDs size and composition, based on PL and PLE as well as Raman scattering spectroscopy measurements. Assuming spherical QDs shape, QDs size and composition were obtained. We also performed CER measurements on the CdSe/ZnSe QDs, and observed transitions due to the QDs and the wetting layer. In this case, assuming lens shaped QDs, QDs size was extracted. Raman spectroscopy measurement for this structure suggests that Cd composition is about 44%. The temperature dependence of PL lifetime is consistent with the results of the QDs size and composition estimated by these two methods.

6-1-4. CdSe SAQDs on $Zn_{1-x}Be_xSe$

(1). We have grown CdSe SAQDs on $Zn_{1-x}Be_xSe$ with different Be concentration (x).

(2). Systematic decrease of the QD size by increasing the Be concentration (x) in the $Zn_{1-x}Be_xSe$ barrier layer has been demonstrated. A 233 meV blue shift in the PL emission energy was obtained by changing the Be concentration of the barrier layer from x=0.02 to x=0.24. A corresponding decrease in the size of uncapped QDs was observed.

(3). Furthermore, a significant effect of unintentional variation in growth parameters on the size of the QDs was also evident, so that very careful control of the growth conditions is essential in order to utilize this phenomenon for practical applications.

6-1-5. CdSe SAQDs on ZnCdMgSe

(1). The initial experiments to establish the growth of CdSe/ZnCdMgSe SAQDs have been presented.

(2). High quality SAQDs of these materials were obtained.

(3). Emission throughout the whole visible range from blue to red has been obtained by simply changing the deposition time of CdSe, and initial results have been given.

In conclusion, we have successfully grown low-dimensional structures by MBE and investigated their optical properties. To do this we first investigated the optical properties of $Zn_xCd_yMg_{1-x-y}Se$ thin layers with different Mg concentrations, then $Zn_{x'}Cd_{y'}Mg_{1-x'-y'}Se/Zn_xCd_yMg_{1-x-y}$ single quantum well blue and green lasers lattice matched to InP with relatively thick quaternary $Zn_xCd_yMg_{1-x-y}Se$ QWs, and CdSe SAQDs on ZnSe and $Zn_{0.97}Be_{0.03}Se$. Detailed optical property investigations have been performed for all these structures. We also systematically studied the effect of Be concentration on the size of CdSe SAQDs grown on $Zn_{1-x}Be_xSe$. CdSe/ZnCdMgSe SAQDs has also been successfully grown with promising potential to improve the performance of $Zn_xCd_yMg_{1-x-y}Se$ based lasers and LEDs.

6-2. Future Works

1. We suggest incorporating the CdSe/ZnCdMgSe SAQDs in the active layer of light emitting devices to get LEDs and LDs that cover the whole visible range. It would be of great interest to get the white light LEDs and LDs by carefully designing the device structures either through stacking or mask patterning the red-green-blue color components.

2. We suggest investigating the effect of Mg on the formation of

CdSe/ZnCdMgSe SAQDs by changing the Mg concentration of ZnCdMgSe barrier layer.

Publications

1. Journal Publications (24 publications in total)

1. **X. Zhou**, Maria C. Tamargo, Martin Muñoz, H. Liu, A. Couzis, C. Maldarelli, Y. S. Huang, and L. Malikova, "*Effect of Beryllium concentration on the size of self-assembled CdSe quantum dots grown on $Zn_{1-x}Be_xSe$ by molecular-beam epitaxy*", J. Vac. Sci. Technol. **B 23(3),** May/June (2005).

2. Y. Gu, Igor L. Kuskovsky, M. van der Voort, G.F. Neumark, **X. Zhou**, and M.C. Tamargo, " *Zn-Se-Te Multilayers With Sub-monolayer Quantities of Te: Type-II Quantum Structures and Isoelectronic Centers* ", Phys. Rev. B. **70**, 045340 (2005).

3. M. Noemi Perez Paz, **X. Zhou**, Martin Muñoz, Hong Lu, Mohamad Sohel, Maria C. Tamargo, Fleumingue Jean-Mary and Daniel L. Akins, "*CdSe self-assembled quantum dots with ZnCdMgSe barriers emitting throughout the visible spectrum*", Appl. Phys. Lett. **85**,6395 (2004).

4. M. Noemi Perez Paz, **X. Zhou**, Martin Muñoz, Mohammad Sohel, Hong Lu, Francisco Fernandez, and Maria C. Tamargo, "*Single layer and stacked CdSe self-assembled quantum dots with ZnCdMgSe barriers for visible light emitters*", J. Vac. Sci. Technol. **B 23(3),** May/June (2005).

5. M. Sohel, **X. Zhou**, H. Lu, M. N. Perez Paz, M. C. Tamargo, and M. Muñoz, "*Optical Characterization and Evaluation of the Conduction Band Offset for ZnCdSe/ZnMgSe Quantum Wells Grown on InP(001) by MBE*", J. Vac. Sci. Technol. **B 23(3),** May/June (2005).

6. **Xuecong Zhou**, Martin Muñoz, Shiping Guo, Maria C. Tamargo, Yi Gu, Igor L. Kuskovsky, R.Robinson, I. P. Herman, and G. F. Neumark, "*CdSe quantum dots grown on ZnSe and $Zn_{0.97}Be_{0.03}Se$ by Molecular Beam Epitaxy: Optical studies*", J. Vac. Sci. Technol. **B 22**, 1518 (2004).

7. **Xuecong Zhou**, Martin Muñoz, Maria C. Tamargo, and Y. C. Chen, "*Optically Pumped Laser Characteristics of Blue $Zn_xCd_yMg_{1-x-y}Se$ /$Zn_xCd_yMg_{1-x-y}Se$ Single Quantum Well Lasers Grown on InP*", J. Appl. Phys. **95**, 7 (2004).

8. Y. Gu, Igor L Kuskovsky, J. Fung, R. R. Robinson, I. P. Herman, G. F. Neumark, **X. Zhou**, S. P. Guo, Martin Muñoz, and M. C. Tamargo, "*Optically active CdSe/Zn(Be)Se quantum dots: effect of Beryllium*", submitted to J. Appl. Phys. (2004).

9. M. Muñoz, H. Lu, S.P. Guo, **X. Zhou**, M.C. Tamargo, F.H. Pollak, Y.S. Huang, C. Trallero-Giner and A.H. Rodríguez, "*Contactless Electroreflectance Studies of II-VI Nanostructures Grown by Molecular Beam Epitaxy*", Phys. Stat Sol **(b) 241**, 546 (2004).

10. Igor L. Kuskovsky, Y. Gu, M. van der Voort, G. F. Neumark, **X. Zhou**, M. Munoz, and M. C. Tamargo, "*Quantum structures in Zn-Se-Te System Containing Submonolayer Quantities of Te*", Phys. Stat. Sol. **(b) 241**, 527 (2004).

11. Y. Gu, Igor L Kuskovsky, M. van der Voort, G. F. Neumark, **X. Zhou**, M. Munoz, and M. C. Tamargo, "*Time-resolved Photoluminescence Studies of Zn-Se-Te Nanostructures with Sub-mono Layer Quantities of Te Grown my Molecular Beam Epitaxy*", Phys. Stat. Sol. **(b) 241**, 515 (2004).

12. Y. Gu, Igor L Kuskovsky, J. Fung, G. F. Neumark, **X. Zhou**, S. P. Guo, and M. C. Tamargo, "*Optical investigation of CdSe/Zn(Be)Se quantum dot structures: size and Cd composition*", Phys. Stat. Sol. **(c) 1,** 779 (2004).

13. **X. Zhou**, Y. Gu, Igor L. Kuskovsky, L. Zeng, G. F. Neumark, and M. C. Tamargo, "*Photoluminescence of $Zn_xCd_yMg_{1-x-y}Se$ alloys as a manifestation of the breakdown of "Common-anion Rule"*", J. Appl. Phys. **94**, 7136 (2003).

14. **X. Zhou**, M. C. Tamargo, S. P. Guo, and Y. C. Chen, "*Optical Properties of CdSe Quantum Dots Grown on ZnSe and ZnBeSe By Molecular Beam Epitaxy*", J. Electron. Mater. V. **32**, 733 (2003).

15. M. Muñoz, S.P. Guo, **X. Zhou**, M.C. Tamargo, Y.S. Huang, C. Trallero and A.H. Rodríguez, "*Contactless Electroreflectance of CdSe/ZnSe Quantum Dots Grown by Molecular Beam Epitaxy*", App. Phys. Lett. **83**, 4399 (2003).

16. M. Muñoz, H. Lu, **X. Zhou**, M.C. Tamargo and F.H. Pollak, "*Band offset determination of $Zn_{0.53}Cd_{0.47}Se/Zn_{0.29}Cd_{0.24}Mg_{0.47}Se$*", Appl. Phys. Lett. **83**, 1995 (2003).

17. Y. Gu, Igor L Kuskovsky, J. Fung, R. R. Robinson, I. P. Herman, G. F. Neumark, **X. Zhou**, S. P. Guo, and M. C. Tamargo, "*Determination of Size and Composition of Optically Active CdZnSe/ZnBeSe Quantum Dots*", Appl. Phys. Lett. **83,** 3779 (2003).

18. Y. Gu, Igor L. Kuskovsky, G. F. Neumark, **X. Zhou**, O. Maksimov, S. P. Guo, and M. C. Tamargo, "*Observation of free-to-acceptor-type photoluminescence in chlorine-doped Zn(Be)Se*", J. of Lumin. **104**, 77 (2003).

19. Y. Gu, Igor L. Kuskovsky, J. Fung, R. Robinson, I. P. Herman, G. F. Neumark, **X. Zhou**, S. P. Guo, and M. C. Tamargo, "*CdSe/Zn(Be)Se Quantum Dot structures:*

Size, Chemical Composition, and Phonons", Mater. Res. Soc. Symp. Proc.**799**, Z9.7 (2003).

20. Igor L. Kuskovsky, Y. Gu, J. Lau, G.F. Neumark, O. Maksimov, S.P. Guo, **X. Zhou**, M.C. Tamargo, V. Volkov, Y. Zhu, and L. Wang, "*Doped Nano-Clusters for Improved Semiconductor Performance*", submitted to Phys. Rev. Lett. (2003).

21. S. K. Zhang, W. B. Wang, F. Yun, L. He, H. Morkoç, **X. Zhou**, M. Tamargo, and R. R. Alfano, "*Backilluminated ultraviolet photodetector based on GaN/AlGaN multiple quantum wells*", Appl. Phys. Lett. **81**, 4628 (2002).

22. S. K. Zhang, W. B. Wang, I. Shtau, F. Yun, L. He, H. Morkoç, **X. Zhou**, M. Tamargo, and R. R. Alfano, "*Backilluminated GaN/AlGaN heterojunction ultraviolet photodetector with high internal gain*", Appl. Phys. Lett. **81**, 4862 (2002).

23. S. P. Guo, W. Lin, **X. Zhou**, and M. C. Tamargo, "*High p-type doping of ZnBeSe using a modified delta-doping technique with N and Te*", J. Appl. Phys., **90**, 1725 (2001).

24. S. P. Guo, **X. Zhou**, O. Maksimov, and M. C. Tamargo, "*Effects of Be on the II-VI/GaAs interface and on CdSe quantum dot formation*", J. Vac. Sci. Technol. **B 19(4),** 1635 (2001).

2. Conference Presentations (16 presentations in total)

1. **X. Zhou**, Maria C. Tamargo, Martin Muñoz, H. Liu, A. Couzis, C. Maldarelli, Y. S. Huang, and L. Malikova, "*Effect of Beryllium concentration on the size of self-assembled CdSe quantum dots grown on $Zn_{1-x}Be_xSe$ by molecular-beam epitaxy*", 22nd **North American Molecular Beam Epitaxy Conference,** Banff, Alberta, Canada, 2004 (oral).

2. M. Noemi Perez Paz, **X. Zhou**, Martin Muñoz, Mohammad Sohel, Hong Lu, Francisco Fernandez, and Maria C. Tamargo, "*Single layer and stacked CdSe self-assembled quantum dots with ZnCdMgSe barriers for visible light emitters*", 22nd **North American Molecular Beam Epitaxy Conference,** Banff, Alberta, Canada, 2004 (oral).

3. M. Sohel, **X. Zhou**, H. Lu, M. N. Perez Paz, M. C. Tamargo, and M. Muñoz, "*Optical Characterization and Evaluation of the Conduction Band Offset for ZnCdSe/ZnMgSe Quantum Wells Grown on InP(001) by MBE*", 22nd **North American Molecular Beam Epitaxy Conference,** Banff, Alberta, Canada, 2004 (oral).

4. **Xuecong Zhou**, Martin Muñoz, Shiping Guo, Maria C. Tamargo, Yi Gu, Igor L. Kuskovsky, and G. F. Neumark, *"Photoluminescence properties of CdSe quantum dots grown on ZnSe and $Zn_{0.97}Be_{0.03}Se$ by Molecular Beam Epitaxy"*, 21st **North American Molecular Beam Epitaxy Conference**, Keystone, Colorado, 2003 (oral).

5. M. Muñoz, S.P. Guo, **X. Zhou**, M.C. Tamargo, Y.S. Huang, C. Trallero and A.H. Rodríguez, *"Contactless Electroreflectance of CdSe/ZnSe Quantum Dots Grown by Molecular Beam Epitaxy"*, 21st **North American Molecular Beam Epitaxy Conference**, Keystone, Colorado, 2003 (poster).

6. **Xuecong Zhou**, Martin Muñoz, and Maria C. Tamargo, *"Effect of Be concentration on the formation of self-assembled quantum dots of CdSe on ZnBeSe"*, **11th International Conference on II-VI Compounds**, Niagara Falls, New York, 2003 (poster).

7. M. Muñoz, H. Lu, S.P. Guo, **X. Zhou**, M.C. Tamargo, F.H. Pollak, Y.S. Huang, C. Trallero-Giner and A.H. Rodríguez, *"Contactless Electroreflectance of CdSe/ZnSe Quantum Dots Grown by Molecular Beam Epitaxy"*, **11th International Conference on II-VI Compounds**, Niagara Falls, New York, 2003 (oral).

8. M. Muñoz, H. Lu, **X. Zhou**, M.C. Tamargo and F.H. Pollak, *"Band offset determination of $Zn_{0.53}Cd_{0.47}Se/Zn_{0.29}Cd_{0.24}Mg_{0.47}Se$"*, **11th International Conference on II-VI Compounds**, Niagara Falls, New York, 2003 (poster).

9. **Xuecong Zhou**, Martin Muñoz, Maria C. Tamargo, and Y. C. Chen, *"Optically Pumped Laser Characteristics of Blue $Zn_xCd_yMg_{1-x-y}Se$ /$Zn_xCd_yMg_{1-x-y}Se$ Single Quantum Well Lasers Grown on InP"*, **APS March Meeting 2003**, Austin, Texas (oral).

10. M. Muñoz, H. Lu, **X. Zhou**, M.C. Tamargo and F.H. Pollak, *"Band offset determination of $Zn_{0.53}Cd_{0.47}Se/Zn_{0.29}Cd_{0.24}Mg_{0.47}Se$"*, **APS March Meeting 2003**, Austin, Texas (oral).

11. Y. Gu, Igor L. Kuskovsky, J. Fung, R. Robinson, I. P. Herman, G. F. Neumark, **X. Zhou**, S. P. Guo, and M. C. Tamargo, *"CdSe/Zn(Be)Se Quantum Dot Structures: Size, Composition and Phonons"*, **MRS Fall Meeting, 2003 (oral session).**

12. Y. Gu, Igor L. Kuskovsky, M. Van der Voort, G. F. Neumark, X. Zhou, W. C. Lin, M. C. Tamargo, *"Quantum Structures in Zn-Se-Te systems with sub-monolayer quantities of Te: Dimensionality vs. Te concentration"*, **11th International Conference on II-VI Compounds,** Niagara Falls, NY, 2003 (poster).

13. Igor L. Kuskovsky, Y. Gu, M. Van der Voort, G. F. Neumark, **X. Zhou**, M. Sohel, M. Muñoz, and M. C. Tamargo, "*Quantum Confinement Effects in Structures Grown via Delta-doping during Molecular Beam Epitaxy*", **11th International Conference on II-VI Compounds,** Niagara Falls, NY, 2003 (oral).

14. Y. Gu, Igor L. Kuskovsky, J. Fung, R. Robinson, I. P. Herman, G. F. Neumark, **X. Zhou**, S. P. Guo, M. C. Tamargo, "*Optical Investigation of CdSe/ZnBeSe Quantum Dot Structure: Size, Cd Composition and Phonons*", **11th International Conference on II-VI Compounds,** Niagara Falls, NY, 2003 (poster).

15. **X. Zhou**, M. C. Tamargo, S. P. Guo, and Y. C. Chen, *"Optical Properties of CdSe Quantum Dots Grown on ZnSe and ZnBeSe By Molecular Beam Epitaxy"*, **U. S. Workshop on the PHYSICS and CHEMISTRY of II-VI MATERIALS (2002)**, San Diego, California.

16. O. Maksimov, **X. Zhou**, S. P. Guo, and M. C. Tamargo, *"Be-chalcogenide alloys for improved R-G-B LEDs: $Be_xZn_{1-x}Te$ and $Be_xZn_yCd_{1-x-y}Se$ on InP"*, Presentation on **10th International Conference on II-VI Compounds**, Germany, 2001.

REFERENCES

Chapter 2

1. Y. Arakawa and H. Sakaki, Appl. Phys. Lett. **40**, 939 (1982).

2. S. Schmitt-Rink, D. Miller, and D. Chemla, Phys. Rev. B **35**, 3113 (1987).

3. J. –Y. Marzin, J. –M. Gerard, A. Izrael, D. Barrier, and G. Bastard, Phys. Rev. Lett. **73**, 716 (1994).

4. M. Grundmann, J. Cristein, N. N. Ledentsov, J. Böhrer, D. Bimberg, S. S. Ruvimov, P. Werner, U. Richter, U. Gösele, J. Heydenreich, V. M. Ustinov, A. Y. Egorov, A. E. Zhukov, P. S. Kop'ev, and Zh. I. Alferov, Phys. Rev. Lett. **74**, 4043 (1995).

5. S. Fafard, D. Leonard, J. L. Merz, and P. M. Petroff, Appl. Phys. Lett. **65**, 1388 (1994).

6. Jacques I. Pankove, *Optical Processes in Semiconductors*, Dover Publications Inc., 1975.

7. H. C. Casey, JR and M. B. Panish, *Heterostructure Lasers*, Academic Press, 1984.

8. M. C. Tamargo, A. Cavus, L. Zeng, N. Dai, N. Bambha, A. Gary, F. Semendy, W. Krystek, and F. H. Pollak, J. Electron. Mater. **25**, 259 (1996).

9. A. Cavus, L. Zeng, M. C. Tamargo, N. Bambha, F. Semendy, and A. Gary, Appl. Phys. Lett. **68**, 3446 (1996).

10. L. Zeng, B. X. Yang, A. Cavus, W. Lin, Y. Y. Guo, M. C. Tamargo, Y. Guo, and Y. C. Chen, Appl. Phys. Lett. **72**, 3136 (1998).

11. M. C. Tamargo, W. Lin, S. P. Guo, Y. Luo, Y. Guo, and Y. C. Chen, J. Cryst. Growth **214/215**, 1058 (2000).

12. S. H. Xin, P. D. Wang, Aie Yin, C. Kim, M. Dobrowolska, J. L. Merz, and J. K. Furdyna, Appl. Phys. Lett. **69**, 3884 (1996).

13. S. V. Ivanov, A. A. Toropov, T. V. Shubina, S. V. Sorokin, A. V. Lebedev, I. V. Sedova, P. S. Kop'ev, G. R. Pozina, J. P. Bergman, and B. Monemar, J. Appl. Phys. **83**, 3168 (1998).
14. J. M. Gerald, O. Cabrol, and B. Sermage, Appl. Phys. Lett. **68**, 3123 (1996).

15. A. Y. Cho, Thun Solid Films **100**, 291 (1983).

16. A. Y. Cho and J. R. Arthur, Prog. Solid State Chem. **10**, 157 (1975).

17. H. H. Farrell, M. C. Tamargo, J. H. de Miguel, F. S. Turco, D. M. Hwang, and R. E. Nahory, J. Appl. Phys. **69**, 7021 (1991).

18. A. Y. Cho, J. Vac. Sci. Technol. **8**, S31 (1971).

19. W. Demtroder, *Laser Spectroscopy*, Springer Series in *Chemical Physics 5* (Springer, Berlin, 1988), Vol. 5.

20. H. B. Bebb and E. W. Williams, in: *Semiconductors and Semimetals,* Edited by R. K. Willardson and A. C. Beers, Academic Press, Vol. **8**, 1972.

21. M. A. G. Halliwell: Prog. Crystal Growth and Charact. **19**, 249 (1989).

22. A. Segmüller, I. C. Noyan, V. S. Speriosu: Prog. Crystal Growth and Charact. **18**, 21 (1989).

23. A. T. Macrander, G. P. Schwartz, and G. J. Gualtieri, J. Appl. Phys. **64**, 6733 (1988).

24. G. Binning, C. F. Quate, and Ch. Gerber, Phys. Rev. Lett. **56**, 930 (1986).

25. F. H. Pollak and H. Shen, Mater. Sci. Eng. **R10**, 275 (1993).

26. O. J. Glembocki and B. V. Shanabrook, in *Semiconductors and Semimetals*, vol. 36, ed. D. G. Seiler and C. L. Littler, Academic Press, New York, 1992, p. 221, and references therein.

27. F. H. Pollak, in *Handbook on Semiconductors*, vol. **2**, ed. M. Balkanski, North-Holland, Amsterdam, 1994, p. 527, and references therein.

28. W. Krystek, M. Leibovitch, F. H. Pollak, M. L. Gray, and W. S. Hobson, IEEE J. Selected Topics Quantum Electron. **1**(4), 1002 (1995).

29. H. Shen and M. Dutta, J. Appl. Phys. **78**, 2151 (1995).

30. F. H. Pollak, in *Photonic Probes of Surfaces*, ed. P. Halevi, North-Holland, New York, 1995, p. 175.

31. A. K. Ramdas and S. Rodriguez, in *Semiconductors and Semimetals*, vol. 36, ed. D. G. Seiler and C. L. Littler, Academic Press, New York, 1992, p. 137, and references therein.

32. D. E. Aspnes, *Mat. Res. Soc. Symp. Proc.* **324**, 3 (1994); also *Proc. Society of Photo-optical Instrumentation Engineers* (SPIE, Bellingham, 1990) **1361**, 551.

33. O. Acher, S. M. Koch, F. Omnes, M. Defour, M. Razeghi, and B. Drévillon, J. Appl. Phys. **68**, 3564 (1990); W. Richter, Phil. Trans, R. Soc. London A **344**, 453 (1993).

34. F. H. Pollak in *Group III Nitride Semiconductor Compounds*, ed. By B. Gil (Clarendon, Oxford, 1998), p.158.

Chapter 3

1. W. A. Harrison, Electronic Structure and Properties of Solids (Freeman, San Francisco, 1980), pp. 74-80; A. A. Levin, *Solid State Quantum Chemistry* (McGraw Hill, New York, 1977).

2. W. Harrison, J. Vac. Sci. Technol. **14**, 1016 (1977).

3. W. Harrison, J. Vac. Sci. Technol. **B 3**, 1231 (1985).

4. W. A. Harrison and J. Tersoff, J. Vac. Sci. Technol. **B 4**, 1068 (1986).

5. J. A. Van Vechten, Phys. Rev. **187**, 1007 (1964), and J. Vac. Sci. Technol. **B 3**, 1240 (1985).

6. See review by R. Bauer and G. Margaritondo, Phys. Today **41**, No. 1, 26 (1987).

7. See review by G. Duggan, J. Vac. Sci. Technol. **B 3**, 1224 (1985).

8. J. O. McCaldin, T. C. McGill, and C. A. Mead, Phys. Rev. Lett. **36**, 56 (1976).

9. M. C. Tamargo, W. Lin, S. P. Guo, Y. Y. Luo, and Y. C. Chen, J. Cryst. Growth **214/215**, 1058 (2000).

10. W. Faschinger and J. Nürnberger, Appl. Phys. Lett. **77**, 187 (2000).

11. L. Zeng, B. X. Yang, A. Cavus, W. Lin, Y. Y. Luo, M. C. Tamargo, Y. Guo, and Y. C. Chen, Appl. Phys. Lett. **72**, 3136 (1998).

12. Xuecong Zhou, Martin Muñoz, M. C. Tamargo, and Y. C. Chen, J. Appl. Phys. **95**, 7 (2004).

13. J. X. Shen, R. Pittini, Y. Oka, S. P. Guo, and M. C. Tamargo, Appl. Phys. Lett. **75**, 3494 (1999).

14. M. Strassburg, M. Strassburg, O. Schulz, U. W. Pohl, D. Bimberg, D. Litvinov, D. Gerthsen, M. Schmidbauer, and P. Schäfer, J. Cryst. Growth **221**, 416 (2000).

15. P. Prete, N. Lovergine, L. Tapfer, C. Zanotti-Fregonara, and A. M. Mancini, J. Cryst. Growth **214**, 119 (2000).

16. S. Permogorov, and A. Reznitsky, J. of Lumin. **52**, 201 (1992).

17. S. A. Permogorov, A. Yu, L. N. Naumov, L. N. Tenishev, A. N. Reznitsky, and D. L. Fedorov, Phys. Solid State **37**, 1350 (1995).

18. C. F. Klingshirn, *Semiconductor Optics*, Springer, New York, 1997.

19. J. L. Pankove, *Optical Processes in Semiconductors*, 1974, Dover, New York.

20. C. Gourdon, P. Lavallard, S. Permogorov, A. Reznitsky, Y. Aaviksoo, and Y. Lippmaa, J. of Lumin. **39**, 111 (1987).

21. L. Zeng, B. X. Yang, M. C. Tamargo, E. Snoeks, and L. Zhao, Appl. Phys. Lett. **72**, 1317 (1998).

22. L. Zeng, S. P. Guo, Y. Y. Luo, M. C. Tamargo, H. Xing, and G. S. Cargill III, J. Vac. Sci. Technol. **B 17**, 1255 (1999).

23. Here we use the temperature dependence of the CdSe bandgap energy (I. Hernandez-Calderon, in *II-VI Semiconductor Materials and Their applications*, edited by M. C. Tamargo, Taylor & Francis, New York, 2002) as a general reference.

24. T. Y. Lin, J. C. Fan and Y. F. Chen, Semicond. Sci. Technol. **14**, 406 (1999).

25. S. M. Olshoorn, F. A. J. M. Driessen, A. P. A. M. Eijkelenboom, and L. J. Giling, J. Appl. Phys. **73**, 7798 (1993).

26. We plot only PL of samples with [Mg]≥20% and higher, since at lower Mg compositions samples show negligible PL shifts with excitation intensity.

27. I. Kuskovsky, D. Li, G.F. Neumark, V.N. Bondarev, and P.V. Pikhitsa, Appl. Phys. Lett. **75**, 1243 (1999).

28. M. Wörz, E. Griebl, Th. Reisinger, R. Flierl, B. Haserer, T. Semmler, T. Frey, and W. Gebhardt, Phys. Stat. Sol. (b) **202**, 805 (1997).

29. S. –H. Wei and A. Zunger, Appl. Phys. Lett. **72**, 2011 (1998).

30. W. I. Wang and F. Stern, J. Vac. Sci. Technol. B **3**, 1280 (1985).

31. S. P. Kowalczyk, J. T. Cheung, E. A. Kraut, and R. W. Grant, Phys. Rev. Lett. **56**, 1605 (1986).

32. J. R. Waldrop and R. W. Grant, Appl. Phys. Lett. **68**, 2879 (1996).

33. S. –H. Wei, and A. Zunger, Phys. Rev. Lett. **59**, 144 (1987).

Chapter 4

1. M. A. Haase, J. Qiu, J. M. DePuydt, and H. Cheng, Appl. Phys. Lett. **59**, 1272 (1991).

2. E. Kato, H. Noguchi, M. Nagai, H. Okuyama, S. Kijima, and A. Ishibashi, Electron. Lett. **34**, 282 (1998).

3. S. Nakamura, M. Senoh, S. Nagahama, N. Iwasa, T. Yamada, T. Matsushita, H. Kiyoku, Y. Sugimoto, T. Kozacki, H. Umemoto, M. Sano, and K. Chocho, Appl. Phys. Lett. **72**, 2014 (1998).

4. S. Nakamura, and G. Fasol, *The Blue Laser Diode*, Springer-Verlag, Berlin 1997.

5. D. P. Bour, in: *Quantum Well Lasers*, Ed. P. S. Zory, JR., Academic Press, New York, 1993. (P. 415-460).

6. C. P. Kuo, R. M. Fletcher, T. D. Osentowski, M. C. Landizabal, M. G. Craford, and V. M. Robbins, Appl. Phys. Lett. **57**, 2937 (1990).

7. A. Valster, M. N. Finke, M. J. B. Boermans, J. M. M. V. D. Heijden, C. J. G. P. Spreuwenberg, and C. T. H. F. Liedenbaum, in: *Proc. 12th IEEE Internat. Semiconductor Laser Conf.*, Davos (Switzerland), Sept. 9-14, 1990 (paper PD-12).

8. H. Hamada, K. Tominaga, M. Shoho, S. Honda, K. Yodoshi, and T. Yamaguchi, Electron. Lett. **28**, 18334 (1992).

9. Y. Kaneko, I. Nomura, K. Kishino, and A. Kikuchi, J. Appl. Phys. **74**, 819 (1993).

10. R. V. Chelakara, M. R. Islam, J. G. Neff, K. G. Fertitta, A. L. Holmes, F. J. Ciuba, R. D. Dupuis, T. A. Richard, N. Holonyak, JR., and K. C. Hsieh, Appl. Phys. Lett. **65**, 854 (1994).

11. D. J. Mowbray, O. P. Kowalski, M. Hopkinson, M. S. Skolnick, and J. P. R. David, Appl. Phys. Lett. **65**, 213 (1994).

12. G. M. Haugen, S. Guha, H. Cheng, J. M. DePuydt, M. A. Hasse, G. E. Hfler, J. Qiu, and B. J. Wu, Appl. Phys. Lett. **66**, 358 (1995).

13. M. Hovinen, J. Ding, A. V. Nurmikko, G. C. Hua, D. C. Grillo, L. He, J. Han, and R. L. Gunshor, Appl. Phys. Lett. **66**, 2013 (1995).

14. L.-L. Chao, G. S. Cargill III, C. Kothandaraman, T. Marshall, E. Snoeks, M. Buijs, K. Haberern, J. Petruzzello, G. M. Haugen, and K. K. Law, Appl. Phys. Lett. **70**, 535 (1997).

15. M. C. Tamargo, A. Cavus, L. Zeng, N. Dai, N. Bambha, A. Gary, F. Semendy, W. Krystek, and F. H. Pollak, J. Electron. Mater. **25**, 259 (1996).

16. A. Cavus, L. Zeng, M. C. Tamargo, N. Bambha, F. Semendy, and A. Gary, Appl. Phys. Lett. **68**, 3446 (1996).

17. L. L. Chao, H. Xing, G. S. Cargill III, L. Zeng, and M. C. Tamargo, *Bulletin of the American Physical Society* **43**, 718 (1998). APS March Meeting, Los Angeles, CA., USA.

18. L. Zeng, B. X. Yang, A. Cavus, W. Lin, Y. Y. Guo, M. C. Tamargo, Y. Guo, and Y. C. Chen, Appl. Phys. Lett. **72**, 3136 (1998).

19. S. P. Guo, L. Zeng, and M. C. Tamargo, Appl. Phys. Lett. **77**, 1 (2001).

20. L. Zeng, S. P. Guo, Y. Y. Luo, M. C. Tamargo, H. Xing, and G. S. Cargill III, J. Vac. Sci. Technol. **B17**, 1255 (1999).

21. F. C. Peiris, J. K. Furdyna, S. P. Guo, and M. C. Tamargo, J. Appl. Phys. **89**, 1 (2001).

22. L. Zeng, B. X. Yang, and M. C. Tamargo, Appl. Phys. Lett. **72**, 1317 (1998).

23. J. H. Chang, M. W. Cho, K. Godo, H. Makino, T. Yao, M. Y. Shen, and T. Goto, Appl. Phys. Lett. **75**, 894 (1999).

24. T. R. Chen, B. Chang, L. C. Chiu, K. L. Yu, S. Margalit and A. Yariv, Appl. Phys. Lett. **43**, 217 (1983).

25. L. C. Chiu, K. L. Yu, S. Margalit, T. R. Chen, U. Koren, A. Hasson and A. Yariv, IEEE J. Quantum Electron. QE-**19**, 1335 (1983).

26. G. H. B. Thompson, IEEE Proc., I**128**, 37 (1981).

27. A. Sugimura, IEEE J. Quantum Electron, QE-**17**, 441 (1981).

28. David P. Bour, David W. Treat, Robert L. Thornton, Randall S. Geels, and David F. Welch, IEEE J. Quantum Electron. **29**, 1337 (1993).

29. T. Fukushima, H. Shimizu, K. Nishikata, Y. Hirayama, and M. Irikawa, Appl. Phys. Lett. **66 (16)**, 2025 (1995).

30. K. Kishino, A. Kikuchi, Y. Kaneko, and I. Nomura, Appl. Phys. Lett. **58**, 1822 (1991).

Chapter 5

1. F. Bloch, Z. Physik **52**, 555 (1928).

2. V. N. Lutskii, Phys. Stat. Sol. (a) **1**, 199 (1970).

3. I. N. Stranski and L. Krastranow, *"Zur Theorie der orientation Ausscheidung von lonenkristallen aufeinander,"* Math.-Naturwiss. Kl., **146**, 797 (1938).

4. J. K. Furdyna, S. Lee, A.-L. Barabási and J. L. Merz, in *"II-VI Semiconductor Materials and Their Applications"*, edited by M. C. Tamargo (Taylor & Francis, New York, 2002).

5. Y. W. Mo, D. E. Savage, B. S. Swartzentruber, and M. G. Lagally, Phys. Rev. Lett. **65**, 1020 (1990).

6. D. J. Eaglesham and M. Cerullo, Phys. Rev. Lett. **64**, 1943 (1990).

7. L. Goldstein, F. Glas, J. Y. Marzin, M. N. Charasse, and G. L. Roux, Appl. Phys. Lett. **47**, 1099 (1985).

8. Kazunari Ozasa, Yoshinobu Aoyagi, Akihiko Yamane, and Yoshio Arai, Appl. Phys. Lett. **83**, 2247 (2003).

9. J. M. Moison, F. Houzay, F. Barthe, L. Leprince, E. Andre, and O. Vatel, Appl. Phys. Lett. **64**, 196 (1994).

10. M. Gurioli, S. Sanguinetti, E. Grilli, M. Guzzi, S. Taddei, A. Vinattieri, M. Colocci, P. Frigeri, and S. Franchi, Appl. Phys. Lett. **83**, 2262 (2003).

11. S. P. DenBaars, C. M. Reaves, V. Bressler-Hill, S. Varma, and H. Weinberg, J. Cryst. Growth **145**, 721 (1994).

12. J. Ahopelto, H. Lipsanen, M. Sopanen, Y. T. Koljonen, and H. E. M. Niemi, Appl. Phys. Lett. **65**, 1662 (1994).

13. N. Carlsson, W. Seifert, A. Petersson, P. Castrillo, M. –E. Pistol, and L. Samuelson, Appl. Phys. Lett. **65**, 3093 (1994).

14. M. Lowisch, M. Rabe, B. Stegermann, F. Henneberger, M. Grundmann, V. T rck, and Bimberg, Phys. Rev. B **54**, R11074 (1996).

15. S. H. Xin, P. D. Wang, Aie Yin, C. Kim, M. Dobrowolska, J. L. Merz, and J. K. Furdyna, Appl. Phys. Lett. **69**, 3884 (1996).

16. D. Li and M. D. Pashley, J. Vac. Sci. Techno. B **12**, 2547 (1994).

17. M. Keim, M. Korn, J. Seufert, G. Bacher, A. Forchel, G. Landwehr, S. Ivanov, S. Sorokin, A. A. Sitnikova, T. V. Shubina, A. Toropov, and A. Waag, J. Appl. Phys. **88**, 7051 (2000).

18. Z. H. Zheng, K. Okamoto, H. C. Ko, Y. Kawakami, and Sg. Fujita, Appl. Phys. Lett. **78**, 297 (2001).

19. B. P. Zhang, K. Wakatsuki, D. D. Manh, and Y. Segawa, J. Appl. Phys. **88**, 4916 (2000).

20. I. Svare, S. W. Martin, and F. Borsa, Phys. Rev. B **61**, 228 (2000).

21. J. S. Massa, G. S. Buller, A. C. Walker, G. Horsburgh, J. T. Mullins, K. A. Prior and B. C. Cavenett, Appl. Phys. Lett. **66**, 1346 (1995).

22. L. Marsal, L. Besombes, F. Tinjod, K. Kheng, A. Wasiela, B. Gilles, J. -L. Rouvière, and H. Mariette, J. Appl. Phys. **91**, 4936 (2002).

23. D. B. Tran Thoai, Y. Z. Hu, and S. W. Koch, Phys. Rev. B **42**, 11261 (1990).

24. C. Chauvet, E. Tournié, and J. –P. Faurie, Phys. Rev. B **61**, 5332 (2000).

25. V. Pellegrini, R. Atamasov, A. Tredicucci, F. Beltram, C. Amzulini, L. Sobra, L. Vanzetti, and A. Francioso, Phys. Rev. B **51**, 5176 (1995).

26. C. G. Van de Walle, Phys. Rev. B **39**, 1871 (1989).

26. E. Roca, Phys. Rev. B **49**, 13704 (1994).

27. M. P. Chamberlain, C. Trallero-Giner, and M. Cardona, Phys. Rev. B **51**, 1680 (1995).

28. Yi Gu, Igor L. Kuskovsky, J. Fung, R. Robinson, I. P. Herman, G. F. Neumark, X. Zhou, S. P. Guo, and M. C. Tamargo, Appl. Phys. Lett. **83**, 3779 (2003).

29. Huaxiang Fu, Lin-Wang Wang, and Alex Zunger, Phys. Rev. B **59**, 5568 (1999).

30. D. V. Melnikov and W. B. Fowler, Phys. Rev. B **64**, 245320 (2001).

31. F. H. Pollak and H. Shen, Mater. Sci. Eng., R. **10**, 275 (1993).

32. A. H. Rodríguez, C. Trallero-Giner, S. E. Ulloa, and J. Marín-Antuña, Phys. Rev. B **63**, 125319 (2001). A. H. Rodríguez, C. R. Handy, and C. Trallero-Giner, J. Phys.: Condens. Matter **15**, 8465 (2003).

33. R. E. Nahory, M. J. S. P. Brasil and M. C. Tamargo, in *Semiconductor Interfaces and Microstructures*, Ed. Z. Feng (World Scientific, Singapore, 1992). P. 238.

34. Martin Muñoz, Shiping Guo, Xuecong Zhou, Maria C. tamargo, Y. S. Huang, C. Trallero-Giner, and A. H. Rodríguez, Appl. Phys. Lett. **83**, 4399 (2003).

35. Yi Gu, Igor L. Kuskovsky, J. Fung, R. Robinson, I. P. Herman, G. F. Neumark, X. Zhou, S. P. Guo, and M. C. Tamargo, in preparation.

36. S. P. Guo, X. Zhou, O. Maksimov, M. C. Tamargo, C. Chi, A. Couzis, C. Maldarelli, I. L. Kuskovsky and G. F. Neumark, J. Vac. Sci. Technol. B**19**, 1635 (2001).

37. *Semiconductors—BasicData*, 2nd ed., edited by O. Madelung (Springer, Berlin, 1996).

38. *II-VI Semiconductor Materials and Their Applications*, edited by Maria C. Tamargo (Taylor & Francis, New York, 2002).

39. *Numerical Data and Functional Relationships in Science and Technology*, Landolt-Börnstein edited by O. Madelung, M. Schultz, and H. Weiss, (Springer, New York, 1982), Vol. III/11.

40. For simplicity, we assume no intermixing in the QDs.

41. M. Noemi Perez Paz, Xuecong Zhou, Martin Muñoz, Hong Lu, Mohammad Sohel, Maria C. Tamargo, Fleumingue Jean-Mary, and Daniel L. Akins, Appl.Phys. Lett. **85**,6395 (2004).

42. S. H. Xin, P. D. Wang, A. Yin, C. Kim, M. Dobrowolska, J. L. Merz, and J. K. Furdyna, Appl. Phys. Lett. **69**, 3884 (1996).

43. M. C. Tamargo, A. Cavus, L. Zeng, N. Dai, N. Bambha, A. Gary, F. Semendy, W. Krystek, and F. H. Pollak, J. Electron. Mater. **25**, 259 (1996).

44. X. Zhou, Y. Gu, Igor L. Kuskovsky, L. Zeng, G. F. Neumark, and M. C. Tamargo, J. Appl. Phys. **94**, 7136 (2003).

45. M. C. Tamargo, W. Lin, S. P. Guo, Y. Luo, Y. Guo, and Y. C. Chen, J. Cryst. Growth **214/215**, 1058 (2000).

46. L. Zeng, B. X. Yang, A. Cavus, W. Lin, Y. Y. Guo, M. C. Tamargo, Y. Guo, and Y. C. Chen, Appl. Phys. Lett. **72**, 3136 (1998).

47. Xuecong Zhou, Martin Muñoz, Maria C. Tamargo, and Y. C. Chen, J. Appl. Phys. **95**, 7 (2004).

48. N. Dai, A. Cavus, R. Dzakpasu, M. C. Tamargo, F. Semendy, N. Bambha, D. M. Hwang, and C. Y. Chen, Appl. Phys. Lett. **66**, 2742 (1995).